Title

A Computational Study on the Thermodynamics and Kinetic Evolution of W-Re Alloy under Irradiation

Author

Huang, Chen-Hsi

Publication Date

2017

UNIVERSITY OF CALIFORNIA
Los Angeles

A Computational Study on the Thermodynamics and Kinetic Evolution of W-Re Alloy under Irradiation

A dissertation submitted in partial satisfaction
of the requirements for the degree
Doctor of Philosophy in Materials Science and Engineering

by

Chen-Hsi Huang

2017

ABSTRACT OF THE DISSERTATION

A Computational Study on the Thermodynamics and Kinetic Evolution of W-Re Alloy under Irradiation

by

Chen-Hsi Huang
Doctor of Philosophy in Materials Science and Engineering
University of California, Los Angeles, 2017
Professor Jaime Marian, Chair

Nuclear fusion energy is a promising future energy source. However, there are still many challenges that are under studying. One big difficulty comes from material engineering: the requirement to develop a material with superior properties including high hardness, high melting temperature, high strength, high resistance to corrosion, creep, radiation, and low He retention. Among all the choices of materials, tungsten is the prime candidate for plasma-facing material in magnetic fusion energy devices due to its high strength and excellent high temperature properties. However, under irradiation, the hardness of tungsten strongly increases and the toughness is largely reduced, which is called irradiation hardening. The hardening is caused by the formation of Re precipitates, which is induced by radiation. In this work, we studied the micro-structural evolution of W and W-Re alloy under irradiation; For this purpose, we applied a bottom-up approach. We started our research on development of an atomic model. Specifically, we extended an Ising model for binary system to including interstitial. The model was verified against several published works. We then studied alloy evolution of W-Re system using various Monte Carlo simulation techniques. The thermodynamics as well as kinetic evolution of W-Re alloy were studied. Finally, we moved onto the continuum scale and study the cluster distribution and irradiation hardening using stochastic dynamics simulations. The cluster dynamics in three creator environments: DEMO, HFIR, and JOYO were simulated and the results were compared with experimental data.

The dissertation of Chen-Hsi Huang is approved.

Jenn-Ming Yang

Nasr M. Ghoniem

Mathieu Bauchy

Jaime Marian, Committee Chair

University of California, Los Angeles

2017

Table of Contents

LIST OF FIGURES

List of Tables

Acknowledgments

It is a long journey of study for me to reach this point. Look back for these 25 years, there were happiness, struggles, cheers, tears, and a lot more. It is glad that I could persist on this road when facing all the obstacles, and it is also very happy to see that for every difficulty there was a solution at the end.

The first ”thank you” goes to myself. I am really proud of you to finish this tough task. I’ll then thank my parents for all the supports. I love you, mom and dad. I would also like to give a big thank to my adviser, Jaime. You are literally the best adviser in the world. I am really grateful that I could meet you in my Ph.D. study.

I would like to thank my girlfriend, Yawen, who supported me in the second half of my Ph.D. both in life and in spirit, and motivated me in working hard. I am also appreciate with all the discussions and supports from ”Rose Friday night group”, and all other friends, who make my life better.

VITA

2003	High School, The Affiliated Senior High School of National Taiwan Normal University.
2007	B.S. (Materials, Engineering and System Science), National Tsing-Hua University.
2010	M.S. (Materials, Engineering and System Science), National Tsing-Hua University. Thesis: "*Molecular Dynamics Simulation Study: the Phase Transition of Lipid Membranes in Solution and the Stability and Fracture Mechanism of a Suspended Bilayer Lipid Membrane*".
Fall 2015	Teaching Assistant, "*Fracture of Engineering Materials*" Online Master Program in Engineering, UCLA.
Fall 2016	Teaching Assistant, "*System Engineering*" Online Master Program in Engineering, UCLA.
2014–present	Graduate Student Researcher, Materials Science Department, UCLA.

PUBLICATIONS

Chen-Hsi Huang, Pai-Yi Hsiao, Fan-Gang Tseng, Shih-Kang Fan, Chien-Chung Fu, and Rong-Long Pan, "Pore-Spanning Lipid Membrane under Indentation by a Probe Tip: A Molecular Dynamics Simulation Study", *Langmuir* 27 (19), 11930 (2011).

Chen-Hsi Huang and Pai-Yi Hsiao, "Geometric Effect of Nanopores on the Behavior and Stability of pore-spanning Lipid Membranes under Indentation", *Journal of Computational and Theoretical Nanoscience* 12, 3999 (2015).

Chen-Hsi Huang and Jaime Marian, "A Generalized Ising Model for Studying Alloy Evolution under Irradiation and its Use in Kinetic Monte Carlo Simulations", *Journal of Physics: Condensed Matter* 28, 425201 (2016).

Chen-Hsi Huang, Leili Gharaee, Yue Zhao, Paul Erhart, Jaime Marian, "Mechanism of Re Precipitation in Irradiated W-Re Alloys from Kinetic Monte Carlo Simulations", *Physical Review B* under review.

CHAPTER 1

Introduction

Tungsten is the prime candidate material in magnetic fusion energy devices due to its high strength and excellent high temperature properties [ZG00, RDV13, FN08, BD09]. Upon fast neutron irradiation in the 600-1000°C temperature range, W transmutes into Re by the way of beta decay reactions at a rate that depends on the neutron spectrum and the position in the reactor. For the DEMO (demonstration fusion power plant) reactor concept, calculations show that the transmutation rate is 2000 and 7000 atomic parts per million (appm) per displacements per atom (dpa) in the divertor and the equatorial plane of the first wall, respectively (where damage, in each case, accumulates at rates of 3.4 and 4.4 dpa/year) [GS11, GDZ12]. The irradiated microstructure initially evolves by accumulating a high density of prismatic dislocation loops and vacancy clusters, approximately up to 0.15 dpa [HTH06, THH09, HTN11, HKF16]. Subsequently, a void lattice emerges and fully develops at fluences of around 1 dpa. After a critical dose that ranges between 5 dpa for fast (>1 MeV) neutron irradiation [HTN11] and 2.2 dpa in modified target rabbits in the HFIR [HKK15, HKF16], W and W-Re alloys develop a high density of nanometric precipitates with acicular shape at Re concentrations well below the solubility limit [HTN11, HKF16]. The structure of these precipitates is consistent with σ (W_7Re_6) and χ (WRe_3) intermetallic phases, which under equilibrium conditions only occur at temperatures and Re concentrations substantially higher than those found in neutron irradiation studies [Cot04]. A principal signature of the formation of these intermetallic structures in body-centered cubic (bcc) W is the sharp increase in hardness and embrittlement [THH09, HTN11, HKF16]. Qualitatively similar observations have been recently made in W-2Re and W-1Re-1Os alloys subjected to heavy ion irradiation [XBA15, XAB17], clearly establishing a link between primary damage production and Re precipitation.

Precipitation of nonequlibrium phases in irradiated materials is commonplace. The standard theory of irradiation damage includes radiation enhanced diffusion (RED) and radiation induced precipitation (RIP) as mechanisms that can drive the system out of equilibrium due to the onset of point defect cluster fluxes towards defect sinks [Was07, DD58, CM79]. Within this picture, Re precipitation in W or W-Re alloys under irradiation would then, in principle, be unsurprising were it not for the fact that Re clustering is seen to occur at concentrations still below the solubility limit even after RED has taken place. In spite of this, recent work using energy models based on the cluster expansion formalism for the W-Re system, and fitted to density functional theory (DFT) calculations, have revealed a direct relationship between excess vacancy concentrations and the formation of Re solute-rich clusters [WNK16]. These calculations are substantiated by recent neutron irradiation experiments of pure W at 900°C up to 1.6 dpa in the HFR in Petten [KJR16]. Post-irradiation examination of the irradiated specimens reveals the formation of a fine distribution of voids with average 5 nm size surrounded by Re-rich clouds. However, the relative concentration of Re around the voids is still on the order of 12-18% (from a nominal overall concentration of 1.4% from transmutation), well below the precipitation limit of Re in W at 900°C. However, in the ion beam irradiation experiments of W-2Re alloys by Xu *et al.* at 300 and 500°C, Re-rich clusters with bcc structure are seen to form with concentrations between 12 and 30% Re with no indication of vacancies forming part of the clusters [XBA15, XAB17]. Another piece of evidence against a strong association between vacancies and Re atoms comes from irradiation tests of W-Re alloys performed at EBR-II in the 1970s and 80s [MNM74, SM74, WWB83, HS84, HS85]. In these studies, the presence of Re was seen to suppress swelling, which would seem to suggest a decoupling between vacancy clusters and Re atoms. Clearly, equilibrium thermodynamics involving vacancies alone may not suffice to explain the precipitation tendencies in irradiated W-Re alloys.

All this is suggestive of alternative solute transport mechanisms that may be unique to W-Re systems. Indeed, several recent studies using electronic structure calculations have independently reported a peculiar association between self-interstitial atoms (SIA) and Re solutes that results in very high solute transport efficacy [SYH14, SYH15, GME16]. This mechanism consists of a series of mixed dumbbell rotations and translations such that the mixed nature of the dumbbell is preserved and solutes can be transported over long distances without the need for vacancy exchanges. Furthermore, this mechanism effectively transforms one-dimensional SIA diffusion into a 3D mixed-dumbbell transport process at activation energies considerably lower than that of vacancy diffusion.

The final purpose of this work is to study the mechanical behavior of W and W-Re alloy in continuum scale such as cluster distributions, irradiation hardening, etc. To achieve this goal, we applied an bottom-up approach from atomic scale, mesoscale to micro-scale. We began our research with atomic model development. Specifically, we extended an pre-existing Ising model to include interstitials. The work is discussed in chapter (2.3). After that, we applied the model to Metropolis and kinetic Monte Carlo simulations to study the thermodynamics and alloy evolution of W-Re alloy under irradiation. This is the most important part of the work and is discussed in chapter (3.3.4). Finally, we moved onto the continuum scale and studied cluster distribution and irradiation hardening using stochastic cluster dynamics simulations, which can be seen in chapter (4.2.2).

CHAPTER 2

A generalized Ising model and its use in kinetic Monte Carlo simulations

In previous study, researchers have applied Ising model to the cluster expansion of the Hamiltonian of a binary alloy system (details will be discussed in section (2.1.1)). It was termed ABV Ising model, where A represents matrix atoms, B is solute atoms, and V is the vacancies. The models are of interest in irradiated materials, to study non-equilibrium phenomena such as radiation enhanced diffusion (RED) and radiation-induced precipitation (RIP), and indeed have been applied on numerous times in irradiation damage scenarios [SBM96,EB01,ENA03,VBP08,SBA13]. However, by their very nature, ABV simulations obviate the existence of self-interstitial atoms (SIA), which are companion to vacancies during defect production in the primary damage phase [Wol12]. Neglecting SIA (as well as mixed interstitial) involvement in solute transport can often be justified when interstitial diffusion is orders of magnitude faster than that of vacancies, and –as importantly– occurs in a (quasi) one-dimensional manner. This results in a point defect imbalance when SIAs reach defect sinks on time scales that are much shorter than those associated with vacancy motion, leaving vacancies as the sole facilitators of atomic transport [DDJ95,SBM96]. However, in certain cases interstitials play an important role in mediating solute diffusion, and their effect can no longer be dismissed when formulating global energy models for solute transport. A case in point is the recent discovery of solute drag by so-called 'bridge' interstitial configurations in W-Re/Os alloys [SYH15], although several other examples exist [WFM05, GE15, SNR15a]. In such cases, the ABV Hamiltonian is insufficient to capture the contribution of SIAs to microstructural evolution. This has prompted the development of cluster expansion Hamiltonians that include interstitials as well as vacancies as defect species [Soi05, Soi06, KAB07, VBD08, SBC10, NBD12]. To date, however, an extension of such Hamiltonians to the Ising framework has not been attempted. That is the central goal of the work described in this chapter.

Here, a generalization of the ABV Ising model to ABVI systems of binary alloys subjected to irradiation is proposed. The chapter is organized as follows: the methodology will be described in detail in Section 2.1, providing a recipe to perform the ABV→ABVI extension. Subsequently, in Section 2.2 I will provide three different verification exercises in increasing order of complexity using published works. A brief discussion and the conclusions will be given in Section 2.3.

2.1 Theory and Numerical Methods

2.1.1 Cluster expansion Hamiltonians for binary alloys

The most common approach to study the energetics of substitutional alloy systems is the cluster expansion method, in which the energies of the different crystal configurations are defined by specifying the occupation of each of the N sites of a fixed crystal lattice by a number of distinct chemical species (which may include solvent and solute atoms, defects, etc.). This problem can quickly become intractable, given the combinatorial nature of arranging N distinguishable atomic sites, and a number of approaches have been proposed to reduce the dimensional complexity of the problem [LFF92, San93, BZ04]. A common simplification is to assume that the Hamiltonian $\mathcal{H}$ of the system can be calculated as the sum of all possible pair interactions, defined by their *bond* energies:

$$\mathcal{H} = \sum_{\alpha,\beta} n_{\alpha\text{-}\beta}\epsilon_{\alpha\text{-}\beta} \tag{2.1}$$

Where α and β refer to a pair of lattice sites, n is the total number of different bond types, and ϵ is the energy coefficients.

Further, a binary system containing two types of atoms (matrix) A and (solute) B, as well as vacancy defects is termed the 'ABV' system, for which the pairwise cluster expansion Hamiltonian (2.1) can be expressed as an Ising Hamiltonian of the following form [FVP93, FPW00, WF03, WFG04]:

$$\mathcal{H} = \mathcal{H}_0 + K\sum_{\langle i,j\rangle}^{nn} \sigma_i^2\sigma_j^2 + U\sum_{\langle i,j\rangle}^{nn} \left(\sigma_i^2\sigma_j + \sigma_j^2\sigma_i\right) + J\sum_{\langle i,j\rangle}^{nn} \sigma_i\sigma_j \tag{2.2}$$

where $\langle i,j\rangle$ refers to a pair of lattice sites i and j, and σ are the occupancy variables:

$$\sigma = \begin{cases} 1 & \text{A (matrix atom)} \\ 0 & \text{V (vacancy)} \\ -1 & \text{B (solute atom)} \end{cases} \tag{2.3}$$

$\mathcal{H}_0$ in eq. (2.2) is a constant independent of the configuration of lattice sites. The three coefficients K, U, and J are:

$$\begin{aligned} K &= {}^1\!/\!_4\left(\epsilon_{\text{A-A}} + \epsilon_{\text{B-B}} + 2\epsilon_{\text{A-B}}\right) + \left(\epsilon_{\text{V-V}} - \epsilon_{\text{A-V}} - \epsilon_{\text{B-V}}\right) \\ U &= {}^1\!/\!_4\left(\epsilon_{\text{A-A}} - \epsilon_{\text{B-B}}\right) - {}^1\!/\!_2\left(\epsilon_{\text{A-V}} - \epsilon_{\text{B-V}}\right) \\ J &= {}^1\!/\!_4\left(\epsilon_{\text{A-A}} + \epsilon_{\text{B-B}} - 2\epsilon_{\text{A-B}}\right) \end{aligned}$$

Together with the activation energy parameters, which will described in Section (2.1.3.2), these constants determine the kinetic behavior of the ABV system. The second term in the r.h.s. of eq. (2.2) gives the relative importance of vacancies in the system. A large value of this term implies low vacancy concentrations, which in the limit of one single vacancy in the crystal converges to a constant value of $K'z\left({}^N\!/\!_2 - 1\right)$, where $K' = {}^1\!/\!_4\left(\epsilon_{\text{A-A}} + \epsilon_{\text{B-B}} + 2\epsilon_{\text{A-B}}\right) - \left(\epsilon_{\text{A-V}} + \epsilon_{\text{B-V}}\right)$, and z is the coordination number [WFG04]. The asymmetry factor U determines whether there is more affinity between A atoms and vacancies or B atoms and vacancies. $U > 0$ indicates a preference of A-V pairs. J determines the thermodynamics of the system, with $J > 0$ leading to an ordered solid solution, $J < 0$ to a phase-separated system, and $J = 0$ resulting in an ideal solid solution. This Hamiltonian can be trivially extended from 1^{st} nearest neighbors (nn) to higher nn by summing over all contributions:

$$\mathcal{H} = \mathcal{H}_{1^{\text{st}}\text{-}nn} + \mathcal{H}_{2^{\text{nd}}\text{-}nn} + \cdots \tag{2.4}$$

2.1.2 Generalization of the ABV Ising Hamiltonian to systems with interstitial atoms

Next, we expand eq. (2.2) to a system containing A and B atoms, vacancies, and interstitial atoms, which we term 'ABVI'. Interstitial atoms can be one of three distinct types, but in all cases two (otherwise substitutional) atoms share a single lattice position: AA denotes a self-interstitial atom (SIA), AB represents a mixed interstitial, and BB is a pure solute interstitial. Adding these extra species to the cluster expansion Hamiltonian brings the total number of species to six, which results in the following expression:

$$\mathcal{H} = \sum_{\langle i,j \rangle}^{nn} \sum_{\alpha,\beta} \epsilon_{\alpha\text{-}\beta} \lambda_i^{\alpha} \lambda_j^{\beta} \tag{2.5}$$

where $\alpha, \beta = \mathrm{A}, B, V, AA, AB, BB$ and the occupancy variable $\lambda_i^{\alpha} = 1$ if lattice site i is occupied by type α and zero otherwise. The total number of independent terms in eq. (2.5) is 36. However, assuming that a pair vacancy-interstitial is unstable up to several nearest neighbor distances, we can eliminate all the $\epsilon_{\text{V-I}} \lambda^{\text{V}} \lambda^{\text{I}}$ (where I= AA, AB, BB) terms in the equation, thus reducing the total number of terms to 30.

In the spirit of the ABV Ising model, we assign spin variables of different types to each of the species of the Hamiltonian:

$$\sigma = \begin{cases} 2 & \text{AA (self-interstitial atom)} \\ 1 & \text{A (matrix atom)} \\ 0 & \text{V (vacancy) and AB (mixed interstitial)} \\ -1 & \text{B (solute atom)} \\ -2 & \text{BB (solute-solute interstitial)} \end{cases} \tag{2.6}$$

Although the set of spin variables for the ABVI model is not unique, the one chosen above uses the lowest-order integer possible and preserves the *magnetization* of the Ising model, *i*.e. the excess amount of solvent after the solute has been subtracted out. The convenience of choosing a zero spin variable for both the V and AB species brings about some complications in the Hamiltonian, however, which will be dealt with in Section 2.1.2.1.

From their definition in eq. (2.5), the six independent λ^{α} variables can be written in terms of the spin variables furnished in eq. (2.6):

$$\begin{aligned} \lambda^{\mathrm{AA}} &= \frac{1}{24}\left(\sigma^4 + 2\sigma^3 - \sigma^2 - 2\sigma\right) \\ \lambda^{\mathrm{A}} &= \frac{1}{6}\left(-\sigma^4 - \sigma^3 + 4\sigma^2 + 4\sigma\right) \\ \lambda^{\mathrm{V}} &= \lambda^{AB} = \frac{1}{4}\left(\sigma^4 - 5\sigma^2 + 4\right) \\ \lambda^{\mathrm{B}} &= \frac{1}{6}\left(-\sigma^4 + \sigma^3 + 4\sigma^2 - 4\sigma\right) \\ \lambda^{\mathrm{BB}} &= \frac{1}{24}\left(\sigma^4 - 2\sigma^3 - \sigma^2 + 2\sigma\right) \end{aligned} \tag{2.7}$$

Inserting the above expressions into eq. (2.5) and operating, the cluster expansion Hamiltonian is transformed into a generalized Ising system with integer spins:

$$\begin{aligned} \mathcal{H} = \sum_{\langle i,j\rangle} \Big[& C_{44}\sigma_i^4\sigma_j^4 + C_{43}\left(\sigma_i^4\sigma_j^3 + \sigma_i^3\sigma_j^4\right) + C_{42}\left(\sigma_i^4\sigma_j^2 + \sigma_i^2\sigma_j^4\right) + \\ & + C_{41}\left(\sigma_i^4\sigma_j + \sigma_i\sigma_j^4\right) + C_{33}\sigma_i^3\sigma_j^3 + C_{32}\left(\sigma_i^3\sigma_j^2 + \sigma_i^2\sigma_j^3\right) + \\ & + C_{31}\left(\sigma_i^3\sigma_j + \sigma_i\sigma_j^3\right) + C_{22}\sigma_i^2\sigma_j^2 + C_{21}\left(\sigma_i^2\sigma_j + \sigma_i\sigma_j^2\right) + \\ & + C_{11}\sigma_i\sigma_j + C_{40}\left(\sigma_i^4 + \sigma_j^4\right) + C_{30}\left(\sigma_i^3 + \sigma_j^3\right) + \\ & + C_{20}\left(\sigma_i^2 + \sigma_j^2\right) + C_{10}\left(\sigma_i + \sigma_j\right) + C_{00} \Big] \end{aligned} \tag{2.8}$$

where C_{mn} are the coefficients of the cluster expansion.

2.1.2.1 Corrections to the Hamiltonian to separate V and AB contributions.

By construction, both vacancies and AB interstitials share $\sigma = 0$ in eq. (2.8), which in turn makes $\lambda_{\text{V}} = \lambda_{\text{AB}} = 1$ leading to miscounting of both contributions. Corrections must therefore be adopted to recover the correct energy from the Hamiltonian. These corrections can simply be subtracted from the uncorrected Hamiltonian in eq. (2.8) as:

$$\mathcal{H}_{\text{corrected}} = \mathcal{H}_{\text{uncorrected}} - [\text{correction terms}] \tag{2.9}$$

The correction terms can be readily identified on inspection of eq. (2.1):

$$\begin{aligned}[\text{correction terms}] &= \epsilon_{\text{V-V}} n_{\text{AB-AB}} + \epsilon_{\text{AB-AB}} n_{\text{V-V}} + \epsilon_{\text{A-V}} n_{\text{A-AB}} + \\ &\quad + \epsilon_{\text{V-B}} n_{\text{AB-B}} + \epsilon_{\text{A-AB}} n_{\text{A-V}} + \epsilon_{\text{AB-B}} n_{\text{V-B}} \end{aligned} \tag{2.10}$$

where $n_{\alpha\text{-}\beta}$ is numbers of bonds. Tracking the number of bonds in simulations takes extra computational effort, and also implies deviating from a purely Ising treatment. It is thus desirable to express $n_{\text{AB-AB}}$, $n_{\text{V-V}}$, $n_{\text{A-AB}}$, $n_{\text{AB-B}}$, $n_{\text{A-V}}$, and $n_{\text{V-B}}$ as summations of powers of the spin variables, as in eq. (2.8). In this fashion, the correction terms do not add any additional cost to the evaluation of the Hamiltonian but, instead, only alter the value of the coefficients in eq. (2.8). First, however, we must obtain expressions for all $n_{\alpha\text{-}\beta}$ in terms of the spin variable σ.

After discounting the $n_{\text{V-I}}$ terms (with I=AA, AB, BB), there are 18 $n_{\alpha\text{-}\beta}$ and therefore 18 independent equations are needed. 10 of them can be obtained from the summations of σ-polynomials:

$$\begin{aligned}\sum \sigma_i \sigma_j &= 4n_{\text{AA-AA}} + 2n_{\text{AA-A}} - 2n_{\text{AA-B}} - 4n_{\text{AA-BB}} + n_{\text{A-A}} + \\ &\quad - n_{\text{A-B}} - 2n_{\text{A-BB}} + n_{\text{B-B}} + 2n_{\text{B-BB}} + 4n_{\text{BB-BB}} \end{aligned} \tag{2.11}$$

$$\begin{aligned}\sum \sigma_i^2\sigma_j + \sigma_i\sigma_j^2 &= 16n_{\text{AA-AA}} + 6n_{\text{AA-A}} - 2n_{\text{AA-B}} + 2n_{\text{A-A}} + 2n_{\text{A-BB}} + \\ &\quad -2n_{\text{B-B}} - 6n_{\text{B-BB}} - 16n_{\text{BB-BB}} \qquad (2.12)\end{aligned}$$

$$\begin{aligned}\sum \sigma_i^2\sigma_j^2 &= 16n_{\text{AA-AA}} + 4n_{\text{AA-A}} + 4n_{\text{AA-B}} + 16n_{\text{AA-BB}} + n_{\text{A-A}} + \\ &\quad +n_{\text{A-B}} + 4n_{\text{A-BB}} + n_{\text{B-B}} + 4n_{\text{B-BB}} + 16n_{\text{BB-BB}} \qquad (2.13)\end{aligned}$$

$$\begin{aligned}\sum \sigma_i^3\sigma_j + \sigma_i\sigma_j^3 &= 32n_{\text{AA-AA}} + 10n_{\text{AA-A}} - 10n_{\text{AA-B}} - 32n_{\text{AA-BB}} + \\ &\quad +2n_{\text{A-A}} - 2n_{\text{A-B}} - 10n_{\text{A-BB}} + 2n_{\text{B-B}} + 10n_{\text{B-BB}} + \\ &\quad +32n_{\text{BB-BB}} \qquad (2.14)\end{aligned}$$

$$\begin{aligned}\sum \sigma_i^3\sigma_j^2 + \sigma_i^2\sigma_j^3 &= 64n_{\text{AA-AA}} + 12n_{\text{AA-A}} + 4n_{\text{AA-B}} + 2n_{\text{A-A}} - 4n_{\text{A-BB}} + \\ &\quad -2n_{\text{B-B}} - 12n_{\text{B-BB}} - 64n_{\text{BB-BB}} \qquad (2.15)\end{aligned}$$

$$\begin{aligned}\sum \sigma_i^3\sigma_j^3 &= 64n_{\text{AA-AA}} + 8n_{\text{AA-A}} - 8n_{\text{AA-B}} - 64n_{\text{AA-BB}} + n_{\text{A-A}} - n_{\text{A-B}} + \\ &\quad -8n_{\text{A-BB}} + n_{\text{B-B}} - 8n_{\text{B-BB}} + 64n_{\text{BB-BB}} \qquad (2.16)\end{aligned}$$

$$\begin{aligned}\sum \sigma_i^4\sigma_j + \sigma_i\sigma_j^4 &= 64n_{\text{AA-AA}} + 18n_{\text{AA-A}} - 14n_{\text{AA-B}} + 2n_{\text{A-A}} + \\ &\quad +14n_{\text{A-BB}} - 2n_{\text{B-B}} - 18n_{\text{B-BB}} - 64n_{\text{BB-BB}} \qquad (2.17)\end{aligned}$$

$$\begin{aligned}\sum \sigma_i^4\sigma_j^2 + \sigma_i^2\sigma_j^4 &= 128n_{\text{AA-AA}} + 20n_{\text{AA-A}} + 20n_{\text{AA-B}} + 128n_{\text{AA-BB}} + \\ &\quad +2n_{\text{A-A}} + 2n_{\text{A-B}} + 20n_{\text{A-BB}} + 2n_{\text{B-B}} + 20n_{\text{B-BB}} + \\ &\quad +128n_{\text{BB-BB}} \qquad (2.18)\end{aligned}$$

$$\begin{aligned}\sum \sigma_i^4\sigma_j^3 + \sigma_i^3\sigma_j^4 &= 256n_{\text{AA-AA}} + 24n_{\text{AA-A}} - 8n_{\text{AA-B}} + 2n_{\text{A-A}} + \\ &\quad +8n_{\text{A-BB}} - 2n_{\text{B-B}} - 24n_{\text{B-BB}} - 256n_{\text{BB-BB}} \qquad (2.19)\end{aligned}$$

$$\begin{aligned}\sum \sigma_i^4\sigma_j^4 &= 256n_{\text{AA-AA}} + 16n_{\text{AA-A}} + 16n_{\text{AA-B}} + 256n_{\text{AA-BB}} + n_{\text{A-A}} + \\ &\quad +n_{\text{A-B}} + 16n_{\text{A-BB}} + n_{\text{B-B}} + 16n_{\text{B-BB}} + 256n_{\text{BB-BB}} \qquad (2.20)\end{aligned}$$

However, the above equations do not contain any $n_{\alpha\text{-}\beta}$ with α or β= V, AB. Six more equations that do contain these terms can be obtained by counting the numbers of six species N_α:

$$zN_{\mathrm{AA}} = 2n_{\text{AA-AA}} + n_{\text{AA-A}} + n_{\text{AA-AB}} + n_{\text{AA-B}} + n_{\text{AA-BB}} \tag{2.21}$$

$$zN_{\mathrm{A}} = n_{\text{AA-A}} + 2n_{\text{A-A}} + n_{\text{A-V}} + n_{\text{A-AB}} + n_{\text{A-B}} + n_{\text{A-BB}} \tag{2.22}$$

$$zN_{\mathrm{V}} = n_{\text{A-V}} + 2n_{\text{V-V}} + n_{\text{V-B}} \tag{2.23}$$

$$zN_{\mathrm{AB}} = n_{\text{AA-AB}} + n_{\text{A-AB}} + 2n_{\text{AB-AB}} + n_{\text{AB-B}} + n_{\text{AB-BB}} \tag{2.24}$$

$$zN_{\mathrm{B}} = n_{\text{AA-B}} + n_{\text{A-B}} + n_{\text{V-B}} + n_{\text{AB-B}} + 2n_{\text{B-B}} + n_{\text{B-BB}} \tag{2.25}$$

$$zN_{\mathrm{BB}} = n_{\text{AA-BB}} + n_{\text{A-BB}} + n_{\text{AB-BB}} + n_{\text{B-BB}} + 2n_{\text{BB-BB}} \tag{2.26}$$

where z is the coordination number. Combining eqs. (2.11) through (2.26), we have 16 equations with 18 unknowns. In order to solve the system, we express everything parametrically in terms of two bond numbers, $n_{\text{AB-A}}$ and $n_{\text{AB-B}}$[1], and solve for the rest of the $n_{\alpha\text{-}\beta}$. $n_{\text{AB-A}}$ and $n_{\text{AB-B}}$ are then the only bond numbers that must be calculated on the fly in the kMC simulations.

2.1.2.2 The corrected Ising Hamiltonian.

After solving for all $n_{\alpha\text{-}\beta}$, the corrected Hamiltonian can be obtained by substituting eq. (2.10) into eq. (2.9). Except for an additional term C_0, the final expression of the corrected Hamiltonian is the same as the uncorrected one in eq. (2.8). However, the coefficients C_{mn} are now 'corrected' to account for the AB/V conflict. Based on the physical characteristics of each coefficient, each term in the Hamiltonian of the ABVI system can be grouped into

---

[1] This choice is justified both by the fact that neither A-AB nor AB-B bonds are very likely to appear in the simulations, and because –as will pointed out below– AB interstitialcy jumps are the likeliest to change the global concentration of species, which results in the need to update the non-configurational constants in the ABVI Hamiltonian (cf. eq. (2.27)).

three different configurational classes and one non-configurational group:

$$
\begin{aligned}
\mathcal{H}_{\text{corrected}} \;=\; & \sum_{\langle i,j\rangle}^{nn} \left[C_{44}\sigma_i^4\sigma_j^4 + C_{42}\left(\sigma_i^4\sigma_j^2 + \sigma_i^2\sigma_j^4\right) + C_{22}\sigma_i^2\sigma_j^2 \right] + \;\text{(Class 1)} \\
& + \sum_{\langle i,j\rangle}^{nn} \Big[C_{43}\left(\sigma_i^4\sigma_j^3 + \sigma_i^3\sigma_j^4\right) + C_{41}\left(\sigma_i^4\sigma_j + \sigma_i\sigma_j^4\right) + C_{32}\left(\sigma_i^3\sigma_j^2 + \sigma_i^2\sigma_j^3\right) + \\
& \qquad\quad + C_{21}\left(\sigma_i^2\sigma_j + \sigma_i\sigma_j^2\right) \Big] + \;\text{(Class 2)} \\
& + \sum_{\langle i,j\rangle}^{nn} \Big[C_{33}\sigma_i^3\sigma_j^3 + C_{31}\left(\sigma_i^3\sigma_j + \sigma_i\sigma_j^3\right) + C_{11}\sigma_i\sigma_j \Big] + \;\text{(Class 3)} \\
& + \sum_{\langle i,j\rangle}^{nn} [\; C_{40}\left(\sigma_i^4 + \sigma_j^4\right) + C_{30}\left(\sigma_i^3 + \sigma_j^3\right) + C_{20}\left(\sigma_i^2 + \sigma_j^2\right) + \\
& \qquad\quad + C_{10}\left(\sigma_i + \sigma_j\right) + C_{00} \;] + C_0 \;\text{(Non-configurational)}
\end{aligned}
\tag{2.27}
$$

where the coefficients C_{mn} are:

Class 1

$$
\begin{aligned}
C_{44} \;=\; & \frac{1}{576}\Big\{ \left(\epsilon_{\text{AA-AA}} - 8\epsilon_{\text{AA-A}} - 8\epsilon_{\text{AA-B}} + 2\epsilon_{\text{AA-BB}} - 8\epsilon_{\text{A-BB}} - 8\epsilon_{\text{B-BB}} + \epsilon_{\text{BB-BB}}\right) + \\
& + \left(12\epsilon_{\text{AA-AB}} - 12\epsilon_{\text{AB-AB}} + 12\epsilon_{\text{AB-BB}}\right) + \left(-48\epsilon_{\text{A-V}} + 48\epsilon_{\text{V-V}} - 48\epsilon_{\text{V-B}}\right) + \\
& + \left(16\epsilon_{\text{A-A}} + 32\epsilon_{\text{A-B}} + 16\epsilon_{\text{B-B}}\right) \Big\} \\
C_{42} \;=\; & \frac{1}{576}\Big\{ \left(-\epsilon_{\text{AA-AA}} + 20\epsilon_{\text{AA-A}} + 20\epsilon_{\text{AA-B}} - 2\epsilon_{\text{AA-BB}} + 20\epsilon_{\text{A-BB}} + 20\epsilon_{\text{B-BB}} - \epsilon_{\text{BB-BB}}\right) + \\
& + \left(-36\epsilon_{\text{AA-AB}} + 36\epsilon_{\text{AB-AB}} - 36\epsilon_{\text{AB-BB}}\right) + \left(216\epsilon_{\text{A-V}} - 216\epsilon_{\text{V-V}} + 216\epsilon_{\text{V-B}}\right) + \\
& + \left(-64\epsilon_{\text{A-A}} - 128\epsilon_{\text{A-B}} - 64\epsilon_{\text{B-B}}\right) \Big\} \\
C_{22} \;=\; & \frac{1}{576}\Big\{ \left(\epsilon_{\text{AA-AA}} - 32\epsilon_{\text{AA-A}} - 32\epsilon_{\text{AA-B}} + 2\epsilon_{\text{AA-BB}} - 32\epsilon_{\text{A-BB}} - 32\epsilon_{\text{B-BB}} + \epsilon_{\text{BB-BB}}\right) + \\
& + \left(60\epsilon_{\text{AA-AB}} - 60\epsilon_{\text{AB-AB}} + 60\epsilon_{\text{AB-BB}}\right) + \left(-960\epsilon_{\text{A-V}} + 960\epsilon_{\text{V-V}} - 960\epsilon_{\text{V-B}}\right) + \\
& + \left(256\epsilon_{\text{A-A}} + 512\epsilon_{\text{A-B}} + 256\epsilon_{\text{B-B}}\right) \Big\}
\end{aligned}
$$

Class 2

$$
\begin{aligned}
C_{43} &= \frac{1}{288}\Big\{ (\epsilon_{\text{AA-AA}} - 6\epsilon_{\text{AA-A}} - 2\epsilon_{\text{AA-B}} + 2\epsilon_{\text{A-BB}} + 6\epsilon_{\text{B-BB}} - \epsilon_{\text{BB-BB}}) + \\
&\quad + (6\epsilon_{\text{AA-AB}} - 6\epsilon_{\text{AB-BB}}) + (-12\epsilon_{\text{A-V}} + 12\epsilon_{\text{V-B}}) + (8\epsilon_{\text{A-A}} - 8\epsilon_{\text{B-B}}) \Big\} \\
C_{41} &= \frac{1}{288}\Big\{ (-\epsilon_{\text{AA-AA}} + 12\epsilon_{\text{AA-A}} - 4\epsilon_{\text{AA-B}} + 4\epsilon_{\text{A-BB}} - 12\epsilon_{\text{B-BB}} + \epsilon_{\text{BB-BB}}) + \\
&\quad + (-6\epsilon_{\text{AA-AB}} + 6\epsilon_{\text{AB-BB}}) + (48\epsilon_{\text{A-V}} - 48\epsilon_{\text{V-B}}) + (-32\epsilon_{\text{A-A}} + 32\epsilon_{\text{B-B}}) \Big\} \\
C_{32} &= \frac{1}{288}\Big\{ (-\epsilon_{\text{AA-AA}} + 18\epsilon_{\text{AA-A}} + 14\epsilon_{\text{AA-B}} - 14\epsilon_{\text{A-BB}} - 18\epsilon_{\text{B-BB}} + \epsilon_{\text{BB-BB}}) + \\
&\quad + (-30\epsilon_{\text{AA-AB}} + 30\epsilon_{\text{AB-BB}}) + (60\epsilon_{\text{A-V}} - 60\epsilon_{\text{V-B}}) + (-32\epsilon_{\text{A-A}} + 32\epsilon_{\text{B-B}}) \Big\} \\
C_{21} &= \frac{1}{288}\Big\{ (\epsilon_{\text{AA-AA}} - 24\epsilon_{\text{AA-A}} - 8\epsilon_{\text{AA-B}} + 8\epsilon_{\text{A-BB}} + 24\epsilon_{\text{B-BB}} - \epsilon_{\text{BB-BB}}) + \\
&\quad + (30\epsilon_{\text{AA-AB}} - 30\epsilon_{\text{AB-BB}}) + (-240\epsilon_{\text{A-V}} + 240\epsilon_{\text{V-B}}) + (128\epsilon_{\text{A-A}} - 128\epsilon_{\text{B-B}}) \Big\}
\end{aligned}
$$

Class 3

$$
\begin{aligned}
C_{33} &= \frac{1}{144}\Big\{ (\epsilon_{\text{AA-AA}} - 4\epsilon_{\text{AA-A}} + 4\epsilon_{\text{AA-B}} - 2\epsilon_{\text{AA-BB}} + 4\epsilon_{\text{A-BB}} - 4\epsilon_{\text{B-BB}} + \epsilon_{\text{BB-BB}}) + \\
&\quad + (4\epsilon_{\text{A-A}} - 8\epsilon_{\text{A-B}} + 4\epsilon_{\text{B-B}}) \Big\} \\
C_{31} &= \frac{1}{144}\Big\{ (-\epsilon_{\text{AA-AA}} + 10\epsilon_{\text{AA-A}} - 10\epsilon_{\text{AA-B}} + 2\epsilon_{\text{AA-BB}} - 10\epsilon_{\text{A-BB}} + 10\epsilon_{\text{B-BB}} - \epsilon_{\text{BB-BB}}) + \\
&\quad + (-16\epsilon_{\text{A-A}} + 32\epsilon_{\text{A-B}} - 16\epsilon_{\text{B-B}}) \Big\} \\
C_{11} &= \frac{1}{144}\Big\{ (\epsilon_{\text{AA-AA}} - 16\epsilon_{\text{AA-A}} + 16\epsilon_{\text{AA-B}} - 2\epsilon_{\text{AA-BB}} + 16\epsilon_{\text{A-BB}} - 16\epsilon_{\text{B-BB}} + \epsilon_{\text{BB-BB}}) + \\
&\quad + (64\epsilon_{\text{A-A}} - 128\epsilon_{\text{A-B}} + 64\epsilon_{\text{B-B}}) \Big\}
\end{aligned}
$$

Non-Configurational

$$\begin{aligned}
C_{40} &= \frac{1}{24}\Big\{ (\epsilon_{\text{AA-AB}} + \epsilon_{\text{AB-BB}}) + (-4\epsilon_{\text{A-AB}} + 6\epsilon_{\text{AB-AB}} - 4\epsilon_{\text{AB-B}}) + \\
&\quad + (-4\epsilon_{\text{A-V}} + 6\epsilon_{\text{V-V}} - 4\epsilon_{\text{V-B}}) \Big\} \\
C_{30} &= \frac{1}{12}\Big\{ (\epsilon_{\text{AA-AB}} - \epsilon_{\text{AB-BB}}) + (-2\epsilon_{\text{A-AB}} + 2\epsilon_{\text{AB-B}}) + (-2\epsilon_{\text{A-V}} + 2\epsilon_{\text{V-B}}) \Big\} \\
C_{20} &= \frac{1}{24}\Big\{ (-\epsilon_{\text{AA-AB}} - \epsilon_{\text{AB-BB}}) + (16\epsilon_{\text{A-AB}} - 30\epsilon_{\text{AB-AB}} + 16\epsilon_{\text{AB-B}}) + \\
&\quad + (16\epsilon_{\text{A-V}} - 30\epsilon_{\text{V-V}} + 16\epsilon_{\text{V-B}}) \Big\} \\
C_{10} &= \frac{1}{12}\Big\{ (-\epsilon_{\text{AA-AB}} + \epsilon_{\text{AB-BB}}) + (8\epsilon_{\text{A-AB}} - 8\epsilon_{\text{AB-B}}) + (8\epsilon_{\text{A-V}} - 8\epsilon_{\text{V-B}}) \Big\} \\
C_{00} &= (\epsilon_{\text{AB-AB}} + \epsilon_{\text{V-V}}) \\
C_{0} &= \frac{n_{\text{A-AB}}}{2}(-\epsilon_{\text{AB-AB}} + 2\epsilon_{\text{A-AB}} - 2\epsilon_{\text{A-V}} + \epsilon_{\text{V-V}}) + \\
&\quad + \frac{n_{\text{AB-B}}}{2}(-\epsilon_{\text{AB-AB}} + 2\epsilon_{\text{AB-B}} - 2\epsilon_{\text{V-B}} + \epsilon_{\text{V-V}}) + \\
&\quad + \frac{Z}{2}\left[N_A(\epsilon_{\text{AB-AB}} - 2\epsilon_{\text{A-AB}}) + N_B(\epsilon_{\text{AB-AB}} - 2\epsilon_{\text{AB-B}})\right] + \\
&\quad - \frac{Z}{2}\left[N_V\epsilon_{\text{AB-AB}} + N_{AA}\epsilon_{\text{V-V}} - N_{AB}\epsilon_{\text{V-V}} + N_{BB}\epsilon_{\text{V-V}}\right]
\end{aligned}$$

This way of grouping the C_{mn} is not unique. We have chosen the three classes above to represent a given physical behavior along the lines of the coefficients K, U, J of the ABV Ising model. Loosely speaking, the physical meanings of each of the three classes is as follows:

- Class 1 (even-even power terms) gives the relative importance of interactions between point defects (vacancies and interstitials).
- Class 2 (even-odd power terms) gives the affinity between atoms and point defects.
- Class 3 (odd-odd power terms) determines the equilibrium phase diagram.

In the standard ABV model, defect (vacancy) hops do not change the global species concentrations. That means that the *non-configurational* class of terms in the Hamiltonian (2.27) does not change merely by vacancy jumps. However, the ABVI model now allows for defect transitions that change the global balance of species [2]. Specifically, there are two

---

[2] The most obvious one being a vacancy-interstitial recombination.

types of transitions that affect the species concentrations when they occur. The first one involves vacancy-interstitial recombinations:

$$\text{AA+V} \rightarrow \text{A} + \text{A}$$

$$\text{AB+V} \rightarrow \text{A} + \text{B}$$

$$\text{BB+V} \rightarrow \text{B} + \text{B}$$

The second type is related to the *interstitialcy* mechanism, by which an interstitial atom displaces an atom from an adjacent lattice position so that it becomes the interstitial in its turn, able to displace another atom. This mechanism includes four reactions:

$$\text{AA} + \text{B} \rightarrow \text{A} + \text{AB}$$

$$\text{AB} + \text{A} \rightarrow \text{B} + \text{AA}$$

$$\text{AB} + \text{B} \rightarrow \text{A} + \text{BB}$$

$$\text{BB} + \text{A} \rightarrow \text{B} + \text{AB}$$

Except when one of the above reactions occurs, the incremental energy formulation used to compute energy differences between the initial and final states allows us to discard the non-configurational terms during calculations.

In order to truly represent a generalized Hamiltonian, the ABVI model Hamiltonian must reduce to the AV and ABV models in their respective limits (AV: no solute, vacancies; ABV: solute plus vacancies). Indeed, we have conducted verification tests of both particular cases and we have found matching results. This is the subject of Sec. 2.2, where we have simulated the time evolution of AB, ABV and ABVI systems using the generalized Hamiltonian presented above. Our method of choice is kinetic Monte Carlo (kMC), which we describe in detail in the following section.

2.1.3 Kinetic Monte Carlo Simulation

In this section we discuss relevant details of the kMC simulation method in relation to our extended ABVI model. All simulations are conducted on a rigid lattice generated from trigonal (primitive) representations of face-centered cubic (FCC) and body-centered cubic (BCC) crystals. The primitive cells employed for each crystal structure are provided in Figure 2.1. The simulations are generally conducted in the grand canonical ensemble, to allow for irradiation damage simulations when required [CS63]. All kinetic transitions are assumed to be due to defect hops. In particular, we consider the vacancy and interstitialcy mechanisms to enable atomic transport. After every transition, the configuration of the system is updated and a new transition is considered.

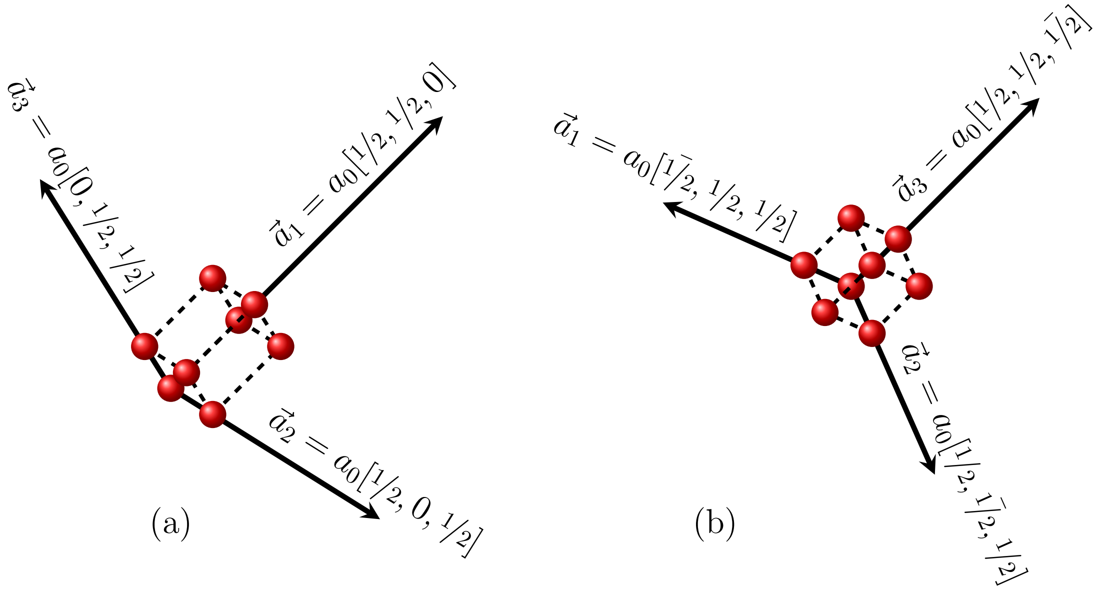

(a) (b)

Figure 2.1: Primitive cells for (a) FCC and (b) BCC lattices showing all eight vertices as red spheres. The vectors $\vec{a_1}$, $\vec{a_2}$, and $\vec{a_3}$ are primitive basis of crystal, with a_0 the lattice parameter.

2.1.3.1 Residence-time algorithm.

We use the residence-time algorithm (RTA) [YE66] to track the kinetic evolution of the system through a series of thermally activated transitions. The transition rates R_{ij} connecting an initial state i to a final state j are calculated as:

$$r_{ij} = \nu \exp\left(-\frac{\Delta E_{ij}}{k_B T}\right) \tag{2.28}$$

where $\Delta E_{ij} > 0$ is an activation energy that will be discussed below, ν is the attempt frequency, and $1/k_B T$ is the reciprocal temperature. With the system in configuration i, an event is randomly chosen with a probability proportional to its rate, and the time advanced per kMC step is on average $\delta t_i = \left(\sum_j r_{ij}\right)^{-1}$. In addition to thermally activated transitions such as those represented by eq. (2.28), we consider spontaneous events –for which, strictly speaking, ΔE_{ij} may be negative– such as recombination between vacancies and interstitials, absorption at sinks, etc. These events occur instantaneously with $\delta t = 0$.

2.1.3.2 Activation energy models.

There are several models proposed to describe the activation energy, which are based on different interpretations of the atomic migration process (see for e.g., [SBC10] for a recent review). The first model is the so-called *saddle-point energy* model (also known as 'cut-bond' model in [VBP08]) [SBM96, BS02, SF07]. The activation energy is given by:

$$\Delta E_{ij} = E_{XY}^{SP} - \sum_{n} \epsilon_{X\text{-}n} - \sum_{p \neq X} \epsilon_{Y\text{-}p} \tag{2.29}$$

where Y refers to the defect (e.g. a vacancy) and X to the atom exchanging positions with Y. The later two summations are the bonding energies between X, Y and the adjacent neighbor sites n and p and represent the energy of the system at the initial state. These summations can be computed using the ABVI formulas described in Section 2.1.1. The saddle-point energy E_{XY}^{SP} is generally taken to be a constant [SBM96], or is computed as a especial sum of bond energies of the jumping atom at the saddle point: $E_{XY}^{SP} = \sum_q \epsilon_{Xq}^{SP,Y}$, where the subindex q represents the local neighbors of the jumping atom [BS02, SF07].

The second model is the so-called *kinetic Ising model* [DMD07, RMO11] (or *final-initial system energy*, as is referred to by Vincent et al. [VBP08]). In this model, the activation energy is dependent on the energy difference of the system $\Delta\mathcal{H}_{ij}$ between the initial i and final states j, as well as a migration energy E_m, which is a constant determined by the type of defect-atom exchange. Two different forms of activation energy are proposed within this model. The first form is given by [RMO11]:

$$\Delta E_{ij} = \begin{cases} E_m + \Delta\mathcal{H}_{ij}, & \text{if } \Delta\mathcal{H}_{ij} > 0 \\ E_m, & \text{if } \Delta\mathcal{H}_{ij} < 0 \end{cases} \tag{2.30}$$

This form assumes that the energy barrier of transitions from higher to lower energy states is the migration energy E_m, and $E_m + \Delta\mathcal{H}_{ij}$ otherwise. An alternative, which is used in this work, is given by [VBP08, DMD07]:

$$\Delta E_{ij} = E_m + \frac{\Delta\mathcal{H}_{ij}}{2} \tag{2.31}$$

In this case, the migration energy is considered to be the energy difference between the saddle point and the average energy between states i and j, $E_m = E^{SP} - (\mathcal{H}_i + \mathcal{H}_j)/2$. This definition of E_m results in an expression for ΔE_{ij} that does not depend of the final state energy $\mathcal{H}_j$. A schematic diagram showing the different activation energy models discussed here is provided in Fig. 2.2. It can be shown that all the three activation energy models satisfy the detailed balance condition, *i*.e.:

$$\frac{r_{ij}}{r_{ji}} = \exp\left(-\frac{\Delta\mathcal{H}_{ij}}{k_B T}\right) \tag{2.32}$$

The different characteristics of each of these models have been discussed in detail by Soisson et al. [SBC10]. In the saddle-point energy model, the height of the energy barrier is not dependent on the energy of the final state, which agrees with the theory of thermally-activated processes. Also, the energy barrier dependence on configurations can be fitted directly from empirical potentials or ab initio calculations. Recently, a more realistic saddle-point energy model has been proposed, where the migration energy depends on the local solute concentration [MSF12, SSM16]. This model requires a larger parameter database, with the consequent extra cost in atomistic calculations or experimental parameterization. For its part, the kinetic Ising model assumes that the migration energy depends on the average of the energy difference between the initial and final states. This approach links the energy barrier to the local chemical environment, with the advantage that no knowledge of the saddle-point energy is required. It is also possible to evaluate energy barrier of events other than defect jumps such as recombination and surface reactions (defect annihilation and vacancy creation), described below in Sec. 2.1.3.4.

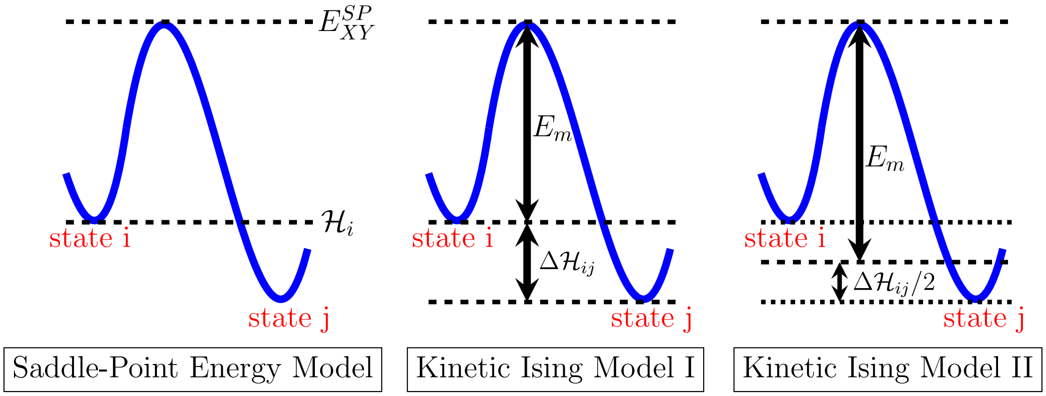

Figure 2.2: The three different models of activation energy

2.1.3.3 Computing bond energies from electronic-structure calculations.

Bond energies to parameterize eq. (2.27) and its associated constants C_{mn} can be calculated using a suitable atomistic force fields such as semi-empirical potentials, density-functional theory (DFT), etc. Considering 2^{nd}-nn interactions, the following parameters can be used to write a set of equations from which to calculate the bond energies:

- The cohesive energy of the pure metal A or B can be written as:

$$E^{\mathrm{A}}_{coh} = -\frac{z_1}{2}\epsilon^{(1)}_{\text{A-A}} - \frac{z_2}{2}\epsilon^{(2)}_{\text{A-A}} \tag{2.33}$$

$$E^{\mathrm{B}}_{coh} = -\frac{z_1}{2}\epsilon^{(1)}_{\text{B-B}} - \frac{z_2}{2}\epsilon^{(2)}_{\text{B-B}} \tag{2.34}$$

  where z_1 and z_2 are coordination numbers of the first and second nearest neighbor shells, and the superindex $^{(i)}$ refers to the nn shell. Care must be exercised when computing each cohesive energy to ensure that the crystal lattice corresponds to the equilibrium crystal lattice at the desired temperature.

- The pair interactions between an A atom and a B atom $\epsilon_{\text{A-B}}$ can be obtained from the enthalpy of mixing:

$$E_{mix} = -\frac{z_1}{2}\left(\epsilon^{(1)}_{\text{A-A}} + \epsilon^{(1)}_{\text{B-B}} - 2\epsilon^{(1)}_{\text{A-B}}\right) - \frac{z_2}{2}\left(\epsilon^{(2)}_{\text{A-A}} + \epsilon^{(2)}_{\text{B-B}} - 2\epsilon^{(2)}_{\text{A-B}}\right) \tag{2.35}$$

- The formation energy of vacancy is calculated by removing an atom from a perfect lattice position and putting it on the surface of the system. For a vacancy in a perfect A-atom matrix containing N lattice sites:

$$E^{\mathrm{V}}_{f} = NE^{\mathrm{A}}_{coh} - (N-1)E^{\mathrm{A}}_{coh} + z_1\epsilon^{(1)}_{\text{A-V}} + z_2\epsilon^{(2)}_{\text{A-V}} \tag{2.36}$$

- Similarly, the formation energy of an interstitial pair in an A-atom matrix can be written as:

$$E^{\mathrm{I}}_{f} = E^{\mathrm{A}}_{coh} + z_1\epsilon^{(1)}_{\text{A-I}} + z_2\epsilon^{(2)}_{\text{A-I}} \tag{2.37}$$

  where I= AA, AB, BB.

2.1.3.4 Events.

In kMC the kinetic evolution is determined by a series of independent events that represent state transitions. Within the ABVI model, we consider five distinct types of events mediated by point defect mechanisms, discussed below.

1. *Defect jumps*: vacancies move by exchanging positions with one of the z_1 1^{st} *nn* atoms:

   $$\mathrm{V} + a \rightarrow a + \mathrm{V}$$

   where a=A, B. Interstitials, for their part, move via the interstitialcy mechanism introduced above. They can adopt either the *dumbbell* or *crowdion* structure, *i*.e. two atoms sharing one lattice site:

   $$\mathrm{I}(a_1\text{-}a_2) + a_1 \rightarrow a_1 + \mathrm{I}(a_2\text{-}a_1)$$

   where an interstitial composed of two atoms a_1 and a_2 (a_1, a_2=A,B) jumps into a neighboring lattice site occupied by atom a_1, giving rise to a new interstitial composed of atoms a_2 and a_1.

2. *Recombination:* when a vacancy and an interstitial are found within a distance less than a critical distance r_c, a recombination event occurs. The generic reaction is:

   $$\mathrm{I}(a_1\text{-}a_2) + V \rightarrow a_1 + a_2$$

   Recombinations events occur spontaneously, with $\delta t = 0$.

3. *Annihilation at defect sinks*: in this work two types of defect sinks are used. The first one, as suggested by Soisson [Soi06], is a thin slab of the simulation box designed to act as a perfect defect sink (a simple model of grain boundary). When a defect jumps into a lattice position belonging to the slab, it instantly disappears. To preserve the alloy composition, a 'reservoir' is used such that when a vacancy is absorbed at the sink, an atom is randomly chosen from the reservoir and placed at the sink site; for interstitials, one of the two atoms is randomly chosen and stored in the reservoir; the other atom remains on the sink site. Another inexhaustible sink is a free surface. The lattice beyond the free surface is considered to be part of a 'vacuum' such that atoms adjacent to vacuum lattice sites are defined as 'surface atoms'. When a vacancy jumps onto a site occupied by a surface atom, it first switches its position with the atom, and then the vacancy becomes a vacuum site:

   $$\mathrm{V} + a_s \rightarrow a_s + v$$

where a_s refers to a surface atom, and v is a vacuum site. The mechanism for interstitial annihilation is more complex. When an interstitial jumps onto a surface atom site, an instantaneous recombination between the interstitial and the vacuum site occurs (vacuum sites are a special class of vacancies). The reaction can be described as:

$$\mathrm{I}(a_1\text{-}a_2) + v \rightarrow a_1 + a_2$$

4. *Thermal vacancy emission*: material inhomogeneities such as surfaces, grain boundaries, dislocations, etc, can act as thermal sources of defects. Due to the relatively high energy of interstitial defects compared to vacancies, interstitial emission is often considered negligible. A thermal emission can be regarded as the inverse of a vacancy annihilation event. For a free surface, a vacancy is created just below the surface by having a vacuum site exchange positions with a surface atom:

   $$v + a_s \rightarrow a_s + \mathrm{V}$$

   The rate of vacancy emission can become sizable at high temperature, and should not be discarded as an efficient vacancy generation mechanism with a strong effect on the system kinetics.

5. *Frenkel pair generation*: when considering irradiation with light particles (e.g., electrons), V-I pairs are generated in the lattice. As implemented in our method, when a Frenkel pair insertion occurs, two lattice sites are randomly chosen, one becomes a vacancy and the other becomes an interstitial formed by the two atoms involved:

   $$a_1 + a_2 \rightarrow \mathrm{V} + \mathrm{I}(a_1\text{-}a_2)$$

   Frenkel pairs are introduced at a rate consistent with the imposed irradiation dose rate (usually measured in displacements per atom per second, or dpa·s^{-1}).

A compilation of all the reactions and events discussed in this section is provided in Table 2.1.

Table 2.1: Event reactions considered in this work. V: vacancy, A: matrix atom, B: solute atom, AA: self interstitial, AB: mixed interstitial, BB: pure solute interstitial, v: vacuum atom, A$_s$: surface matrix atom, B$_s$: surface solute atom.

Vacancy jumps	Interstitial jumps	Recombinations	Frenkel pair generation
V+A→A+V	AA+A→A+AA	AA+V→A+A	A+A→AA+V
V+B→A+B	AA+B→B+AA	AB+V→A+B	A+B→AB+V
	BB+A→B+AB	BB+V→B+B	B+B→BB+V
	BB+B→B+BB		
	$\mathrm{AB+A}\to\begin{cases}\mathrm{A+AB}\\ \mathrm{B+AA}\end{cases}$		
	$\mathrm{AB+B}\to\begin{cases}\mathrm{A+BB}\\ \mathrm{B+AB}\end{cases}$		

Defect annihilation		Thermal emission
Ideal sink	Surface	
V→A	V+A$_s$→A$_s$+v	v+A$_s$→A$_s$+V
V→B	V+B$_s$→B$_s$+v	v+B$_s$→B$_s$+V
AA→A	AA+v→A+A$_s$	
BB→B	BB+v→B+B$_s$	
$\mathrm{AB}\to\begin{cases}A\\ B\end{cases}$	$\mathrm{AB}+v\to\begin{cases}\mathrm{A+B}_s\\ \mathrm{B+A}_s\end{cases}$	

2.2 Results

This section consists of various verification checks undertaken to ensure the correctness of our approach. The first tests are designed to check the 'downward' consistency of our model, *i*.e. comparing against AV and ABV models with reduced complexity w.r.t. the ABVI Hamiltonian. Subsequently, we compare our method with KMC simulations of three different ABVI systems published in the literature. In all simulations, atoms are initially assigned randomly to lattice sites so as to achieve a perfect solid solution as a starting configuration.

2.2.1 AV system: Nanovoid formation in pure Al

An AV case, studied by Reina et al. [RMO11], was first trivially reproduced. Pure aluminum with vacancy concentration of 0.1at% at 700 K is simulated. The simulation box size is set to be 100^3. Fig. (2.3) shows the results of number densities of clusters with different sizes as a function of time. The results are consistent with Reina et al. work.

2.2.2 ABV system: Precipitation of Fe-Cu alloys

We simulate the system considered by Vincent et al. [VBP08]: a Fe-0.6% at. Cu alloy occupying a periodic BCC lattice arranged into computational box with $80 \times 80 \times 80$ primitive cells containing 512,000 atoms and a single vacancy. The Hamiltonian includes 2^{nd}-nn interactions with energy coefficients given in Table 2.2. The energies of mixing for 1^{st} and 2^{nd}-nn are 0.26 and 0.24 eV, which suggest a strong tendency toward phase separation [Gas08]. The temperature is fixed at 773 K. During the simulations, the vacancy may become trapped in solute precipitates, which does not result in net microstructural evolution and may stall the simulations. To correct for this, Vincent et al. proposed to increment the kMC time only

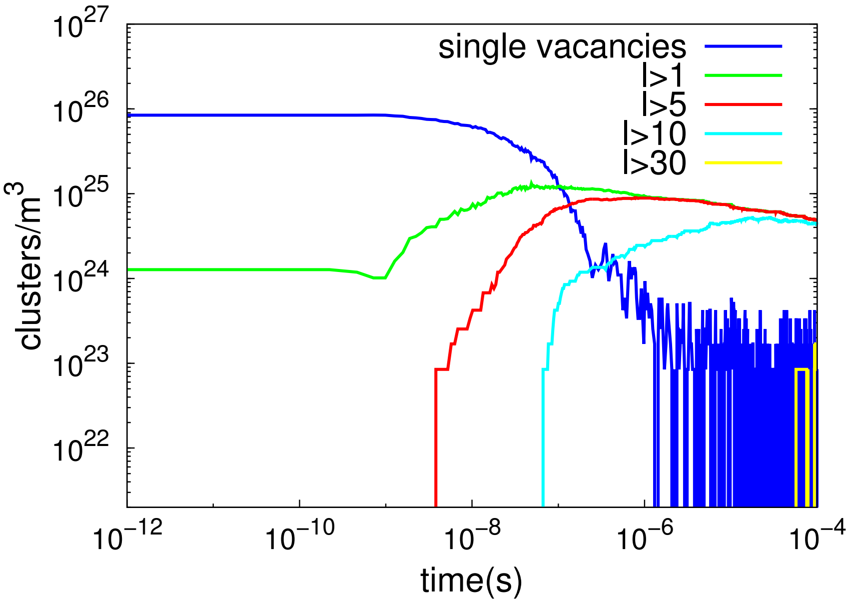

Figure 2.3: Number densities of clusters with different sizes as a function of time. The results consistent with Reina et al. work [VBP08]

when the vacancy is surrounded by at most one solute atom. As well, to account for an unrealistically high vacancy concentration, the kMC time step is rescaled according to:

$$\delta t = \frac{C_{\mathrm{V}}^{\mathrm{kMC}}}{C_{\mathrm{V}}^{0}} \delta t_{\mathrm{kMC}} \tag{2.38}$$

where $C_{\mathrm{V}}^{0} = \exp\left(-E_{f}^{\mathrm{V}}/k_{B}T\right)$ is the thermodynamic vacancy concentration. The rescaling factor in eq. (2.38) only reflects the true time acceleration when there is no solute present, or while there is no precipitation. When the system is undergoing precipitation, the vacancy concentration is environment-dependent and must be updated as the simulation progresses [NS12]. Alternatively, rescaling can be avoided by introducing a vacancy source/sink, which has recently been proposed [GMM01, MGL01, HWN09, Hin09, HDC10]. However, using a vacancy source/sink requires that an exchange energy be defined, which introduces another source of uncertainty. Vincent et al. adjust their kMC timescale by comparing the kinetic evolution directly with experiments. Specifically, they matched a cluster mean radius of 0.9 nm in their simulations to a time of 7200 s. For consistency, we adopt the same approach here. The initial and final configurations are shown in Fig. 2.4. The kinetic evolution of precipitation is quantified by calculating the cluster mean radius of solute atoms as a

Table 2.2: Bond energies for the Fe-Cu ABV system. A represents Fe atoms, B Cu atoms, and V is the vacancy.

1$^{\text{st}}$-*nn* interactions (eV)					Migration energy (eV)	
$\epsilon^{(1)}_{\text{A-A}}$	$\epsilon^{(1)}_{\text{A-B}}$	$\epsilon^{(1)}_{\text{B-B}}$	$\epsilon^{(1)}_{\text{A-V}}$	$\epsilon^{(1)}_{\text{B-V}}$	E_m^{V-A}	E_m^{V-B}
-0.611	-0.480	-0.414	-0.163	-0.102	0.62	0.54
2$^{\text{nd}}$-*nn* interactions (eV)					Jump frequency (s^{-1})	
$\epsilon^{(2)}_{\text{A-A}}$	$\epsilon^{(2)}_{\text{A-B}}$	$\epsilon^{(2)}_{\text{B-B}}$	$\epsilon^{(2)}_{\text{A-V}}$	$\epsilon^{(2)}_{\text{B-V}}$	$\nu^{\text{V}}_{\text{A}}$	$\nu^{\text{V}}_{\text{B}}$
-0.611	-0.571	-0.611	-0.163	-0.180	6×10^{12}	6×10^{12}

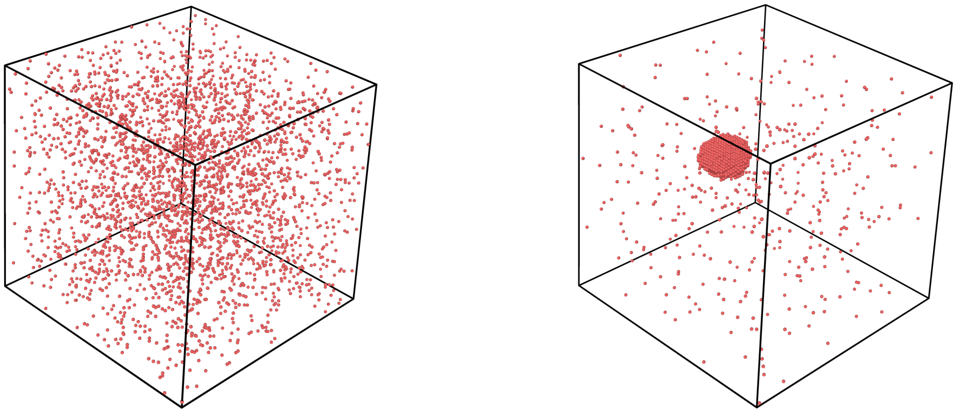

(a) (b)

Figure 2.4: Initial (a), $t = 0$, and final (b), $t = 28368$ s alloy configurations. The red dots represent solute atoms (B atoms). Solvent atoms and the vacancy are omitted for clarity.

function of time. It is assumed that a B atom belongs to a cluster if one of its 1$^{\text{st}}$-*nn* is also a B atom of the cluster. The cluster size is computed assuming a spherical shape from the expression [SB02]:

$$\bar{R} = a_0 \left(\frac{3N}{8\pi} \right)^{\frac{1}{3}} \tag{2.39}$$

where $\bar{R}$ is the cluster mean radius, N is the number of solute atoms in the cluster, and a_0 is the lattice constant of the BCC lattice. As in ref. [VBP08], clusters containing three or less atoms are not counted towards the calculation of $\bar{R}$. To capture the statistical variability of the simulations, we perform five independent runs under the same conditions and extract the time evolution of the average value of $\bar{R}$. Error bars are extracted by calculating the standard deviation for a representative data point subset consisting of 31 points. Our results are provided in Figure 2.5, together with the data of Vincent et al. After taking into account statistical errors and simulation conditions, it can be seen that Vincent et al.'s results are generally within the error bars of our simulations. With this, we consider our Hamiltonian sufficiently verified for the ABV system.

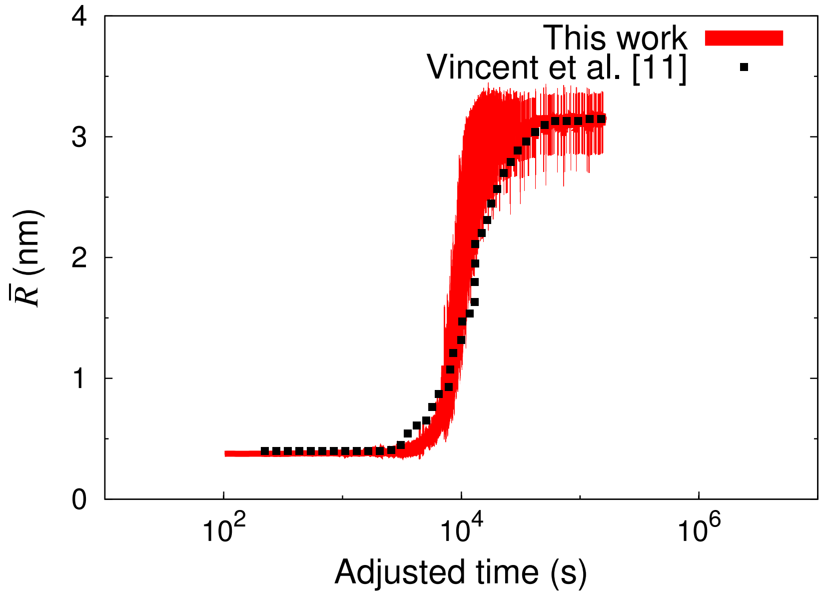

Figure 2.5: The cluster mean radius of the ABV Fe-Cu system. The red line represents the results in this work; the black filled squares are the data from Vincent et al. [VBP08]

2.2.3 ABVI system: Solute segregation at sinks

In this test, we reproduce the work of Soisson [Soi06]. The system consists of a BCC $256 \times 64 \times 64$ triclinic crystal lattice containing an A-5%B alloy, vacancies and interstitials defects. A perfect planar defect sink is placed in the middle of the crystal and kMC simulations of (radiation-induced) segregation at the defect sink are performed. Frenkel pairs are generated at a rate of $G = 10^{-6}$ dpa·s^{-1} following the mechanism described in Sec. 2.1.3.4.

Segregation at the sinks is governed by the onset of solute fluxes in the system. These fluxes are mediated by defect migration to and absorption at the sink. The solute flux can be controlled by setting the defect migration energies such that exchanges with B atoms are preferred over exchanges with A atoms (or vice versa), resulting in enrichment or depletion of solute at the defect sink. While Soisson uses a saddle-point model to obtain the activation energy (cf. Sec. 2.1.3.2), our implementation of the ABVI Hamiltonian has been designed to employ a kinetic Ising model. In order to make both approaches as close to one another as possible, we use Soisson's bond energies directly and adjust the migration energies E_m so as to match the kinetic evolution. The parameters used are shown in Table 2.3. There are four sets of parameters. The first two, ABVI-1 and ABVI-2, correspond to a system with relatively low energy of mixing ($E_{mix} = 0.216$ eV), representing undersaturated solid solutions with high solubility limits. The other two, ABVI-3 and ABVI-4 correspond to a system with $E_{mix} = 0.680$ eV leading to supersaturated solid solutions. Systems ABVI-1 and ABVI-3 are such that a net flux of B atoms develops toward the sink ($E_m^{\text{V-A}} < E_m^{\text{V-B}}$; $E_m^{\text{I-A}} > E_m^{\text{I-B}}$), whereas ABVI-2 and ABVI-4 result in solute depletion at the sink –the so-called *inverse Kirkendall* effect–($E_m^{\text{V-A}} > E_m^{\text{V-B}}$; $E_m^{\text{I-A}} < E_m^{\text{I-B}}$). For simplicity, migration energies of vacancies and interstitials are set to produce the same segregation tendency for each set of parameters. Other details considered by Soisson, such as recombination radii, event sampling, etc., are also followed here[3]. The spatial solute concentration profiles are shown in Fig. 2.6.

In the undersaturated alloy, no precipitation in the bulk is observed. As the dose increases, the concentration of B atoms near the sink is enhanced (reduced) for the enrichment (depletion) parameter set. For the enrichment case ABVI-1, a solute concentration drop at the center of the system is observed. This can rationalized in terms of interstitialcy jumps. After the solute concentration raises near the sink, interstitials must traverse a solute-rich region in order to reach the sink. As interstitials penetrate the near-sink region, they will increasingly become of the AB type. Because $\epsilon_{\text{A-B}} > \epsilon_{\text{B-B}}$, A atoms located in this solute-rich

---

[3] With one exception: the Frenkel pair distance is not set in this work.

Table 2.3: Parameters for the ABVI system (after Soisson [Soi06]). ‘A’ and ‘B’ denote solvent and solute atoms, respectively. ‘V’ represents vacancies and ‘I’ all types of interstitial defects. All energies given in eV. Attempt frequencies given in Hz.

Kinetic parameters	ABVI-1	ABVI-2	ABVI-3	ABVI-4
	high solubility		low solubility	
	enrichment	depletion	enrichment	depletion
$\nu_{\text{A}}^{\text{V}} = \nu_{\text{B}}^{\text{V}} = \nu_{\text{A}}^{\text{I}} = \nu_{\text{B}}^{\text{I}}$	5×10^{15}	5×10^{15}	5×10^{15}	5×10^{15}
$\epsilon_{\text{A-A}} = \epsilon_{\text{B-B}}$	-1.07	-1.07	-1.07	-1.07
$\epsilon_{\text{A-B}}$	-1.043	-1.043	-0.985	-0.985
$\epsilon_{\text{A-V}} = \epsilon_{\text{B-V}}$	-0.3	-0.3	-0.3	-0.3
$\epsilon_{A\text{-}I} = \epsilon_{B\text{-}I}$	0	0	0	0
E_m^{V-A}	0.95	1.1	0.8	1.05
$E_m^{\text{V-B}}$	1.05	0.9	1.2	0.95
$E_m^{\text{I-A}}$	0.5	0.35	0.55	0.2
$E_m^{\text{I-B}}$	0.5	0.65	0.45	0.8

region are energetically unfavorable. Therefore, interstitials jumps favor the avoidance of A-B bonds, which results in enhanced matrix atom transport to the sink. This phenomenon was not observed in Soisson’s work because they used a saddle-point energy model that gives a nonlocal activation energy (does not depend on the atomic environment of the jumping atom). Increasing the driving force for solute transport toward the sink (e.g., by setting $E_m^{\text{I-A}} = 0.6$, $E_m^{\text{I-B}} = 0.4$), the drop at the sink disappears. Snapshots for ABVI-1 and ABVI-4 at three different doses are shown in Fig. 2.7.

For the low solubility alloy, on the other hand, bulk precipitation does occur, as one would expect given the low marginal difference between bulk and sink segregation driving forces. As Fig. 2.6 shows, the solute spatial profiles are much more fluctuative than their high solubility counterparts, especially for the depletion case (ABVI-2 vs. ABVI-4). This of course

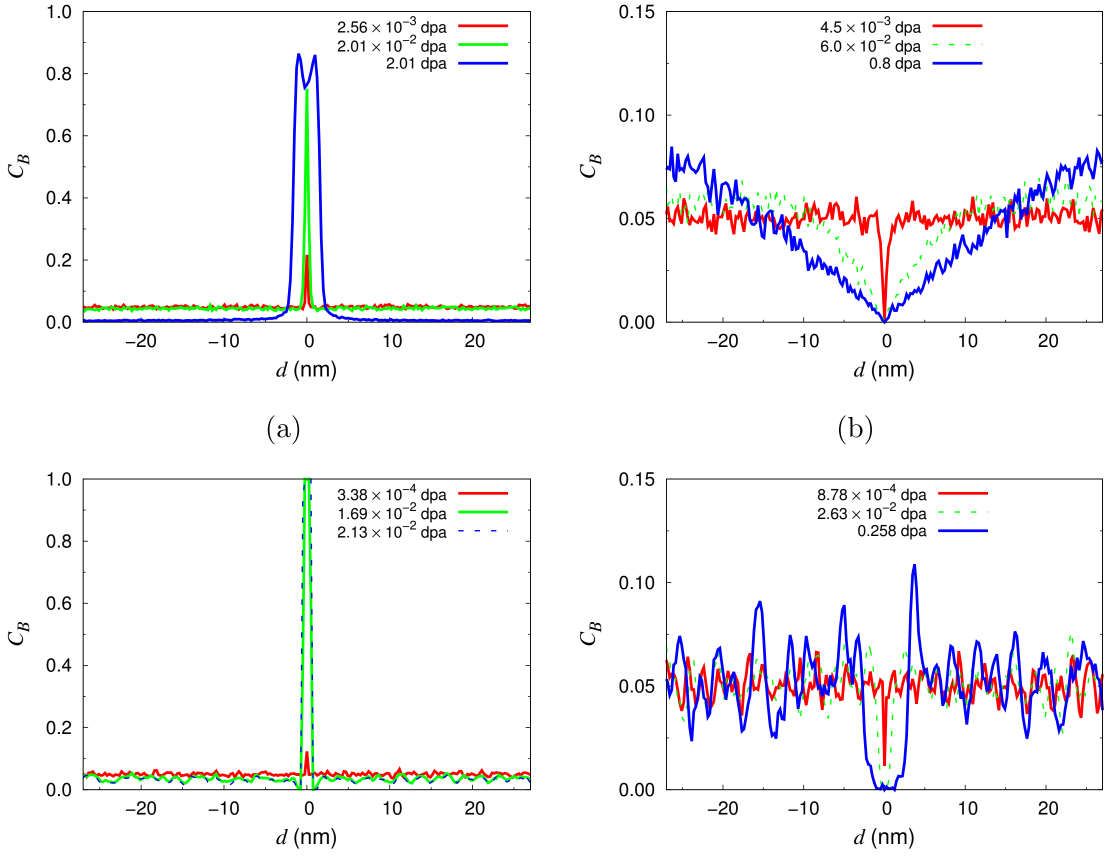

(a) (b)

(c) (d)

Figure 2.6: Spatial solute concentration profiles at different doses for the undersatured alloy for the (a) solute enrichment and (b) solute depletion cases at $T = 800$ K. The supersatured case for (c) solute enrichment and (d) solute depletion at $T = 500$ K are also shown. The nominal solute concentration of the alloy is $C_B = 0.05$ and the dose rate is 10^{-6} dpa·s^{-1}.

is a manifestation of the formation of precipitates in bulk. The mean free path for solute diffusion is quite low, due to a high number density of precipitates acting as trapping sites, which makes depletion dynamics slow. Soisson observed a less intense bulk precipitation than shown here, possibly also due to the different in activation energy models employed. In any case, the global qualitative features of the alloy evolution kinetics are matched by both methods.

These results show that the saddle point energies are crucial in establishing the relative

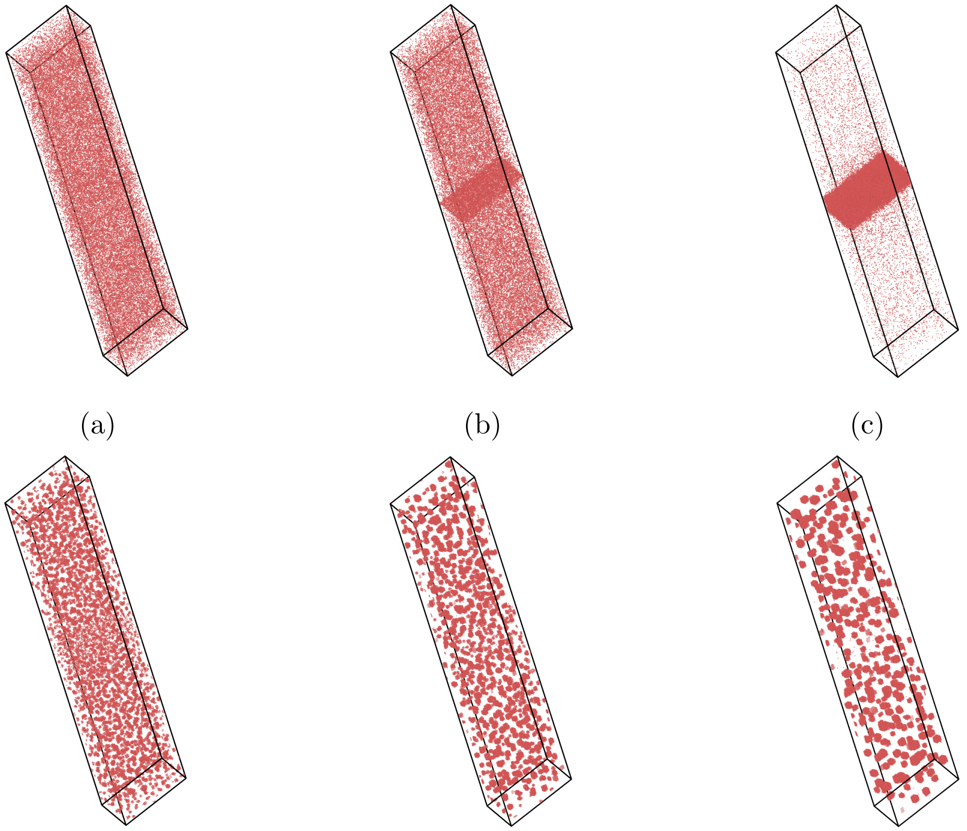

(a) (b) (c)

(d) (e) (f)

Figure 2.7: Snapshots of ABVI-1 system (undersaturated, enrichment) at (a) 2.56×10^{-3} (b) 2.01×10^{-2} and (c) 2.01 dpa. For the ABVI-4 case (supersaturated, depletion), configurations are shown at (d) 8.78×10^{-4} (e) 2.63×10^{-2} and (f) 0.258 dpa. Only solute atoms are shown.

solute fluxes to sinks. This is in agreement with Le Bouar and Soisson [BS02], who showed that the effect of (concentration dependent) saddle point energies on the kinetics can be felt dramatically at low temperatures, when atomic transport is slowed down.

2.2.4 ABVI system: Radiation-induced segregation at surfaces

The last verification example that we undertake in this paper is that of a finite system containing free surfaces. This mimics the case considered by Dubey and El-Azab, which studied a binary Au-Cu alloy under irradiation using a two-dimensional continuum reaction-diffusion model that included a free surface [DE15]. These authors used mean-field rate theory to solve the ordinary differential equation system representing defect kinetics with spatial resolution. As such, our method differs fundamentally in that it relies on a discrete lattice description, and so the comparison between both approaches must account for this distinction. Our lattice system, however, is constructed so as to create two free surfaces along one of the dimensions of the computational cell, with periodic boundary condition used in the other two. Adjacent to the free surfaces, several layers of 'vacuum' atoms are introduced (cf. Sec. 2.1.3.4 for the mechanisms involving these vacuum atoms). In this fashion, the surface is always univocally defined as the interface between atomic lattice sites and vacuum sites, which provides a convenient way to study the surface roughness as the simulation progresses. Atoms connected to the vacuum, regardless of their chemical nature, have bond energies in the direction along the surface normal equal to:

$$\varepsilon_s = a^2\gamma - \varepsilon_{\mathrm{A}A} \tag{2.40}$$

where a is the bond length (depends on surface orientation), γ is the surface energy, and $\varepsilon_{\mathrm{A}A}$ is a standard 'bulk' bond energy.

As well, considering free surfaces introduces both a defect sink and a defect source. In addition to Frenkel-pair generation by irradiation, point defects can also be emitted thermally from the surface. Following Dubey and El-Azab, Frenkel-pair generation rate is set at 1.0 dpa·s^{-1}. Regarding defect emission from the surface, the high formation energy difference between interstitial defects and vacancies allows us to discount thermal emission of SIAs, as done in ref. [DE15], while vacancies can be created at all surface sites. In each step, the rates of all the possible creation paths, *i.e.* all 1$^{\mathrm{st}}$-nn jumps from surface sites towards the interior of the box, are calculated and added to the global kMC event list. Vacancy emission can occur from any surface site. Given the potentially large number of such sites, we pre-compute all the thermal emission rates at the beginning, and then simply update the list when the local chemical environment around a surface site changes during the kMC simulation. The large majority of these emission events do not result in a successful vacancy injection into the bulk but, rather, just in an emission immediately followed by re-absorption at the surface. Considering these transitions (the so-called 'flickering' problem: not encountered in continuum mean field approaches) is exceedingly inefficient. To deal with the problem, especially at elevated temperature, one can apply the following method: calculate numerically the conditional probability that, if an emission event occurs, the emitted vacancy will make it to a depth where the surface attraction is no longer felt. In other words, the probability that an emission/re-absorption event is uncorrelated (diffusive) as opposed to correlated. This enhances the computational efficiency per kMC step significantly, yet providing a very accurate approximation to the 'brute force' method.

The annihilation of defects at surfaces is also considered, as described in Sec. 2.1.3.4. After Dubey and El-Azab, we study a face-centered cubic binary Au-10% at. Cu alloy using the energetics provided in Table 2.4 based on a study by Hashimoto et al. [HIS95]. The computational box dimensions are 660 × 270 × 4 primitive cells, with a vacuum buffer of 20 atomic layers on either side of the free surface, along the x-direction. In this case, jumps of mixed interstitials are calculated considering both directional possibilities, e.g. AB+A→B+AA, or AB+A→AB+A (cf. Table 2.1), with their total rate weighted by a factor of $1/2$ to preserve the correct sampling statistics.

The differences between kMC simulations and the continuum model are also exhibited in energy parameters. Dubey and El-Azab defined global parameters for their simulations such as defect formation energies, and surface energies. In kMC simulations, however, one need to express of all energies into bond energies. In this work, we set the vacuum energy level as the zero reference, *i*.e. $\epsilon_{v\text{-X}} = 0$ (where $X=$ A, B, V, v), and the energies of atoms on the surface are simply tallied in terms of the number of missing surface bonds. The defect bond energy parameters then can be obtained from formation energies of vacancy and interstitial using the formulas described in Section 2.1.3.3. The surface energy per area and defect formation energies are taken from Dubey and El-Azab's paper. In addition, after Hashimoto et al., a conversion energy is applied when interstitial defects change their type after a diffusive jump. On some occasions, the activation energy for interstitialcy jumps can become negative, which we simply interpret as a spontaneous event within the kMC cycle.

Table 2.4: The parameters for the Au-Cu ABVI system. 'A' are Cu atoms, 'B' are Au atoms. X, Y= A, B.

Bond energies (eV)				
$\epsilon_{\text{X-Y}}$	$\epsilon_{\text{V-X}}$	$\epsilon_{\text{AA-X}}$	$\epsilon_{\text{AB-X}}$	$\epsilon_{\text{BB-X}}$
-0.1425	-0.01625	0.24625	0.12875	0.14625
Migration energies (eV)				
$E_m^{\text{V-A}}$	$E_m^{\text{V-B}}$	$E_m^{\text{I-AA}}$	$E_m^{\text{I-AB}}$	$E_m^{\text{I-BB}}$
0.88	0.76	0.3	0.377	0.12
Conversion energies (eV)				
$E_c^{\text{AA}\to\text{AB}}$	$E_c^{\text{AB}\to\text{AA}}$	$E_c^{\text{BB}\to\text{AB}}$	$E_c^{\text{AB}\to BB}$	
0.3	0.5	0.12	0.32	

Our kMC simulations are run up to a maximum dose of 0.04 dpa. As in Section 2.2.2, we perform five independent runs to study the statistical variability and provide error bars to the simulation results. In this case, we take the average and statistical deviation at each point along the x-coordinate. The spatial solute concentration profiles at 650 K as a function of dose are shown in Fig. 2.8. For the five simulations performed, the statistical errors are on the order of 20%, approximately. From the figure, the enrichment of solute atoms near the surfaces can be clearly appreciated, which is accompanied by local depletion in the subsurface region. Segregation near the surfaces increases with dose, in agreement with Dubey and El-Azab's work. These authors also studied the degree of segregation as a function of time $M(t)$, defined as:

$$M(t) = \int_0^{l_s} \left(C(x,t) - \bar{C}\right) dx \tag{2.41}$$

where l_s is an arbitrary segregation distance, $C(x,t)$ is the instantaneous solute concentration profile, and $\bar{C}$ is the average solute concentration of the whole system. Here, we replace the integral by a discrete sum over lattice positions, with l_s defined as the distance from the surface at which the local concentration is within 10% of the background global concentration. To avoid noise due to lattice fluctuations, we apply a Savitzky-Golay smoothing filter [SG64] prior to the determination of l_s. M represents the deviation of the local concentration w.r.t. the average global concentration, integrated across the entire sample thickness. As such, an increasing value of M reflects a higher degree of heterogeneity in the solute distribution.

The evolution of M as a function of dose and temperature is shown in Fig. 2.9. Our results are in agreement with those of Dubey and El-Azab, with M increasing with dose monotonically in all cases. However, the evolution with temperature shows two distinct trends. First, M increases with temperature up to a critical value of approximately 650 K. Then, it gradually decreases until, at $T = 900$ K, the degree of segregation is practically zero. The causes behind this behavior are well understood [OR79]. Essentially, at low temperatures, vacancy mobility is limited, leading to high excess vacancy concentration and high recombination rates. As a consequence, segregation is low due to small defect fluxes to surfaces. At higher temperatures, vacancy and interstitial diffusion are activated resulting in net solute segregation. However, above 650 K, significant numbers of vacancies start to be emitted from the surfaces, leading to high back diffusion rates and again high recombination rates. The two effects result in a reduced solute segregation to the surfaces. Therefore, the maximum degree of segregation occurs at intermediate temperatures, consistent also with Dubey and El-Azab's findings.

KMC simulations are capable of providing morphological features that continuum methods cannot furnish. For example, our method can be used to study the evolution of the surface roughness, an example of which is shown in Fig. 2.10. The figure contains two snapshots of the surface for a system with a computational box size of of $660 \times 32 \times 32$ primitive cells at 500 K at different accumulated doses, where clear surface morphology changes can be appreciated. As well, surface roughness is accompanied by a concomitant increase in the

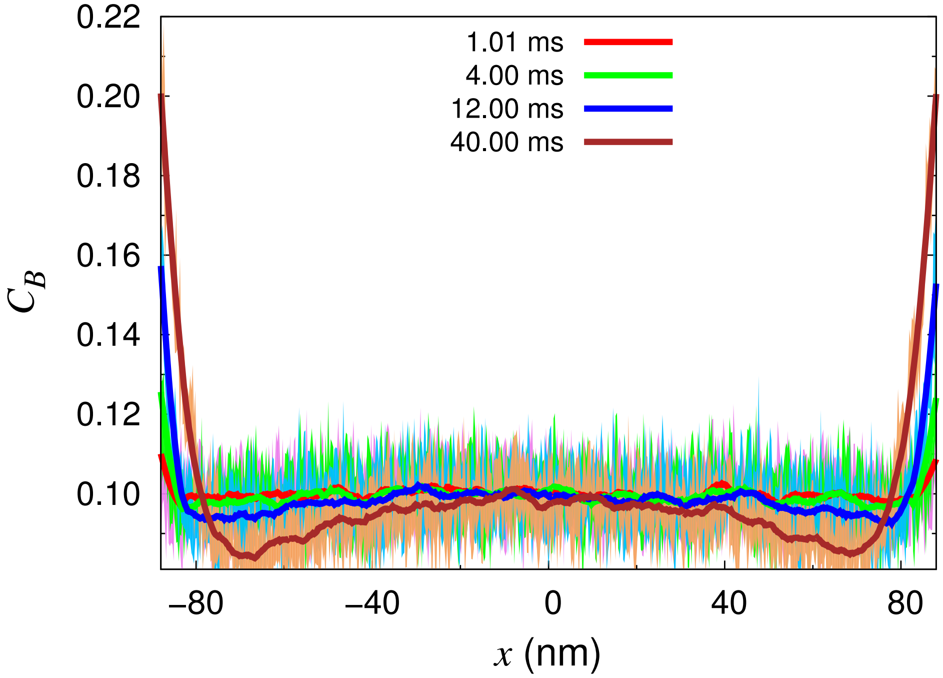

Figure 2.8: Solute concentration profile and associated error bars at different doses for the Au-10% at. Cu alloy at T= 650 K . The dose rate is 1.0 dpa·s^{-1}.

concentration of solute atoms, which occurs by the mechanisms explained above.

2.3 Summary and Conclusions

We have proposed an extension of the standard ABV Hamiltonian to discrete binary systems containing interstitial defects. The chosen framework for this extension is the Ising model, where three new values for the spin variables are considered: '+2', representing pure self-interstitials (A-A), '−2', representing pure solute interstitials (B-B), and '0', for mixed interstitials (A-B). The reason for choosing these values is to preserve one of the essential magnitudes of the Ising model, the magnetization $N^{-1}\sum_i \sigma_i$, or, in the ABVI context, the excess solute concentration. The main advantage behind expressing a cluster expansion Hamiltonian as an Ising Hamiltonian is that thermodynamic information about the system

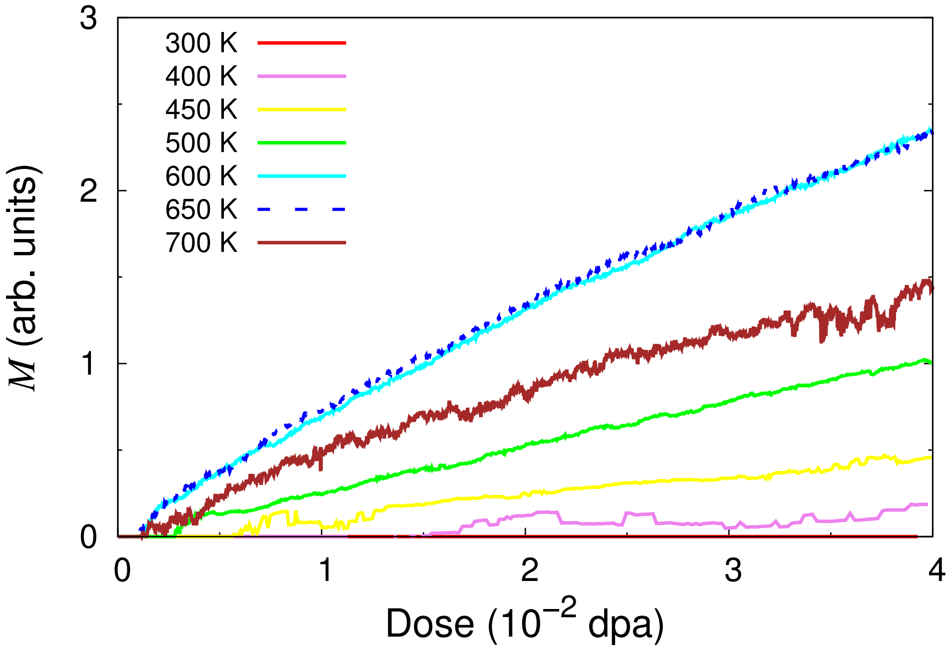

Figure 2.9: Evolution of the degree of segregation at different temperatures. The total solute concentration is 10% at. The dose rate is 1.0 dpa·s^{-1}.

can more easily be construed in the Ising framework. For example, the value of the constants of class 3 identified in eq. (2.27) uniquely determine the thermodynamic phase diagram of the ABVI model (much like constant J in eq. (2.2) determines the structure of the ABV system). Indeed, one of the aspects of greatest interest associated with the ABVI model is to study how the presence of interstitials alters the behavior of substitutional binary alloys.

However, we leave this thermodynamic analysis for a specific binary system with well characterized bond energetics for a future study, and, instead, in this paper we have focused on verification by comparing against a number of selected published studies. The main tests that we have conducted include discrete lattice ABV and ABVI for dilute Fe-Cu alloys, as well as comparison against a spatially-resolved mean-field study of solute segregation at free surfaces in irradiated Au-Cu alloys. In all cases, basic metrics related to the timescale and/or some governing kinetic parameters were reproduced with good agreement. In terms of computational cost, our Ising ABVI model scales in a similar manner as second-order cluster

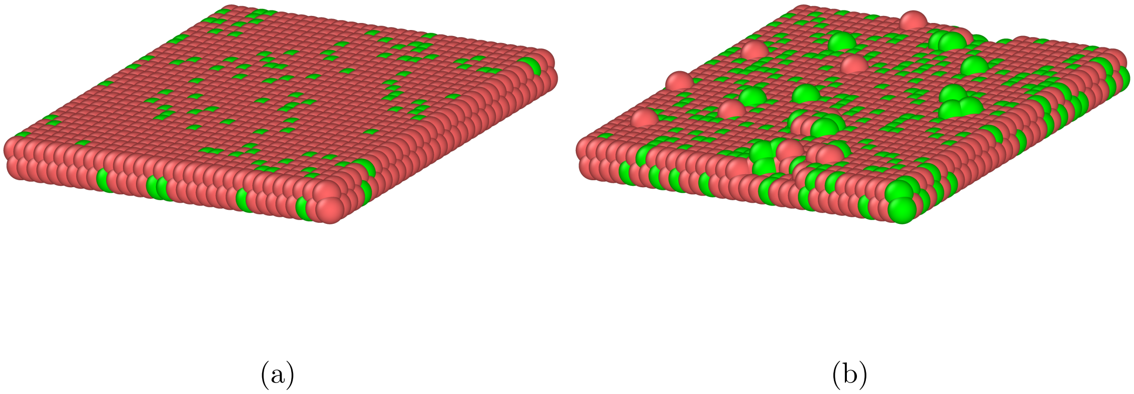
(a) (b)

Figure 2.10: Snapshots of surface roughness at (a) $t = 0$, and (b) $t = 0.02$ s for the Au-10.0 at. Cu system alloy for a computational box of $660 \times 32 \times 32$ primitive cells at 500 K. Red dots represent solvent (A) atoms, while solute atoms (B) are represented as green dots. The dose rate is 1.0 dpa$\cdot$s^{-1}.

expansion Hamiltonians with similar cutoff radius –as it should, given that no advantage is lost by simply recasting a cluster expansion Hamiltonian into the Ising form.

Thus, in conclusion, we present an ABVI Hamiltonian, cast as an Ising model Hamiltonian, for discrete event simulations that can be considered a generalization of ABV models. Our model has been verified against existing parameterizations of cluster expansion Hamiltonians using kinetic Monte Carlo simulations, with good agreement observed. The model will be used to study W-Re alloy evolution under irradiation, which will be discussed in the next chapter.

CHAPTER 3

Mechanism of Re precipitation in irradiated W-Re alloys from Monte Carlo simulations

In this chapter, we study the kinetics of Re precipitation in irradiated W accounting for both vacancy and interstitial transport. To this effect, we perform both Metropolis and kinetic MC simulations on alloy evolution parameterized solely using first principles calculations. The Metropolis MC simulation results provide a thermodynamic perspective on the W-Re alloy system, while kinetic MC simulations give kinetic effect from defect transports on the alloy. Previous DFT calculations have discovered an ”bridge” migration mechanism for mixed-dumbbell interstitial, which consists of a series of mixed dumbbell rotations and translations such that the mixed nature of the dumbbell is preserved and solutes can be transported over long distances without the need for vacancy exchanges [SYH14, SYH15, GME16]. Furthermore, this mechanism effectively transforms one-dimensional SIA diffusion into a 3D mixed-dumbbell transport process at activation energies considerably lower than that of vacancy diffusion. This mechanism has been suspected to have impact on RIP, and therefore was implemented the mechanism in our KMC model. The chapter start in Section 3.1 by describing the essential elements of our simulation models as well as the parameterization effort based on DFT calculations. In Section 3.2, our main results are provided, including semi-grand canonical Monte Carlo calculations of ternary W-Re-vacancy and W-Re-SIA systems, and kMC simulations and analysis of the Re-precipitate nucleation and growth. Finally, a discussion of the results and the conclusions are given in Section 3.3.

3.1 Theory and methods

3.1.1 Energy model

The energy model employed is a cluster expansion Hamiltonian based on pair interactions truncated to the 2^{nd}-nearest neighbor (2nn) shell, as the $ABVI$ model described in the previous chapter:

$$\mathcal{H} = \sum_{i} \sum_{\alpha,\beta} n^{(i)}_{\alpha\text{-}\beta} \epsilon^{(i)}_{\alpha\text{-}\beta} \tag{3.1}$$

where (i) specifies the type of nearest-neighbor interaction (first or second), α and β refer to a pair of lattice sites, separated by a distance specified by the index i, $n_{\alpha\text{-}\beta}$ denotes the number of occurrences (bonds) of each α-β pair, and $\epsilon_{\alpha\text{-}\beta}$ is bond energy. In the previous chapter, I have shown how this Hamiltonian can be reduced to a generalized Ising Hamiltonian involving solvent and solute atoms (A and B), vacancies (V), and pure and mixed interstitials (AA, BB, and AB) [HM16]. The Hamiltonian, As shown in Section 2.8, is then expressed as a sum of polynomial terms of various degrees involving spin variables σ_α and σ_β in the manner of the Ising model:

$$\mathcal{H} = \sum_{n,m} \sum_{\alpha,\beta} C_{nm} \sigma^{n}_{\alpha} \sigma^{m}_{\beta} \tag{3.2}$$

where n and m are exponents reflecting the order of each term, and C_{nm} are a coupling constants shown in Section 2.1.2.2. In the chapter, the notations of atoms and point defects are as the same as in previous chapter, with A: W atoms; B: Re atoms; V: vacancies, AA: W-W dumbbell (or self-interstitial atom); BB: Re-Re dumbbell; AB: mixed W-Re dumbbell.

3.1.2 Semi-Grand Canonical Monte Carlo for AB systems

The thermodynamic phase diagram of the W-Re system can be studied using semi-grand canonical Monte Carlo (SGMC) calculations as a function of temperature and solute concentration [BLP81, DL93, PSM99, TLA04, CL05, BZK10]. We seek to minimize the thermodynamic potential of the semi-grand canonical ensemble, characterized by a constant temperature T, a constant number of particles N, and a constant chemical potential μ [1]. In each SGMC step, a transition involving an atom selected at random is executed and the new state is accepted with a probability:

$$p_{ij} = \exp\left(-\frac{\Delta\mathcal{H}_{ij} - N_{\mathrm{B}}\Delta\mu}{k_B T}\right) \tag{3.3}$$

where $\Delta\mathcal{H}_{ij}$ is the energy difference between the initial and final states, i and j, $N_{\mathrm{B}} = NX$ is the number of solute atoms (X: solute concentration), $\Delta\mu$ is the change in chemical potential per atom after the transition, and k_B is Boltzmann's constant. In this work, each transition is defined by changing the chemical nature of one atom chosen at random (A→B or B→A). In terms of the change in spin variable (in the notation of the generalized Ising Hamiltonian, cf. eq. (3.2)), this always results in a change of $\delta\sigma = \pm 2$, such that eq. (3.3) can be simplified to:

$$p_{ij} = \exp\left(-\frac{\Delta\mathcal{H}_{ij} \pm 2\Delta\mu}{k_B T}\right) \tag{3.4}$$

In the calculations, the chemical potential difference $\Delta\mu$ and the temperature T are input variables, while the solute composition X and the equilibrium configurations are obtained when convergence is reached.

3.1.3 Metropolis Monte Carlo calculations of ABV system configurations

During irradiation, the introduction of large amounts of defects has the potential to impact the thermodynamics of the system. It is therefore of interest to calculate phase diagrams with fixed defect concentrations using equilibrium (Metropolis) Monte Carlo. Defect concentrations are not thermodynamically equilibrated under irradiation –the number of vacancies

---

[1] For a brief discussion on the differences between the semi-grand canonical and the grand canonical ensembles, see ref. [sgm].

or interstitials is not controlled by the chemical potential–, and so the AB system must be considered in conjunction with a fixed defect concentration. Take the case of vacancies for example, to properly obtain converged nonequilibrium configurations of ABV systems, we employ a *flip* and *swap* approach: (i) initially a system consisting of A atoms and a random distribution of vacancies is considered; (ii) a lattice point is selected at random; (iii) if that lattice point corresponds to an atom, a SGMC step is carried out, resulting in a change in the relative concentrations of A and B; if it, on the contrary, corresponds to a vacant site, then a canonical Monte Carlo step is carried out, leaving X unchanged, and the vacancy exchanges its position with a randomly-selected atom. This trial swap is then accepted according to the Boltzmann distribution:

$$p_{ij} = \exp\left(-\frac{\Delta\mathcal{H}_{ij}}{k_B T}\right) \tag{3.5}$$

In this fashion, equilibrated AB alloys containing a fixed vacancy concentration are obtained, from which one can determine the changes relative to the thermodynamic equilibrium configurations. Although interstitials are much higher in energy than vacancies (so that only very small concentrations need be explored), the procedure for the ABI system is identical to that of the ABV system.

3.1.4 Kinetic Monte Carlo simulations of ABVI systems

The kinetic evolution of W-Re alloys under irradiation is studied using standard lattice kMC. The system is evolved by events involving atomic jumps and time is advanced according to the residence-time algorithm [YE66]. Jump rates are calculated as:

$$r_{ij} = \nu \exp\left(-\frac{\Delta E_{ij}}{k_B T}\right) \tag{3.6}$$

where ν is an attempt frequency and ΔE_{ij} is the activation energy to jump from state i to state j.

3.1.4.1 Vacancy migration model

A review on models proposed to describe the activation energy based on different interpretations of the atomic migration process has been given in Chapter 2.3 (see also [HM16] and [SBC10] for recent reviews). In this work, the activation energy of vacancy jump is calculated by the saddle-point energy model (or cut-bond model) [SBM96, SF07, MSF12, SSM16], according to which ΔE_{ij} is given by the energy difference of the configuration when the jumping atom is at saddle point and the initial configuration:

$$\Delta E_{ij} = \sum_{p} \epsilon^{sp}_{\alpha\text{-}p} - \sum_{q} \epsilon^{(i)}_{\alpha\text{-}q} - \sum_{r \neq \alpha} \epsilon^{(i)}_{\text{V-}r} + \sum \Delta E^{\text{non-broken}}_{ij} \tag{3.7}$$

where α is the jumping atom, V is the vacancy, and ϵ^{sp} are the bond energies between the atom at the saddle point and the neighboring atoms. The first term on the r.h.s. of eq. (3.7) reflects the energy of the jumping atom at the saddle point. In this work, we consider interactions up to 2nn distances for this term[2]. The second and third terms on the r.h.s. of the equation are the energies of the jumping atom and the vacancy at the initial state i. Finally, the fourth term gives the energy difference between state i and j for the non-broken bonds due to local solute concentration changes. The dependence of bond coefficients on local solute concentration will be discussed in Section 3.1.5.

3.1.4.2 Interstitial defect migration model

Here we consider self-interstitial atoms of the AA type, and mixed-interstitials AB. Due to their rarity, BB interstitials are omitted in our calculations. In bcc metals, AA SIAs are known to migrate athermally in one dimension along ⟨111⟩ directions with migration energy E_m, with sporadic rotations to other ⟨111⟩ orientations characterized by an activation energy E_r. These processes, however, are treated separately in the kMC simulations. In contrast

---

[2] In the saddle-point configuration for vacancy migration, there are six 1nn bonds and six 2nn bonds, compared with eight and six for a lattice point configuration.

to vacancy migration, activation energies of interstitial jumps are calculated using the direct final-initial system energy model [DMD07, VBD08, VBP08, RMO11]:

$$\Delta E_{ij} = \begin{cases} E_m + \Delta\mathcal{H}_{ij}, & \text{if } \Delta\mathcal{H}_{ij} > 0 \\ E_m, & \text{if } \Delta\mathcal{H}_{ij} < 0 \end{cases} \tag{3.8}$$

In addition, we include a bias due to the well-known phenomenon of *correlation*, by which a forward jump is slightly more likely to occur than a backward jump. This is reflected in a correlation factor f computed as the ratio of forward to backward jumps [ZLH13], which in our simulations is temperature dependent.

For their part, as pointed out in Chapter 1, recent DFT studies have revealed a new migration mechanism for mixed dumbbells in W alloys. This mechanism involves an non-dissociative sequence of rotations and translations such that the solute atom is always part of the mixed dumbbell (in contrast with the *intersticialcy* or 'knock-on' mechanism commonly associated with SIAs) [SYH14,SYH15,GE15,GME16]. This effectively makes AB interstitials move in three dimensions with 2nn jumps along $\langle 100\rangle$ directions. Calculations for the W-Re system have shown that the migration energy in this case is very low, on the order of one tenth of an eV. As we shall see, this plays a big role in governing the kinetic evolution of irradiated W-Re alloys.

3.1.4.3 Spontaneous events: recombination and absorption

Any recombination event occurs spontaneously (no sampling involved) when the distance between an interstitial defect and a vacancy is within the 3$^{\text{rd}}$ nearest neighbor distance. Another reaction considered to be instantaneous is the transition of a SIA into an AB dumbbell when it encounters a solute atom: AA+B→AB+A. This is because the binding energy between a SIA and a Re solute atom has been calculated to be -0.8 eV (negative binding energies represent attraction). The distance for this transformation is set to be equal to the 1nn separation.

Defect absorption represents another type of spontaneous event. Absorption can occur at sinks, such as a plane located in a stationary position within the simulation box [Soi06], or a free surface [HM16]. Sinks can potentially act also as defect emitters, as in the case of grain boundaries, dislocations, and free surfaces in real microstructures. Details about the implementation of these processes can be found in ref. [HM16].

3.1.4.4 Frenkel pair generation

In this work, defects are generated as Frenkel pairs at a prescribed rate set by the damage rate. To insert a defect pair, two atomic sites are chosen at random, one is replaced by a vacancy and the other with an interstitial formed by an A atom and the lattice atom.

3.1.5 Parameters

There are five distinct atomic species used in this work: W atoms (A), Re atoms (B), vacancies (V), SIAs (AA), and mixed-interstitials (AB). As mentioned above, our energy model consists of pairwise interactions up to the 2nn shell. After discounting interstitial-vacancy bonds, this amounts to 26 different types of bonds (13 for each nearest neighbor shell), all of which must be obtained using first-principles calculations. Moreover, as discussed by Martinez *et al.* [MSF12] and Senninger *et al.* [SSM16], several of these bond energies are sensitive to the local solute concentration and must be computed on the fly in each Monte Carlo step. Following Warczok *et al.* [WZK12], we reduce the number of unknowns from 26 to 13 by partitioning bond energies according the following relation:

$$\epsilon^{(2)} = \epsilon^{(1)} \left(\frac{r_{2\text{nn}}}{r_{1\text{nn}}}\right)^{-6} \tag{3.9}$$

which is used unless both bond energies can be explicitly calculated. For the bcc lattice, this results in $\epsilon^{(1)}_{\alpha\text{-}\beta}/\epsilon^{(2)}_{\alpha\text{-}\beta} = 0.421875$ for regular bond coefficients, and $\epsilon^{sp(1)}_{\alpha\text{-}\beta}/\epsilon^{sp(2)}_{\alpha\text{-}\beta} = 0.194052$ for saddle-point bond coefficients.

The local solute concentration is always computed up to the 2nn shell. Next we describe the parameterization procedure for each set of bond energies.

3.1.5.1 W-Re parameters

The W-Re bond coefficients are $\epsilon_{\text{A-A}}$, $\epsilon_{\text{B-B}}$, and $\epsilon_{\text{A-B}}$. They determine the thermodynamic equilibrium phase diagram of the alloy. $\epsilon_{\text{A-A}}$ and $\epsilon_{\text{B-B}}$ are obtained from the cohesive energies:

$$\begin{aligned} E^{\text{A}}_{coh} &= -\frac{z_1}{2}\epsilon^{(1)}_{\text{A-A}} - \frac{z_2}{2}\epsilon^{(2)}_{\text{A-A}} \\ E^{\text{B}}_{coh} &= -\frac{z_1}{2}\epsilon^{(1)}_{\text{B-B}} - \frac{z_2}{2}\epsilon^{(2)}_{\text{B-B}} \end{aligned} \tag{3.10}$$

where z_1 and z_2 are coordination numbers for the 1nn and 2nn shells, respectively. The cohesive energies calculated using DFT are given in Table 3.1. [3]

The coefficient for the A-B bond is obtained from the enthalpy of mixing of W-Re, ΔH^{mix}, which can be written within the Bragg-Williams approximation [BW34, BW35, Wil35] as:

$$\begin{aligned} \Delta H^{\text{mix}} = &\frac{z_1}{2}\left[(1-X)\epsilon^{(1)}_{\text{A-A}} + X\epsilon^{(1)}_{\text{B-B}} + 2x(1-x)\Omega^{(1)}_s\right] \\ &+ \frac{z_2}{2}\left[(1-X)\epsilon^{(2)}_{\text{A-A}} + X\epsilon^{(2)}_{\text{B-B}} + 2X(1-X)\Omega^{(2)}_s\right] \end{aligned} \tag{3.11}$$

where X is the global solute concentration, and Ω_s is the *heat of solution*, defined as:

$$\Omega^{(1)}_s = \epsilon^{(1)}_{\text{A-B}} - \frac{1}{2}\left(\epsilon^{(1)}_{\text{A-A}} + \epsilon^{(1)}_{\text{B-B}}\right) \tag{3.12}$$

$$\Omega^{(2)}_s = \epsilon^{(2)}_{\text{A-B}} - \frac{1}{2}\left(\epsilon^{(2)}_{\text{A-A}} + \epsilon^{(2)}_{\text{B-B}}\right) \tag{3.13}$$

---

[3] With xc-energy correction from Ref. [KIM11]

Table 3.1: Energetics of W-Re systems calculated with DFT.

Quantity	Value	Source
E^{A}_{coh}	8.3276	This work
E^{B}_{coh}	7.4070	This work
ΔH^{mix}	$-0.1571 - 0.2311X$	Ref. [GME16]
E^{V}_{f}	3.1690	This work
$E^{(a)}_{b}$	-0.2096	This work
$E^{(b)}_{b}$	-0.1520	This work
$E^{(c)}_{b}$	-0.3079	This work
$E^{(d)}_{b}$	-0.2992	This work
$E^{\mathrm{V\text{-}V}}_{b,\mathrm{1nn}}$	-0.0146	This work(3)
$E^{\mathrm{V\text{-}V}}_{b,\mathrm{2nn}}$	0.3028	This work(3)
E^{AA}_{f}	10.16	Ref. [GE15]
E^{AB}_{f}	9.49	Ref. [GE15]
$E^{\mathrm{AA\text{-}B}}_{b,\mathrm{1nn}}$	-0.52	Ref. [GE15]
$E^{\mathrm{AB\text{-}B}}_{b,\mathrm{1nn}}$	-0.53	Ref. [SNK16]
$E^{\mathrm{AA\text{-}AA}}_{b,\mathrm{1nn}}$	-2.12	Ref. [BDS10]
$E^{\mathrm{AA\text{-}AB}}_{b,\mathrm{1nn}}$	-2.12	Assumed (4)
$E^{\mathrm{AB\text{-}AB}}_{b,\mathrm{1nn}}$	-3.2	Ref. [GME16]
$E^{\mathrm{V}\to\mathrm{A}}_{m}$ (A)	1.623	This work
$E^{\mathrm{V}\to\mathrm{B}}_{m}$ (A)	1.651	This work
$E^{\mathrm{V}\to\mathrm{A(1)}}_{m}$ (Fig. 3.2(c))	1.7151	This work
$E^{\mathrm{V}\to\mathrm{A(2)}}_{m}$ (Fig. 3.2(c))	1.6378	This work
$E^{\mathrm{V}\to\mathrm{B(3)}}_{m}$ (Fig. 3.2(c))	1.577	This work
$E^{\mathrm{V}\to\mathrm{A}}_{m}$ (V)	1.623	This work
$E^{\mathrm{V}\to\mathrm{B}}_{m}$ (V)	1.651	This work

Combining eqs. (3.10) and (3.11), ΔE^{mix} can be expressed as:

$$X(1-X)\Omega_s^* = \Delta H^{\text{mix}} + (1-X)E_{coh}^{\text{A}} + XE_{coh}^{\text{B}} \tag{3.14}$$

where $\Omega_s^* = z_1\Omega_s^{(1)} + z_2\Omega_s^{(2)}$. To obtain the dependence of the heat of solution on the solute concentration, we fit the l.h.s. of eq. (3.14) to the data points for the mixing enthalpies as a function of X calculated in our previous work [GME16]. The best fit, shown in Figure 3.1, is achieved when Ω_s^* is expressed a linear function of the concentration:

$$\Omega_s^* = w_0 + w_1 X$$

with $w_0 = -0.1571$ and $w_1 = -0.2311$. The negative values of w_0 and w_1 suggest a strong tendency towards ordering, which becomes larger as the solute concentration increases. Combining eqs. (3.9), (3.10), (3.12), and (3.14), one can obtain the values of $\Omega_s^{(1)}$, $\Omega_s^{(2)}$, $\epsilon_{\text{A-B}}^{(1)}$, and $\epsilon_{\text{A-B}}^{(2)}$. A non-constant Ω_s^* effectively implies that $\epsilon_{\text{A-B}}$ is also a function of the concentration. Moreover, to reflect local composition variations in the W-Re alloys, we make the assumption that the dependence of $\epsilon_{\text{A-B}}^{(1)}$ and $\epsilon_{\text{A-B}}^{(2)}$ on X can be transferred to the local environment of each atom, such that both bond energy coefficients are functions of the local composition, which we term x, and must be computed on the fly for each solute atom in the system.

3.1.5.2 Vacancy parameters

The vacancy bond coefficients are $\epsilon_{\text{A-V}}$, $\epsilon_{\text{B-V}}$, and $\epsilon_{\text{V-V}}$. $\epsilon_{\text{A-V}}$ can be readily obtained from the value of the vacancy formation energy:

$$E_f^{\text{V}} = E_{coh}^{\text{A}} - z_1\epsilon_{\text{A-V}}^{(1)} - z_2\epsilon_{\text{A-V}}^{(2)} \tag{3.15}$$

where E_f^{V} is the vacancy formation energy in pure W (given in Table 3.1). $\epsilon_{\text{B-V}}$ can be obtained from the binding energies of V-Re configurations, which for a structure involving m solute atoms and n vacancies is defined as:

$$E_b^{\text{B}_m\text{V}_n} = E_f^{\text{B}_m\text{V}_n} - mE_f^{\text{B}} - nE_f^{\text{V}} \tag{3.16}$$

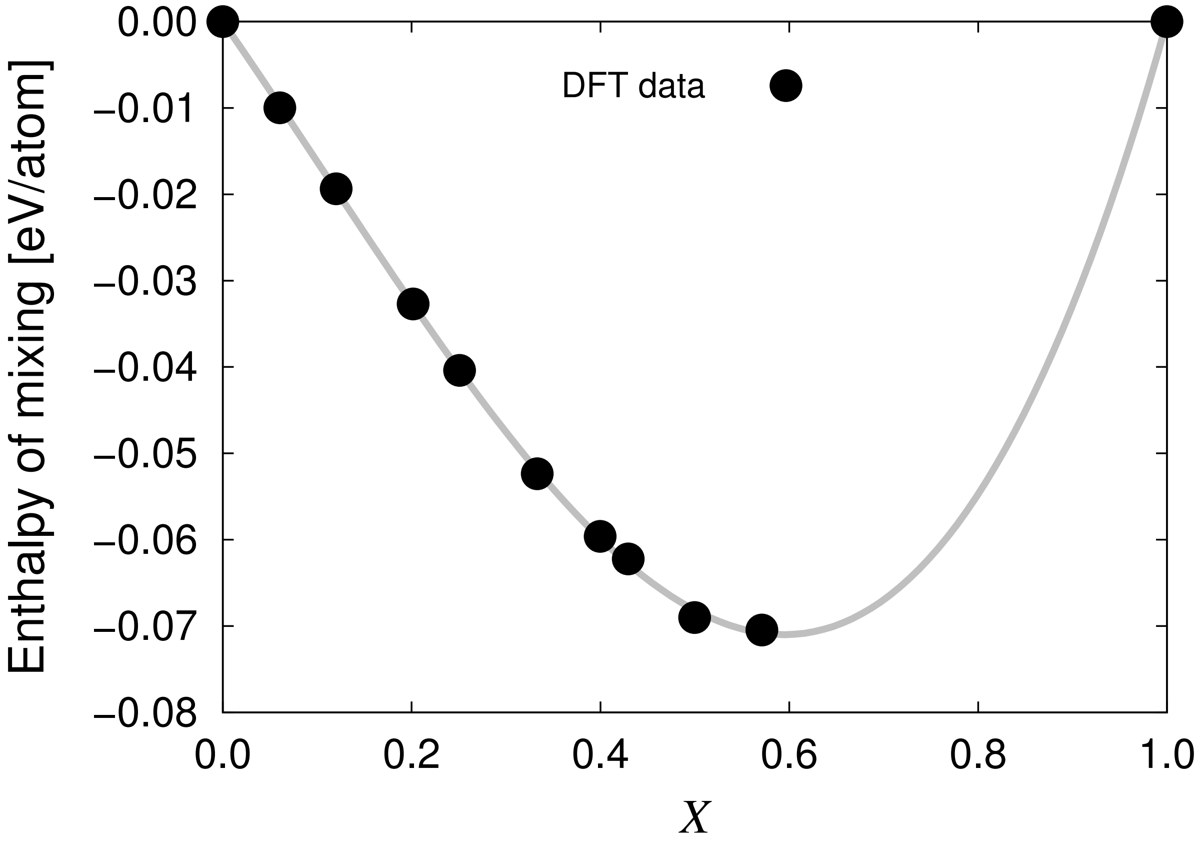

Figure 3.1: Enthalpy of mixing as a function of solute concentration from ref. [GME16] and 3rd-degree polynomial fit.

where the E_f are the respective formation energies of each structure. In this work, binding energies for the four vacancy-solute configurations shown in Figure 3.2 have been calculated (cf. Table 3.1). One can now rewrite eq. (3.16) as a function of the B-V bond coefficients $\epsilon^{(1)}_{\text{B-V}}$ and $\epsilon^{(2)}_{\text{B-V}}$ for each one of the configurations in the figure:

$$E_b^{(a)} = \epsilon^{(1)}_{\text{B-V}} + \epsilon^{(1)}_{\text{A-A}} - \epsilon^{(1)}_{\text{A-B}} - \epsilon^{(1)}_{\text{A-V}} \tag{3.17a}$$

$$E_b^{(b)} = \epsilon^{(2)}_{\text{B-V}} + \epsilon^{(2)}_{\text{A-A}} - \epsilon^{(2)}_{\text{A-B}} - \epsilon^{(2)}_{\text{A-V}} \tag{3.17b}$$

$$\begin{aligned} E_b^{(c)} =& 2\epsilon^{(1)}_{\text{B-V}} + \epsilon^{(2)}_{\text{B-B}} + 2\epsilon^{(1)}_{\text{A-A}} + \epsilon^{(2)}_{\text{A-A}} - 2\epsilon^{(1)}_{\text{A-V}} - 2\epsilon^{(1)}_{\text{A-B}} \\ &- 2\epsilon^{(2)}_{\text{A-B}} + 14\Delta\epsilon^{(1)}_{\text{A-B}} + 10\Delta\epsilon^{(2)}_{\text{A-B}} \end{aligned} \tag{3.17c}$$

$$E_b^{(d)} = 2\epsilon^{(2)}_{\text{B-V}} + 2\epsilon^{(2)}_{\text{A-A}} - 2\epsilon^{(2)}_{\text{A-B}} - 2\epsilon^{(2)}_{\text{A-V}} \tag{3.17d}$$

where $\Delta\epsilon^{(m)}_{\text{A-B}}$ is the change in $\epsilon^{(m)}_{\text{A-B}}$ due to the local solute concentration change resulting from the vacancy jump.

To define the dependence on x of $\epsilon^{(1)}_{\text{B-V}}$, we must consider two factors. First, our DFT calculations show that $\epsilon^{(1)}_{\text{A-V}} > \epsilon^{(1)}_{\text{B-V}}$. Second, the values of $\epsilon^{(1)}_{\text{B-V}}$ is seen to increase with local concentration. Both of these conditions are satisfied by assuming a dependence such as $\epsilon^{(1)}_{\text{B-V}}(x) = \epsilon^{(1)}_{\text{A-V}} - ax^{-1}$, where a is a fitting constant. As well, $\epsilon^{(2)}_{\text{B-V}}$ is seen to independently increase with concentration, such that $\epsilon^{(2)}_{\text{B-V}}(x) = bx + c$, where b and c are fitting parameters

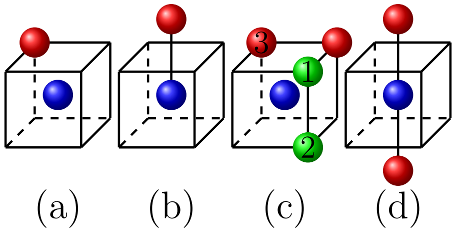

Figure 3.2: Configurations of V-Re clusters used to extract bond energy coefficients $\epsilon_{\text{A-V}}$ and $\epsilon_{\text{B-V}}$. Blue spheres represent vacancies, red spheres represents Re atoms. All other lattice sites are occupied by A atoms, which are omitted for clarity. Green spheres indicate the various equivalent sites for atoms to exchange positions with the vacancy

$\epsilon_{\text{V-V}}$ can be readily calculated by considering the binding energy of a di-vacancy:

$$E^{\text{V-V}}_{b,\text{1nn}} = \epsilon^{(1)}_{\text{A-A}} + \epsilon^{(1)}_{\text{V-V}} - 2\epsilon^{(1)}_{\text{A-V}} \tag{3.18}$$

$$E^{\text{V-V}}_{b,\text{2nn}} = \epsilon^{(2)}_{\text{A-A}} + \epsilon^{(2)}_{\text{V-V}} - 2\epsilon^{(2)}_{\text{A-V}} \tag{3.19}$$

It is interesting to note that, in accordance with several other studies [BD07, VWF12, MNK11, OIT14, SNK16], $E^{\text{V-V}}_{b,\text{2nn}}$ takes a positive value (cf. Table 3.1), indicating repulsion between vacancies that are at 2nn distances of each other.

3.1.5.3 Interstitial defect parameters

The interstitial bond coefficients include $\epsilon_{\text{AA-A}}$, $\epsilon_{\text{AB-A}}$, $\epsilon_{\text{AA-B}}$, $\epsilon_{\text{AB-B}}$, $\epsilon_{\text{AA-AA}}$, $\epsilon_{\text{AA-AB}}$, and $\epsilon_{\text{AB-AB}}$. $\epsilon_{\text{AA-A}}$ and $\epsilon_{\text{AB-A}}$ are calculated directly from the formation energies of SIAs and mixed dumbbells:

$$E_f^{\text{AA}} = -4\epsilon^{(1)}_{\text{A-A}} - 3\epsilon^{(2)}_{\text{A-A}} + 8\epsilon^{(1)}_{\text{AA-A}} + 6\epsilon^{(2)}_{\text{AA-A}} \tag{3.20}$$

$$E_f^{\text{AB}} = -4\epsilon^{(1)}_{\text{A-A}} - 3\epsilon^{(2)}_{\text{A-A}} + 8\epsilon^{(1)}_{\text{AB-A}} + 6\epsilon^{(2)}_{\text{AB-A}} \tag{3.21}$$

The other bond coefficients are obtained from various binding energies:

$$E_{b,\text{1nn}}^{\text{AA-B}} = \epsilon^{(1)}_{\text{AA-B}} + \epsilon^{(1)}_{\text{A-A}} - \epsilon^{(1)}_{\text{AA-A}} - \epsilon^{(1)}_{\text{A-B}} \tag{3.22}$$

$$E_{b,\text{1nn}}^{\text{AB-B}} = \epsilon^{(1)}_{\text{AB-B}} + \epsilon^{(1)}_{\text{A-A}} - \epsilon^{(1)}_{\text{AB-A}} - \epsilon^{(1)}_{\text{A-B}} \tag{3.23}$$

$$E_{b,\text{1nn}}^{\text{AA-AA}} = \epsilon^{(1)}_{\text{AA-AA}} + \epsilon^{(1)}_{\text{A-A}} - 2\epsilon^{(1)}_{\text{AA-A}} \tag{3.24}$$

$$E_{b,\text{1nn}}^{\text{AA-AB}} = \epsilon^{(1)}_{\text{AA-AB}} + \epsilon^{(1)}_{\text{A-A}} - \epsilon^{(1)}_{\text{AA-A}} - \epsilon^{(1)}_{\text{AB-A}} \tag{3.25}$$

$$E_{b,\text{1nn}}^{\text{AB-AB}} = \epsilon^{(1)}_{\text{AB-AB}} + \epsilon^{(1)}_{\text{A-A}} - 2\epsilon^{(1)}_{\text{AB-A}} \tag{3.26}$$

These formation and binding energies are all taken from the literature[4].

All the bond energy coefficients, the equation used for their calculation, and the source of the numbers are compiled in Table 3.2.

3.1.5.4 Migration parameters

The attempt frequency (ν in eq. (3.6)) used for vacancy jumps in this work is set to be equal to Debye frequency of W, or 6.5×10^{12} Hz [GDD08], while for interstitials we use a value of 1.5×10^{12} Hz [ZLH13].

---

[4] The only exception being the binding energy between an AA and an AB interstitial, which is assumed to be equal to the binding energy between two AA.

Table 3.2: Bond energy coefficients with the equation used for their calculation, and the literature source. x is the local solute concentration

$\epsilon^{(1)}_{\text{A-A}}$	-1.5815	cohesive energy, eq. (3.9)	This work
$\epsilon^{(2)}_{\text{A-A}}$	-0.6672	cohesive energy, eq. (3.9)	This work
$\epsilon^{(1)}_{\text{B-B}}$	-1.4067	cohesive energy, eq. (3.9)	This work
$\epsilon^{(2)}_{\text{B-B}}$	-0.5935	cohesive energy, eq. (3.9)	This work
$\epsilon^{(1)}_{\text{A-B}}$	$-1.5090 - 0.0219x$	mixing energy	Ref. [GME16]
$\epsilon^{(2)}_{\text{A-B}}$	$-0.6366 - 0.0092x$	eq. (3.9)	Ref. [GME16]
$\epsilon^{(1)}_{\text{A-V}}$	-0.4898	formation energy, eq. (3.9)	This work
$\epsilon^{(2)}_{\text{A-V}}$	-0.2067	formation energy, eq. (3.9)	This work
$\epsilon^{(1)}_{\text{B-V}}$	$-0.4898 - 0.009432/x$	formation e fitted to $\epsilon^{(1)}_{B-V} = a + \frac{b}{x}$	This work
$\epsilon^{(2)}_{\text{B-V}}$	$-0.3311 + 0.036x$	formation e fitted to $\epsilon^{(1)}_{B-V} = a + bx$	This work
$\epsilon^{(1)}_{\text{V-V}}$	0.5873	1nn binding energy	This work
$\epsilon^{(2)}_{\text{V-V}}$	0.5566	2nn binding energy	This work
$\epsilon^{(1)}_{\text{AA-A}}$	0.1740	formation energy, eq. (3.9)	Ref. [GE15]
$\epsilon^{(2)}_{\text{AA-A}}$	0.0734	formation energy, eq. (3.9)	Ref. [GE15]
$\epsilon^{(1)}_{\text{AB-A}}$	0.1104	formation energy, eq. (3.9)	Ref. [GE15]
$\epsilon^{(2)}_{\text{AB-A}}$	0.0466	formation energy, eq. (3.9)	Ref. [GE15]
$\epsilon^{(1)}_{\text{AA-B}}$	-0.2750	binding energy	Ref. [GE15]
$\epsilon^{(2)}_{\text{AA-B}}$	-0.1160	eq. (3.9)	Ref. [GE15]
$\epsilon^{(1)}_{\text{AB-B}}$	-0.3486	binding energy	Ref. [SNK16]
$\epsilon^{(2)}_{\text{AB-B}}$	-0.1470	eq. (3.9)	Ref. [SNK16]
$\epsilon^{(1)}_{\text{AA-AA}}$	-0.1905	binding energy	Ref. [BDS10]
$\epsilon^{(2)}_{\text{AA-AA}}$	-0.0804	eq. (3.9)	Ref. [BDS10]
$\epsilon^{(1)}_{\text{AA-AB}}$	-0.2505	binding energy	Assumed (4)
$\epsilon^{(2)}_{\text{AA-AB}}$	-0.1057	eq. (3.9)	Assumed (4)
$\epsilon^{(1)}_{\text{AB-AB}}$	-1.3977	binding energy	Ref. [GME16]
$\epsilon^{(2)}_{\text{AB-AB}}$	-0.5897	eq. (3.9)	Ref. [GME16]

From eq. (3.7), there are six different saddle-point bond coefficients: $\epsilon_{\text{A-A}}^{sp(m)}$, $\epsilon_{\text{A-B}}^{sp(m)}$, $\epsilon_{\text{A-V}}^{sp(m)}$, $\epsilon_{\text{B-A}}^{sp(m)}$, $\epsilon_{\text{B-B}}^{sp(m)}$, and $\epsilon_{\text{B-V}}^{sp(m)}$, where $m=$ 1nn, 2nn. In this notation, $\epsilon_{\alpha\text{-}\beta}^{sp(m)}$ represents the energy of the bond between the atom at the saddle point α and its closest lattice neighbor β. This means $\epsilon_{\alpha\text{-}\beta}^{sp(m)} \neq \epsilon_{\beta\text{-}\alpha}^{sp(m)}$.

The saddle-point bond coefficients connected to a lattice atom A (W atom), $\epsilon_{\alpha\text{-A}}^{sp(m)}$, can be calculated as:

$$z_1^{sp}\epsilon_{\alpha\text{-A}}^{sp(1)} + z_2^{sp}\epsilon_{\alpha\text{-A}}^{sp(2)} = E_m + \sum_{n,q}\epsilon_{X\text{-}q}^{(n)} + \sum_{n,r\neq X}\epsilon_{V\text{-}r}^{(n)} \tag{3.27}$$

where z_1^{sp} and z_2^{sp} are the numbers of 1st- and 2nd nearest neighbor of an atom at the saddle point, which are both equal to 6 for the bcc lattice, and E_m is the migration energy. The term $\Delta E_{ij}^{\text{non-broken}}$ in eq. (3.7) is zero here since no solute concentration change is involved in an A-atom jump. $\epsilon_{\alpha\text{-A}}^{sp(2)}$ is obtained from $\epsilon_{\alpha\text{-A}}^{sp(1)}$ using eq. (3.9). Vacancy bonds are calculated in a similar manner.

To calculate the saddle-point bond coefficients pertaining to B (Re) atoms, $\epsilon_{\alpha\text{-B}}^{sp(m)}$, one must consider local solute concentration changes. To this end, we resort to the configurations shown in Fig. 3.2(c). The A-B saddle-point coefficients $\epsilon_{\text{A-B}}^{sp(m)}$ are obtained from A-atom jumps, labeled '1' and '2' in Fig. 3.2(c), into the vacant site. The B-B saddle-point coefficient $\epsilon_{\text{B-B}}^{sp(1)}$ is computed assuming a B-atom (labeled '3' in the figure) jump into the vacancy. Equation (3.9) is then used to obtain the 2nn coefficients. All the necessary DFT calculations to calculate the saddle-point bond coefficients were performed as part of the present work, and are given in Table (3.3).

The migration energies of SIA and mixed-interstitials, the activation energy for SIA rotation, as well as the correlation factors at different temperatures are taken from the literature, and listed in Table (3.4).

Table 3.3: Saddle-point bond energy coefficients for vacancy jumps (in eV).

$\epsilon^{sp(1)}_{\text{A-A}}$	-2.5975	$\epsilon^{sp(2)}_{\text{A-A}}$	-0.5041
$\epsilon^{sp(1)}_{\text{A-B}}$	-2.6451	$\epsilon^{sp(2)}_{\text{A-B}}$	-0.5532
$\epsilon^{sp(1)}_{\text{A-V}}$	0.5465	$\epsilon^{sp(2)}_{\text{A-V}}$	0.1060
$\epsilon^{sp(1)}_{\text{B-A}}$	-2.5188	$\epsilon^{sp(2)}_{\text{B-A}}$	-0.4888
$\epsilon^{sp(1)}_{\text{B-B}}$	-2.5417	$\epsilon^{sp(2)}_{\text{B-B}}$	-0.4943
$\epsilon^{sp(1)}_{\text{B-V}}$	0.2902	$\epsilon^{sp(2)}_{\text{B-V}}$	0.0563

Table 3.4: Self-interstitial migration parameters. The jump distances for SIA, mixed-dumbbell migrations are $\delta{=}a_0\sqrt{3}/2$, a_0, respectively.

E_m^{AA}	0.003	Ref. [SYH14]
E_r^{AA}	0.43	Ref. [SYH14]
E_m^{AB}	0.12	Ref. [GME16]
f	$2.93 - 0.00055T$	Ref. [ZLH13]

3.1.5.5 DFT calculations

Density functional theory calculations were carried out using the projector augmented wave (PAW) method [Bl94, KJ99] as implemented in the Vienna *ab-initio* simulation package [KH93, KH94, KF96b, KF96a]. Since interstitial configurations involve short interatomic distances "hard" PAW setups that include semi-core electron states were employed with a plane wave energy cutoff of 300 eV.

Exchange and correlation effects were described using the generalized gradient approximation [PBE96] while the occupation of electronic states was performed using the first order Methfessel-Paxton scheme with a smearing width of 0.2 eV. The Brillouin zone was sampled using $5 \times 5 \times 5$ $\vec{k}$-point grids. (A detailed discussion of the effect of different computational parameters on the results can be found in Ref. [GE15]). All structures were optimized allowing full relaxation of both ionic positions and cell shape with forces converged to below 10 meV/Å. Migration barriers were computed using 4 × 4 × 4 supercells and the climbing image-nudged elastic band method with three images [HUJ00].

3.2 Results

3.2.1 Structural phase diagrams

Although our energy model includes thermodynamic information reflective of the phase stability of W-Re alloys, the model consists of a rigid lattice with bcc structure and is thus suitable only for a given, well-defined, concentration range. Our DFT calculations yield bond energies that are consistent with stable solid solutions from zero to approximately 40% at. Re [GME16]. This is confirmed by way of SGMC simulations performed as a function of composition and temperature in 64 × 64 × 64 computational cells. Figure 3.3 shows the set of stable compositions obtained as a function of the chemical potential for several temperatures. The figure shows a clear jump in the Re concentration at a temperature of approximately 100 K. This is typically indicative of a phase boundary, as two distinct phases characterized by widely different solute concentrations seem to coexist at the same temperature and chemical potential. This may be indicative of a miscibility gap between Re concentrations of a few percent and approximately 50 at.%, *i.e.* beyond the thermodynamic validity of our rigid lattice model. To further characterize the configurations obtained, we calculate the short-range order (SRO) of the configurations obtained according to the *Warren-Cowley* parameter [Cow50]:

$$\eta = N_B^{-1} \sum_i^{N_B} \left(1 - \frac{x_i(\mathrm{A})}{1 - X} \right) \tag{3.28}$$

which gives the SRO parameter η of Re atoms w.r.t. matrix W atoms, with $x_i(\mathrm{A})$ being the fraction of A atoms surrounding each solute atom i. The sum extends to all B atoms in the

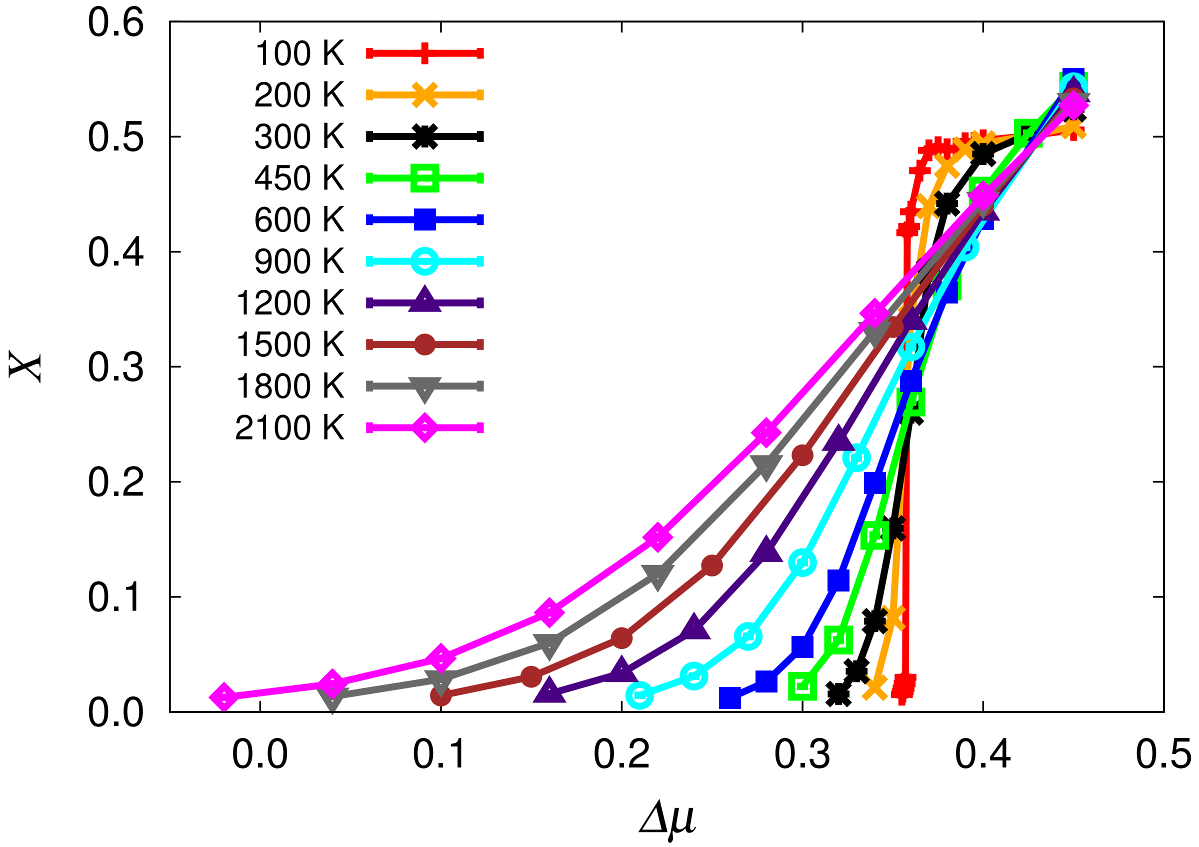

Figure 3.3: Solute composition X as a function of chemical potential $\Delta\mu$ at different temperatures.

system.

According to this definition, $\eta > 0$ implies phase separation, $\eta = 0$ represents an ideal solid solution, and $\eta < 0$ indicates ordering. However, the SRO parameter of a random solution has a range of ± 0.003 regardless of solute composition due to the random occurrence of dimers, trimers, and other small clusters. This band of *natural* order is marked with dashed lines in Figure 3.4, which shows the equilibrium SRO as a function of X for several temperatures. As the figure shows, the SRO parameter is near zero for dilute systems, and gradually becomes negative as the concentration increases. Based on the figure we conclude that equilibrium W-Re systems with up to ≈ 40 at.% solute content are consistent with random solid solutions with a weak tendency to ordering at higher concentrations. The corresponding T-X phase diagram is provided in Figure 3.5.

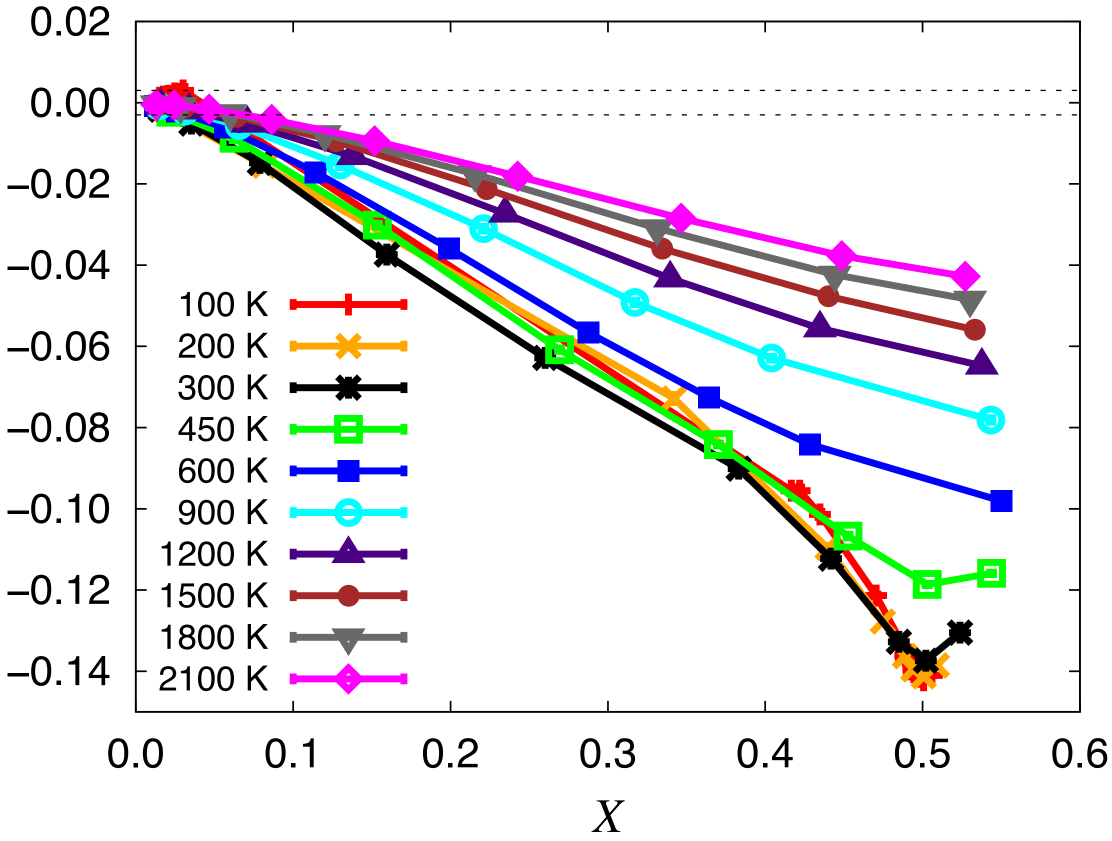

Figure 3.4: Short range order parameter η as a function of global solute composition X at different temperatures. The dashed line indicate the SRO interval caused by normal concentration fluctuations during the generation of atomistic samples.

3.2.1.1 Effect of vacancies on phase diagram

It is well known that non-equilibrium concentrations of defects can alter the thermodynamic behavior of an alloy. For the W-Re system, Wrobel *et al.* have studied the ternary W-Re-vacancy system and found that Re clustering occurs in the presence of non-thermodynamic vacancy concentrations [WNK17]. Although these are unrealistic homogeneous defect con-

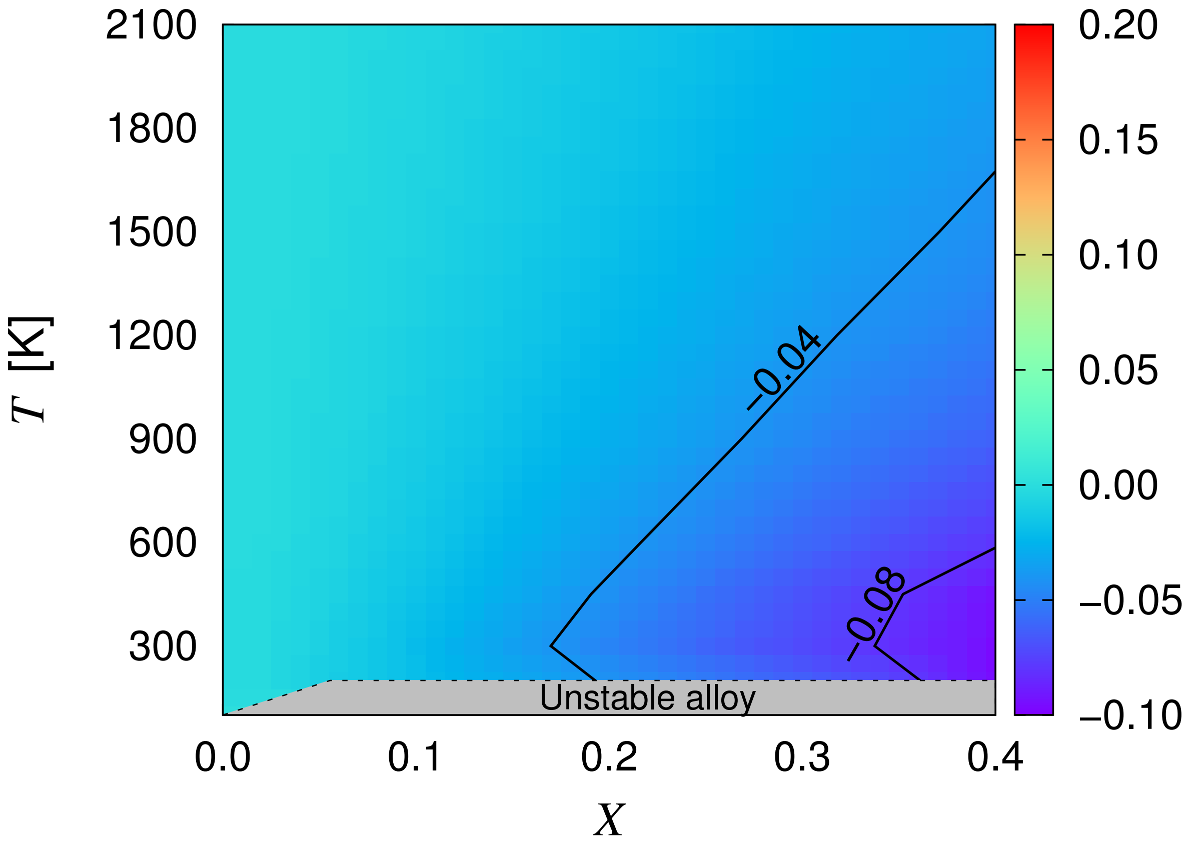

Figure 3.5: Structural phase diagram showing regions of changing SRO. The dashed lines are the limits of applicability of the rigid bcc lattice model. The system displays slightly negative SRO throughout the entire temperature-concentration space, indicating a preference to be in a solid solution state.

centrations, we can justify their study to hint at what could happen in highly heterogeneous situations, such as near defect sinks in irradiated materials. Clusters appear as semi-ordered structures of alternating solute and vacancy planes –a necessity given the short-range repulsion between Re atoms on the one hand, and vacancies on the other (cf. Table 3.1). Next, we carry out a similar study involving various vacancy concentrations, temperatures, and solute concentrations to obtain structural phase diagrams such as that shown in Fig. 3.5. Each configuration is optimized by combining SGMC steps with energy minimization steps following the process described in Section 3.1.3. Figure 3.6 shows the diagrams for vacancy concentrations of $C_v = 0.01,\ 0.1,\ 0.2,\ 0.5$ at.% using $64 \times 64 \times 64$ primitive cells.

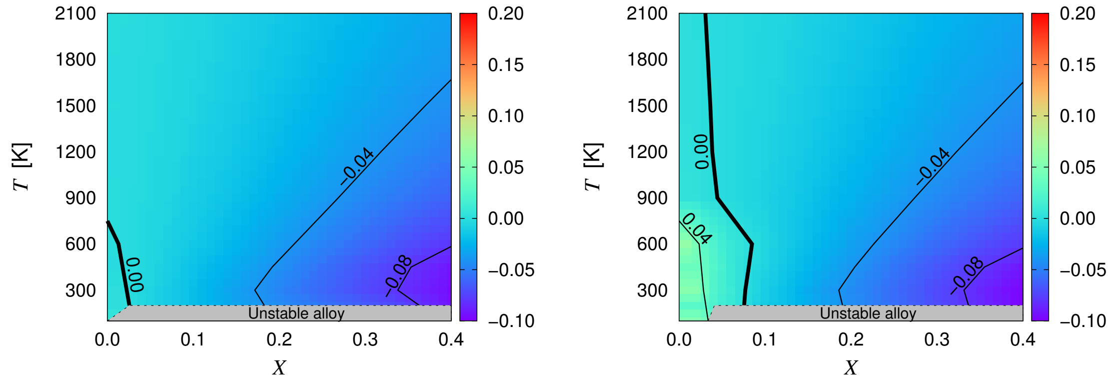

(a) $C_v = 0.01$ at.% (b) $C_v = 0.1$ at.%

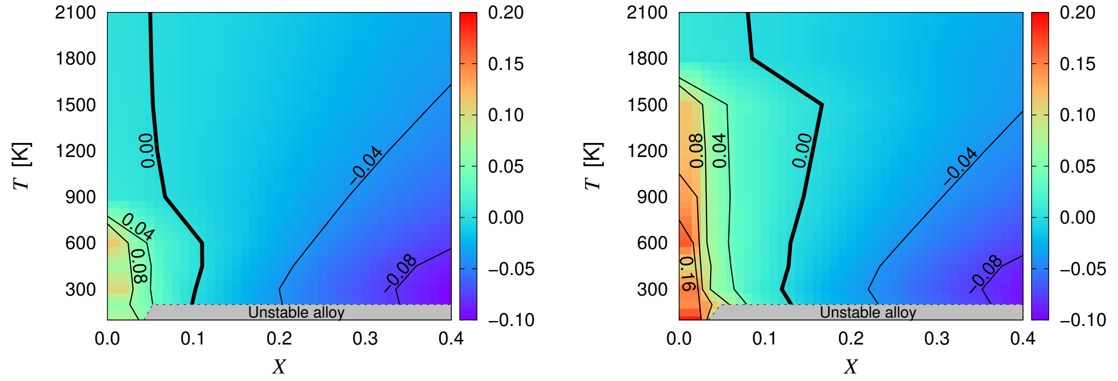

(c) $C_v = 0.2$ at.% (d) $C_v = 0.5$ at.%

Figure 3.6: Structural phase diagrams for four different vacancy concentrations. The diagrams clearly show the emergence of regions of solute segregation, characterized by positive SRO and a shifting of the transition phase boundary, $\eta = 0$, towards the right (higher concentrations).

As a representative example, Figure 3.7(a) shows the equilibrated configuration at 600 K, 1.8 at.% Re (which occurs for $\Delta\mu = 0.26$), and $C_v = 0.5$ at%. The figure shows several Re-vacancy clusters with an ordered structure, consistent with the study by Wrobel *et al.* [WNK17]. Due to their ordered structure, these solute-vacancy clusters form only at Re concentrations that are commensurate with the vacancy concentration in the system, *i.e.* at values of $X \lesssim 0.04$ in most cases.

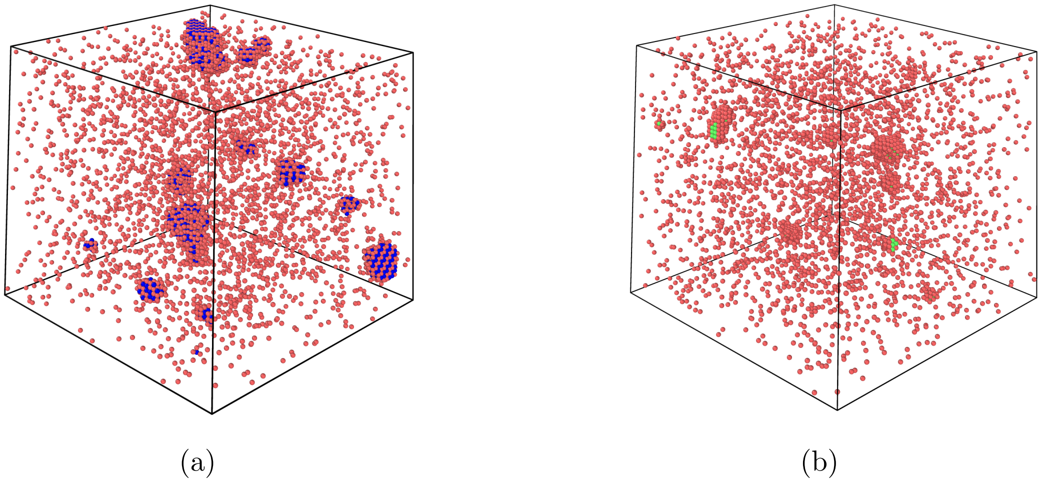

(a) (b)

Figure 3.7: Equilibrated configurations for W-Re alloys containing vacancy and mixed-interstitial at 600 K with (a) W-1.8at%Re alloy, 0.5 at% vacancy concentration and (b) W-1.4at%Re alloy, 0.1 at% mixed-interstitials, respectively. Red spheres represent Re atoms, colored blue or green ones represent the defect in each case.

3.2.1.2 Effect of interstitial defects on the phase diagram

Although vacancy concentrations such as those considered here are several orders of magnitude larger than the vacancy concentration in thermal equilibrium, one can expect such numbers under far-from-equilibrium conditions such as under high-dose or high-dose rate irradiation. The case is much more difficult to make for SIAs due to their much higher formation energy (3.2 vs. 10.2 eV, to take two representative numbers [GE15]). However, given the inclination of single interstitials to convert into mixed dumbbells in the presence of solute, it is of interest to repeat the same exercise of looking at the clustering propensity of Re in such cases. The results are shown in Figure 3.8 for a defect concentration of 0.1 at.%. The diagram reveals a stronger clustering tendency when interstitials are present compared to vacancies. Such an effect originates from both more attractive binding energies between mixed-interstitials and solute atoms, and between mixed-interstitials with themselves. A snapshot of the equilibrated atomistic configuration is shown in Fig. 3.7(b), where the precipitates are seen to form platelet-like structures with a mixed dumbbell core surrounded by substitutional solute atoms.

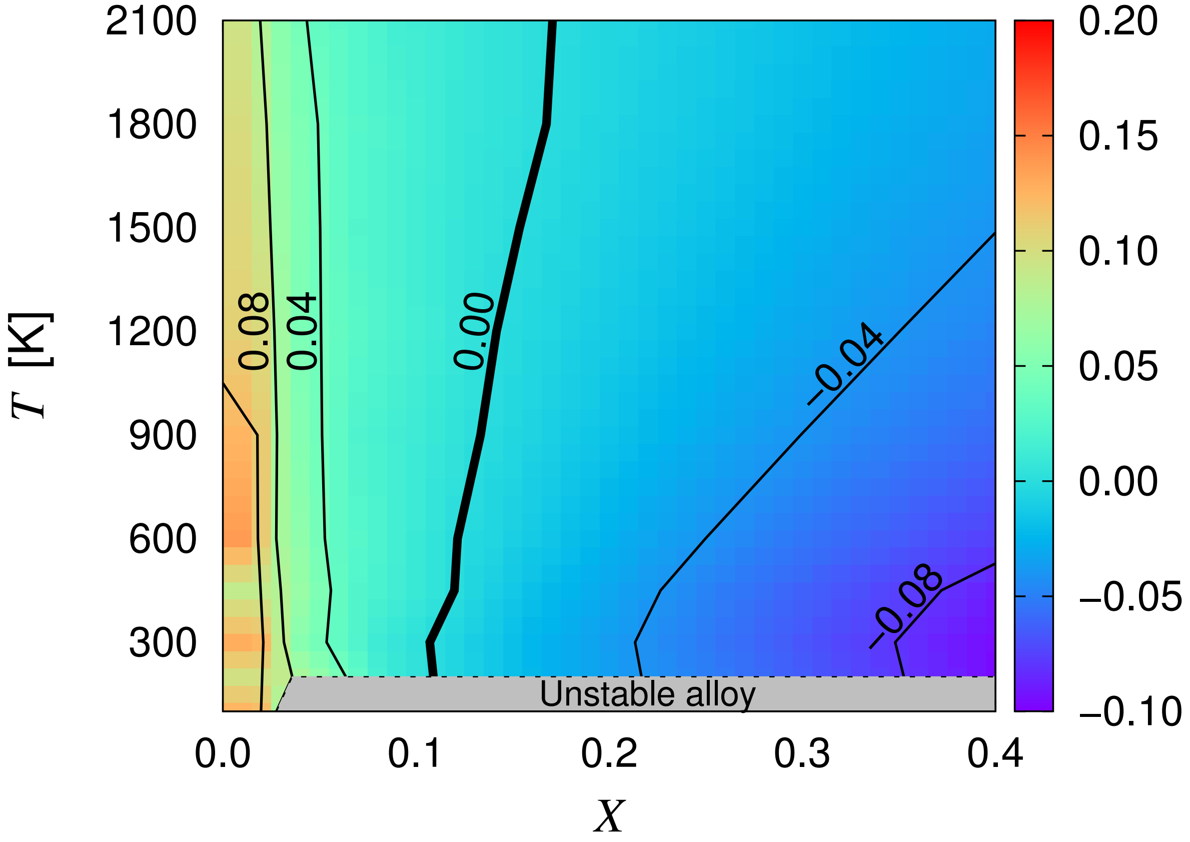

Figure 3.8: Structural phase diagram for 0.1 at.% mixed-dumbbell concentration. The diagram shows the emergence of regions of solute segregation, characterized by $\eta > 0$, up to $X = 0.1\%$.

3.2.2 Kinetic evolution of irradiated W-Re alloys

There are a number of factors that call for performing kMC simulations in W-Re systems.

1. First, equilibrium Monte Carlo calculations such as those performed in Section 3.2.1 do not provide information about the precipitate nucleation and growth mechanisms, as well as the timescales involved.

2. Second, there is clear experimental evidence of Re-cluster formation in the absence of vacancies. Hasegawa *et al.* [THH07,HTN11] and Hu *et al.* [HKF16] have both reported the formation of W-Re intermetallic precipitates after high-dose, fast neutron irradiation. Moreover, recent irradiation experiments have revealed the formation of Re-rich clusters with bcc structure, *i.e.* prior to their conversion into σ and/or χ precipitates. For example, Klimenkov *et al.* note that Re-rich particles not associated with cavities formed in neutron-irradiated single crystal W [KJR16]. As well, using atom-probe tomography Xu *et al.* have performed detailed analyses of Re-rich atmospheres in bcc W without detecting significant numbers of vacancies [XAB17].

3. New understanding regarding interstitial-mediated solute transport in W-Re alloys [SYH15, GME16], together with the results in Section 3.2.1.2, call for renewed simulation efforts incorporating these new mechanisms –in particular, the three-dimensional and associative nature of Re transport via mixed-dumbbell diffusion.

These considerations motivate the following study of the Re precipitation kinetics under irradiation conditions. First, however, we proceed to calculate diffusion coefficients and transport coefficients for defect species and solute atoms.

3.2.2.1 Calculation of diffusion coefficients

Tracer diffusion coefficients (i.e., in the absence of a concentration gradient) for vacancies, interstitials, and solute species in three dimensions are assumed to follow an Arrhenius temperature dependence:

$$D(T) = \nu f \delta^2 \exp\left(-\frac{E_a}{kT}\right) \tag{3.29}$$

where ν is the so-called *attempt* frequency, f is the correlation factor, δ is the jump distance, E_a is the activation energy, and $D_0 = \nu f \delta^2$ is the so-called diffusion pre-factor. Defect diffusivities can be obtained directly from this equation, with $E_a \equiv E_m$. For solute diffusion via the vacancy mechanism, the above expression must be multiplied times the probability of finding a vacancy in one of the 1nn positions, such that $D_0 = z_1 \nu f \delta^2$ and $E_a = E_m + E_f^{\mathrm{V}}$. However, fluctuations in local chemistry prevent us from using equations for homogeneous systems such as eq. (3.29) to calculate the diffusivities of solutes and vacancies as a function of the global solute concentration. In such cases, diffusion coefficients must be obtained by recourse to *Einstein*'s equation:

$$D = \frac{\langle \Delta r^2 \rangle}{6 \Delta t} \tag{3.30}$$

where $\langle \Delta r^2 \rangle$ is the *mean squared displacement* (msd) and Δt is the time interval. This formula assumes equilibrium defect concentrations, which are generally several orders of magnitude smaller than what a typical simulation cell can afford. For this reason, the time in eq. (3.30) is not directly the time clocked in the kMC simulations, Δt_{kMC}. Rather, it must be rescaled by a coefficient that accounts for the difference in defect concentration [BS02,NS12]:

$$\Delta t = \Delta t_{\mathrm{kMC}} \frac{C^{\mathrm{kMC}}}{C^{\mathrm{eq}}} \tag{3.31}$$

where C^{kMC} and C^{eq} are the defect concentrations in the kMC simulations and in equilibrium, respectively. For simulations involving only one defect, C^{kMC} is simply equal to the inverse of the number of atoms in the computational cell, $C^{\mathrm{kMC}} = N^{-1}$, while $C^{\mathrm{eq}} = \exp(-E_f/k_B T)$, where E_f is the *instantaneous* defect formation energy, *i.e.* calculated accounting for the local chemical environment. This is the approach used for vacancy mediated diffusion, with $E_f^{\mathrm{V}} = \sum_i \epsilon_{\mathrm{V}\text{-}\alpha_i}$, where α_i symbolizes the neighboring atoms forming a bond with the vacancy. During simulations of solute and vacancy diffusion, E_f^{V} is updated in every Monte Carlo time step and time rescaling is performed on the fly. The starting configuration for all calculations involving solute atoms is the equilibrated alloy as obtained in Section 3.2.1 using SGMC simulations. The results for the vacancy and solute diffusivities, D_{v} and D_{s}, can be seen in Figure 3.9, while the parameters resulting from fitting the data points in the above figures to eq. (3.29) are collected in Table 3.5. The details of obtaining diffusion coefficients from KMC simulations can be seen in Appendix A.1. While D_{v} displays a moderate dependence with the solute concentration, D_{s} is quite insensitive to it.

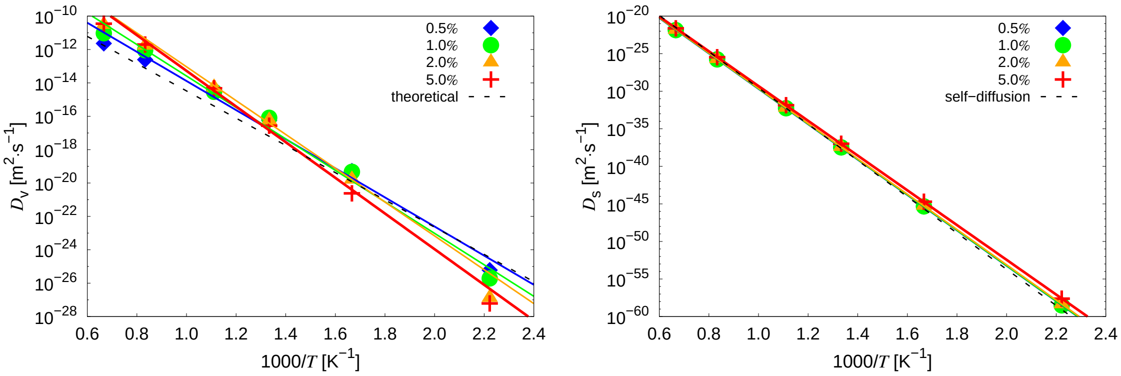

(a) Vacancy diffusion

(b) Solute diffusion

Figure 3.9: Diffusivities of vacancies and solute atoms as a function of temperature and alloy concentration. The solid lines correspond to the Arrhenius fits shown in Table 3.5, while the dashed line corresponds to eq. (3.29).

As discussed in Section 3.1.5.4, self-interstitial migration occurs by way of fast sequences of $\langle 111\rangle$ transitions punctuated by sporadic rotations, whereas mixed dumbbell diffusion occurs via random $\langle 100\rangle$ hops in three dimensions. Interstitial diffusivities of both types can be calculated straightforwardly by using eq. (3.29) parameterized with the data in Table 3.4.

3.2.2.2 Calculation of transport coefficients

Within linear response theory, mass transport can be related to chemical potential gradients via Onsager's phenomenological coefficients. The value and sign of these transport coefficients can provide important physical information about the nature of solute and defect fluxes. On a discrete lattice, the transport coefficients L_{ij} coupling two diffusing species can be calculated as [SSM16, AL03]:

$$L_{ij} = \frac{1}{6V}\frac{\langle \Delta r_i \Delta r_j \rangle}{\Delta t} \tag{3.32}$$

where V is the total volume of the system; Δr_i is the total displacement of species i, and Δt is the rescaled time. Here we focus on the relationship between solutes and vacancy and

Table 3.5: Diffusion parameters for vacancy and solute diffusion as a function of solute concentration.

X [at. %]	D_0 [m^2·s^{-1}]	E_m [eV]
Vacancy diffusion		
0.0 (eq. (3.29))	4.84×10^{-7}	1.62
0.5	6.86×10^{-6}	1.73
1.0	6.92×10^{-5}	1.87
2.0	1.26×10^{-3}	2.08
5.0	2.57×10^{-3}	2.16
Solute diffusion		
0.0 (eq. (3.29))	3.87×10^{-6}	$1.62 + 3.17 = 4.79$
0.5	7.56×10^{-7}	4.67
1.0	7.80×10^{-7}	4.67
2.0	7.89×10^{-7}	4.66
5.0	6.75×10^{-7}	4.59

solute atoms, $L_{\text{B-B}}$, and $L_{\text{B-V}}$, as a function of temperature and solute content. Due to the associative transport mechanism of AB interstitials, the corresponding transport coefficient relating interstitials with solute atoms is always positive and we obviate its calculation. Figure 3.10a shows the results for $L_{\text{B-B}}$, which displays an Arrhenius temperature dependence and is always positive. The dependence with solute concentration is not significant up to 5%, with an average activation energy of 4.7 eV –very similar to the solute diffusion activation energy– and a prefactor of approximately 3.9×10^{20} m^{-1}·s^{-1}. $L_{\text{B-B}}$ is by definition related to the solute diffusion coefficient presented above.

In Figure 3.10b we plot the ratio $L_{\text{B-V}}/L_{\text{B-B}}$. Two observations stand out directly from the figure. First, the value of $L_{\text{B-V}}$ is always negative (the exception being at 450 K, when is almost zero). This indicates a reverse coupling between solutes and vacancies, *i.e.* vacancy fluxes oppose solute fluxes. The implications of this calculation will become clearer when we study solute precipitation in the next section. Second, $L_{\text{B-V}}$ is on average about an order of magnitude larger than $L_{\text{B-B}}$,which is to be expected for substitutional solutes moving by a vacancy mechanism.

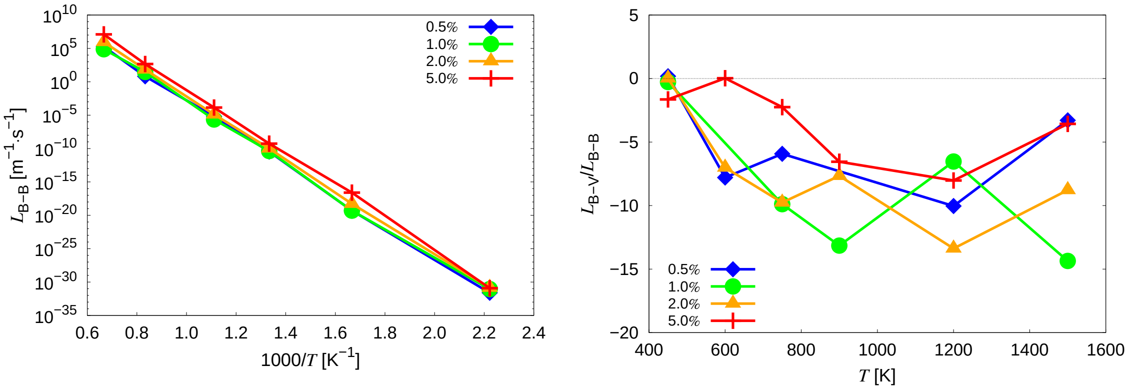

(a) Solute-solute transport coefficient

(b) Solute-vacancy transport coefficient

Figure 3.10: Phenomenological transport coefficients for solute-solute and vacancy-solute interactions.

3.2.2.3 Kinetic Monte Carlo simulations

To narrow down the large parametric space associated with irradiation of W-Re alloys (Re concentration, temperature, dose, dose rate, etc.), we resort to the study performed in Sections 3.2.1 and 3.2.1.1. It was seen there that segregation occurs most favorably at low solute compositions. For this reason, and to enable comparison with the work by Xu *et al.* [XBA15,XAB17], we choose a W-2Re (at.) alloy for our study. By way of reference, this would correspond to the transmutation fraction attained after a dose of 12 dpa or 4 full-power years in DEMO's first wall according to Gilbert and Sublet [GS11]. When relatively high concentrations of defects are present –as one might expect during irradiation– precipitation is also favored at high temperatures, so here we carry out our simulations between 1700 and 2000 K. We use box sizes of 64^3 and 80^3 with a damage insertion rate of 10^{-3} dpa per second. As shown in Appendix A.2, the equivalence relation that exists between both box sizes enables us to compare them directly. Eight independent simulations were conducted for statistical averaging and stochastic error estimation.

It is seen that, on average, a precipitate starts to grow after a waiting time of ≈ 21 seconds (or ≈ 0.02 dpa). This time can be regarded as the average *incubation* (nucleation) time for the conditions considered in the study. Figure 3.11 shows the mean size from all eight cases as a function of *growth* time, *i.e.* initializing the clock after the cluster nuclei are formed regardless of the observed incubation time. The dashed line in the figure is the associated spherical growth trend, which the precipitates are seen to follow for approximately 20 s. Subsequently, growth stops at a saturation radius of 4 nm, which is seen to be the stable precipitate size. A surface reconstruction rendition of one of the precipitates is also provided in the figure as a function of time. This depiction as a compact convex shape is not intended to represent the true diffuse nature of the cluster, and is only shown as an indication of the cluster average size and shape. The distribution of cluster sizes at beginning, during growth, and after saturation can be seen in Appendix A.3.

The next question we address is the solute concentration inside the precipitate. Xu *et al.* [XBA15, XAB17] have performed detailed atom probe analyses of radial concentration profiles at 573 and 773 K and find that the precipitates that form might be better characerized as 'solute clouds', reaching concentrations of around 30% in the center gradually declining as the radius increases. Our analysis is shown in Figure 3.12, with results averaged over the 8 cases tried here. The figure shows that the concentration at the precipitate core (within the inner 1.5 nanometers) surpasses 50% –the thermodynamic limit for the formation of intermetallic phases–, which could provide the driving force for such a transformation. Because our energy model is not valid above the solid solution regime, we limit the interpretation of such phenomenon however. What is clear is that the precipitates are not fully-dense, even near their center. In fact, the relative solute concentration appears to diminish near the precipitate core once the saturation point has been reached.

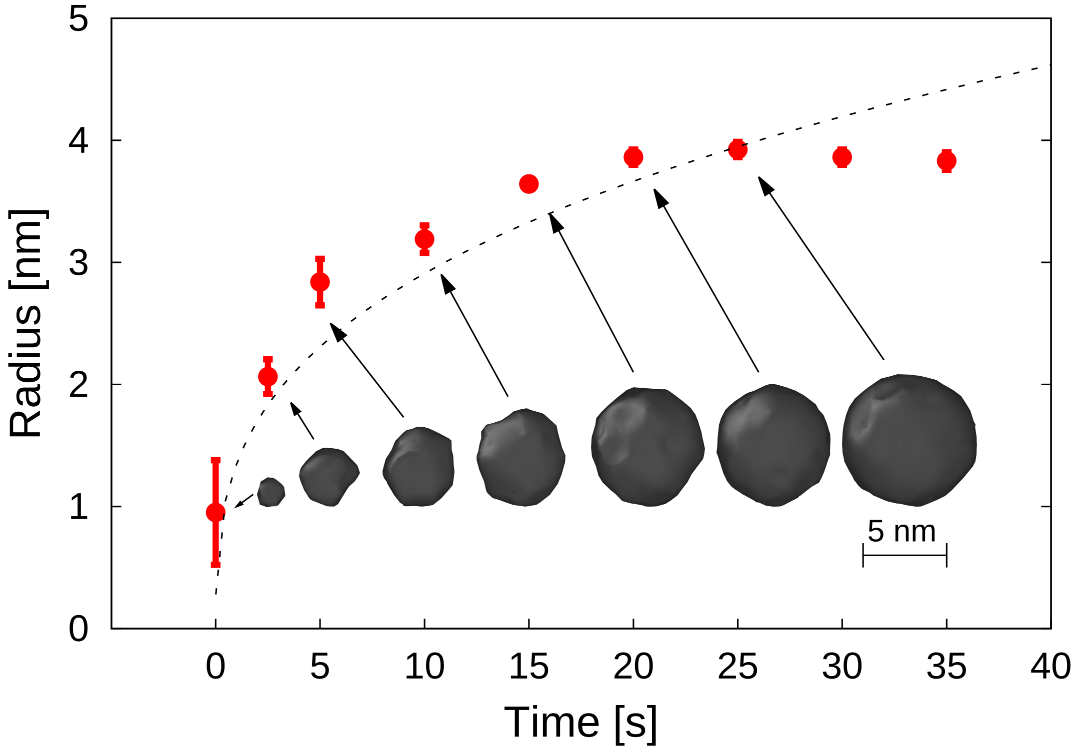

Figure 3.11: Precipitate growth with time at 1800 K and 10^{-3} dpa·s^{-1} in a W-2.0% at. Re alloy. The dashed line represents perfect spherical growth (cf. A.2). A surface reconstruction rendition of one precipitate at various times is provided as inset.

Finally, we address the issue of whether it is vacancy or interstitial mediated transport that is primarily responsible for solute agglomeration and the formation of Re-rich clusters. To this end, we track the evolution with time of the incremental SRO change brought about by any given kMC event during the formation stage of one the precipitates discussed above. The results are given in Figure 3.13, where contributions from SIA and mixed interstitial jumps, vacancy jumps, and Frenkel pair insertion are plotted. These results conclusively demonstrate that mixed-interstitial transport is dominant among all other events to bring solute together. Vacancies, on the other hand, serve a dual purpose. They first act as a ‘hinge’ between solute atoms that would otherwise repel, much in the manner shown in

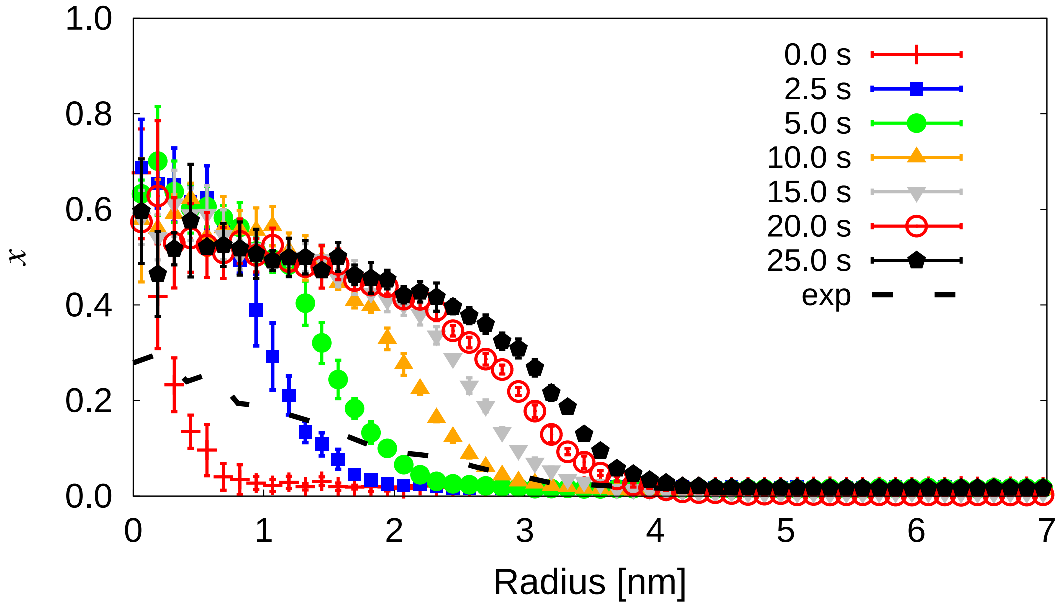

Figure 3.12: Radial concentration profile as a function of time for the precipitates formed in the kMC simulations. The experimental results are taken from the work by Xu *et al.* [XAB17].

Fig. 3.7(a). These results in an initial positive contribution to the SRO, as shown in the inset to Fig. 3.13, by forming dimers, trimers, or other small solute clusters. However, once a critical nucleus forms and starts to grow, vacancies reverse this behavior and act to dissolve the precipitate (differential SRO turns negative in Fig. 3.13), mostly by making the precipitate/matrix interface more diffuse. We also performed a simple confirmation on the dual purpose of vacancies by performing KMC simulations with only one vacancy from an initial configuration of complete phase separation and random configuration, which is discussed in Appendix A.4. As expected, Frenkel pair insertion has practically no effect on the overall precipitate evolution.

The precipitate grows by a sustained capture of mixed interstitials and subsequent attraction of vacancies. This gives rise to localized recombination at the precipitate, which makes the precipitates incorporate solute atoms over time. Figure 3.14 shows the spatial location of the recombination events during a period of 2.0 s before, during, and after precipitate growth.

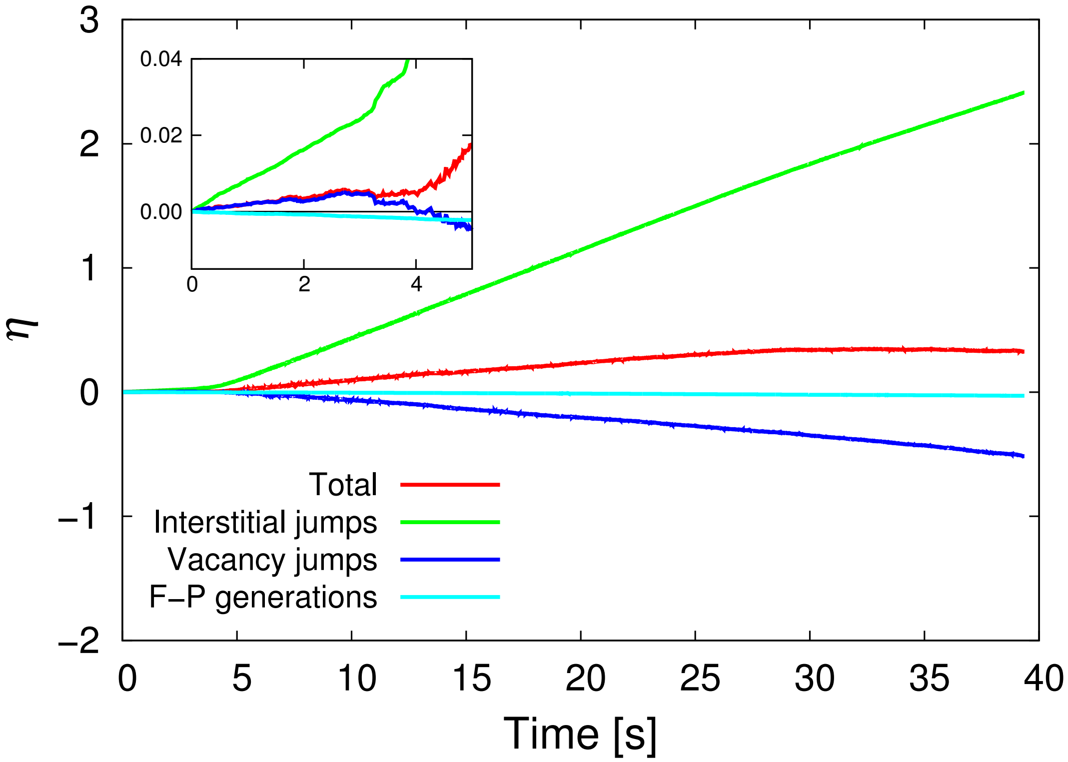

Figure 3.13: Evolution of the differential SRO during the nucleation and growth in the kMC simulations.

The figure clearly shows that, once formed, the precipitate becomes a preferential site for recombinations, which results in further growth and eventually in saturation. Because the primary source of solute is via interstitial transport, which also brings W atoms, the precipitates are never fully compact ($x \sim 1$). Instead, maximum concentrations of around 50% are seen near the center when the precipitates reach their saturation size of 4-nm radius. As we will discuss in the next section, this is consistent with experimental measurements and observations of both coherent bcc clusters and incoherent σ and χ phases.

Simulations performed with defect sinks in the same temperature range simply result in solute segregation in the manner described in Section 2.3. Radiation induced precipitation results from the onset of defect fluxes to the sinks, providing sufficient competition to delay the formation of bulk precipitates beyond the time scales coverable in our kMC simulations.

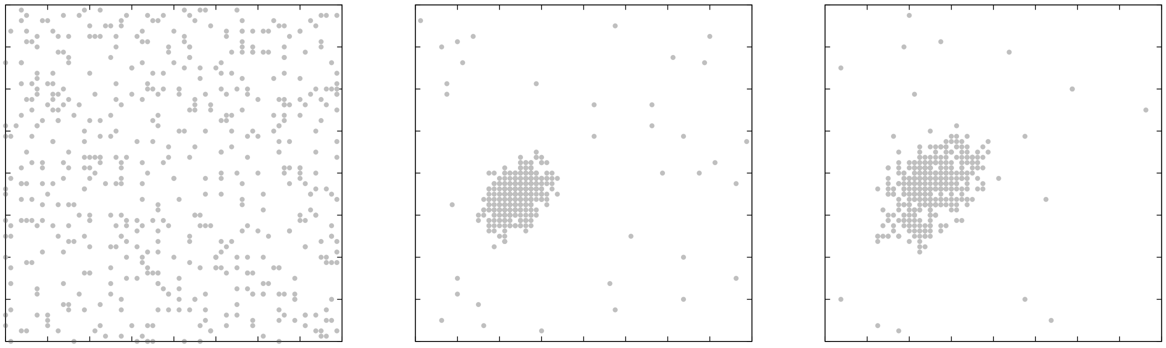

(a) During cluster nucleation. (b) During precipitate growth. (c) After size saturation.

Figure 3.14: Spatial distribution of recombination events for several stages of precipitate evolution.

More information is provided in the Appendix A.5.

3.3 Discussion and conclusions

3.3.1 Mechanism of nucleation and growth

On the basis of our results, the sequence of events that leads to the formation of Re-rich precipitates in irradiated W-2Re (at%) alloys is as follows:

1. First, a Frenkel pair is inserted in the computational box following the procedure specified in Section 3.1.4. As interstitials enter the system, they perform a one-dimensional migration until they encounter a solute atom, after which they become mixed AB dumbbells capable of transporting solute in 3D. As these mixed dumbbells diffuse throughout the lattice, they encounter substitutional solute atoms and become trapped forming a B-AB complex with a binding energy of 0.15 eV (cf. Table 3.1).

2. The vacancy in the Frenkel pair migrates throughout the lattice contributing to the formation of small Re complexes (dimers, trimers, tetramers, etc.). Vacancy motion does not necessary imply solute drag, as indicated by the negative value of transport coefficients in Section 3.2.2.2. However, as the evidence from the Metropolis Monte Carlo simulations in Fig. 3.6 suggests, they can form small complexes of stable Re-V clusters.

3. The vacancy can become locally trapped in the small Re-V complexes mentioned above. However, at the high temperatures considered here, it is likely to de-trap and continue migrating until it finds the immobilized interstitial from (1), as this provides the largest thermodynamic driving force to reduce the energy of the crystal. When the vacancy and the interstitial meet, another small Re cluster is formed. Throughout this process, both mixed interstitial and vacancy hops are characterized by an increasing differential SRO parameter (cf. Fig. 3.13).

4. Eventually, one of these Re clusters grows larger than the rest due to natural fluctuations. When that happens, this larger cluster has a higher likelihood of attracting the next V-AB recombination event. This signals the onset of the growth process, fueled by continued attraction of AB mixed dumbbells and the subsequent associated recombination. At this stage, vacancies reverse their role as solute-atom 'hinges' and begin to contribute to cluster dissolution (negative differential SRO parameter in Fig. 3.13). This results in the development of a more or less diffuse interface as the precipitate grows, which delays the next recombination event and slows down growth.

5. Although the precipitate continues to be the main pole of attraction for vacancy-interstitial recombinations (cf. Fig. 3.14), the system reaches a point where most of the solute is consumed into a diffuse precipitate that halts further growth. Vacancies then have more time to interact with the interface atoms before the next recombination event, which results in a smearing of the precipitate interface. In the absence of sinks, or other precipitates, the existing cluster is the sole focus of solute agglomeration, which allows it grow to its maximum size for the current alloy content of 2% Re. It

is to be expected that with competing solute sinks, the precipitates might either be slightly smaller in size or less solute-dense internally.

This qualitative explanation is built on direct evidence and interpretation from our results, described in detail in Section 3.3. However, to support some of the above points more explicitly, we provide additional details as Supplementary Information.

Interestingly, the essential features of our mechanism were originally proposed by Herschitz and Seidman [HS84, HS85] on the basis of atom probe observations of neutron-irradiated W-25Re alloys. Remarkably, these authors had the intuition to propose the basic ingredients needed to have Re precipitate formation identified in our work with the more limited understanding available at the time.

3.3.2 Brief discussion on the validity of our results

With the computational resources available to us, we can reasonably simulate systems with less than 500,000 atoms into timescales of tens of seconds. This has proven sufficient to study Re clustering at high temperatures, where vacancy mobility is high and comparable to mixed-interstitial mobility. Recall from the previous section that the formation of clusters is predicated on the concerted action of both defect species, with mixed interstitials becoming trapped at small Re clusters followed by a recombination with a vacancy that makes the cluster grow over time. Clustering and precipitation of Re in irradiated W has been seen at temperatures sensibly lower than those explored here, such as 573 and 773 K for ion-irradiated W-Re [XBA15,EXH15,XAB17], 773 and 1073 K for neutron irradiated W in HFIR [HKF16], 1173 K in neutron irradiated W in the HFR reactor [KJR16], and by Williams *et al.* at 973∼1173 K in EBR-II [WWB83]. The work by Hasegawa *et al.* in JOYO [THF08, HTN11] does cover –by contrast– a similar temperature range as ours. The principle is that the mechanism proposed here can be conceivably extended to lower temperatures without changes with just a timescale adjustment due to the significantly slower mobility of vacancies at those temperatures. This would require simulated times that are far too long to cover with kMC.

An intrinsic limitation of our model is that it is based on a rigid bcc lattice and cannot thus capture the transition of precipitates to the intermetallic phase. As such, our model does not necessarily reflect the true microstructural state when the local concentration surpasses 40∼50%, which is when phase coexistence is expected to occur according to the phase diagram [EPG00]. However, our simulations are useful to determine the kinetic pathway towards the accumulation of Re concentrations in the vicinity of that amount. Neutron irradiation experiments such as those performed at JOYO and HFIR reveal the formation of acicular σ and χ precipitates [WWB83,THF08,HTN11,HKF16], which presumably indicates reaching local values of Re concentration of or higher than 40∼50% at the site of precipitate formation. However, in controlled ion irradiation experiments [XBA15,EXH15,XAB17] there is clear evidence that the precursor to the formation of these intermetallic precipitates are noncompact Re-rich clusters with bcc structure. We cannot but speculate how the transition from these solute-rich clusters to well-defined line compounds σ and χ takes place (perhaps via a martensitic transformation, as in Fe-Cu systems [EMS13]), but it is clear that it is preceded by the nucleation and growth of coherent Re clusters. In our simulations, we find that the clusters have a maximum concentration of ≈50% in the center, in contrast with Xu *et al.*, who observe concentrations no larger than 30%. This disparity may simply be a consequence of the different temperatures considered relative to our simulations (773 vs 1800 K), as it is expected that the accumulation of solute by the mechanism proposed here will be accelerated by temperature.

As well, our Re clustering mechanism is predicated on the insertion of Frenkel pairs, when it is well known that fast neutron and heavy-ion irradiation generally result in the formation of clusters of vacancies and interstitials directly in displacement cascades. However, even here tungsten is somewhat of a special case. Recent work [SDN13, YSM15, SNR15a] suggests that most of the defects in high-energy (>150 keV) cascades in W appear in the form of isolated vacancies and interstitials. This, together with the fact that most displacement cascades for non-fusion neutrons and heavy ions have energies well below the 150-keV baseline, gives us confidence that our mechanism would be operative even in such scenarios.

3.3.3 Implications of our study

Beyond the obvious interest behind understanding the kinetics of Re-cluster formation in irradiated W-Re alloys, our model is useful to interpret other physical phenomena. For example, it is well known that swelling is suppressed in irradiated W-Re alloys compared to pure W [MNM74]. By providing enhanced avenues for interstitial-vacancy recombination, small Re clusters capture mixed interstitials, allowing sufficient time for vacancies to subsequently find them and suppressing the onset of swelling. Intrinsic 3D mobility of mixed dumbbells is likely to favor recombination as well. Note that this explanation for swelling suppression is different to the one proposed for Fe-Cr alloys, where 1D migration of SIAs is restrained by Cr atoms [TMB05].

Finally, the mechanisms proposed here refer to homogeneous nucleation, *i.e.* Re clustering occurs without any assistance from RED or RIP, and hence without the need for defect sinks. This is again a remarkable feature of these alloys, confirmed in several studies [HS85, XAB17, KJR16]. As noted by Herschitz and Seidman, "The coherent precipitates were not associated with either linear or planar defects or with any impurity atoms; i.e. a true homogeneous radiation-induced precipitation occurs in this alloy", or by Klimenkov *et al.*, who point out that "The formation of Re-rich particles with a round shape was detected in the single crystal material. These particles were formed independently of cavities". We leave out heterogeneous precipitation at voids, as the evidence in the literature is conflicting at this stage: discounted in some works [HS85, XAB17] and observed in others [KJR16].

3.3.4 Sensitivity of results to model uncertainties

The issue of sensitivity of *mesoscale* models to atomistic parameters is of course of extraordinary importance and the subject of larger methodologies such as uncertainty quantification (UQ). This is especially true in a case like ours, where properties evaluated at the atomic-molecular scale are transferred to the mesoscopic scale. Sources of uncertainty can originate in numerical uncertainty, model uncertainty, and parametric uncertainty. Numerical uncertainties are related to the finite time of the dynamic simulation, the number of particles, and the accuracy of the computers used. Model uncertainty comes from the specific Hamiltonian representation used here and the boundary conditions employed. Parametric uncertainties stem from errors in parameter values due to noisy or insufficient calculations, or in approximations used to calculate them. In the specific case of DFT calculations, recent efforts point to the need to propagate errors in the formulation of the functionals using proper statistical analysis techniques [MSH15, Han11]. The intrinsic stochasticity of kMC simulations results in another sort of uncertainty related to random number generators and the number of independent cases run. All told, this aspect of the simulations is the least understood, and is starting to receive increased attention in the literature [Car08, CPL13, TPK15]. UQ requires dedicated efforts, well beyond the scope of this work, and therefore here we simply note the potential sources of uncertainty in our simulations and alert readers as to their potential implications.

CHAPTER 4

Stochastic cluster dynamics simulation study on W-Re alloy and its strength

MC simulations can give us insight about the thermodynamic equilibrium and kinetic evolutions of microstructures of W-Re alloy under irradiation. However, due to the computational limitations, the system size and simulation time are limited to nm scale with ~ 0.01 dpa, in which we can only obtain one precipitate in the system. In order to extend the study to micrometer scale with ~ 1 dpa, we have to perform simulations on continuum regime. In this chapter we study the W-Re alloy using stochastic cluster dynamics (SCD) simulations. The parameters were obtained from previous MC simulations. The results of SCD simulations can be used to predict the cluster distributions of W metal in irradiation environments and further estimate the effect of irradiation-induced hardening.

4.1 Theory and methods

4.1.1 Stochastic cluster dynamics method

SCD simulation is a stochastic variant of the mean-field rate theory technique, alternative to the standard ODE-based implementations, that eliminates the need to solve exceedingly large sets of ODEs and relies instead on sparse stochastic sampling from the underlying kinetic master equation [MB11,MH12]. Rather than dealing with continuously varying defect concentrations in an infinite volume, SCD evolves an integer-valued defect population Ni in a finite material volume V, thus avoiding combinatorial explosion in the number of ODEs. This makes SCD ideal to treat problems where the dimensionality of the cluster size space is high, e.g., when multi-species simulations are of interest. SCD recasts the standard ODE system into stochastic equations of the form:

$$\frac{dN_i}{dt} = \tilde{g}_i - \sum_i \tilde{s}_{ij} N_i + \sum_j \tilde{s}_{ji} N_j - \sum_{i,j} \tilde{k}_{ij} N_i N_j + \sum_{j,k} \tilde{k}_{jk} N_j N_k \tag{4.1}$$

where the set $\{\tilde{g}, \tilde{s}, \tilde{k}\}$ represents the reaction rates of 0^{th} (insertion), 1^{st} (thermal dissociation, annihilation at sinks), and 2^{nd} (binary reactions) order kinetic processes taking place inside V. The detailed description of the SCD method can be found in Ref. [MB11].

In this work, we performed SCD simulations to study W-Re alloy under irradiation. The cluster species contained in the system are Re atoms/clusters, SIAs/SIA loops, vacancies/voids, and clusters with more than one species including V-Re and SIA-Re clusters. From pervious DFT calculation work and our previous kMC simulation study, it has been discovered that mixed-dumbbells play an important role on the segregation of W-Re alloy under irradiation. Therefore, in this work, we carefully added the mechanism of clustering and transport of mixed-dumbbells. To keep the simulation simple, mixed-dumbbells are not explicitly treated as a new species; instead, a SIA_1Re_1 cluster is considered as a mixed-dumbbell.

In this work, system volume is set to be $10^{-20}m^3$ and it is ensured that at all times $\sqrt[3]{V} > l$, where l is the maximum of the diffusion lengths l_i of all species i in the system, defined as:

$$l = \max_i \{l_i\},$$

$$l_i = \sqrt{\frac{D_i}{R_i}}$$

Here, D_i and R_i^{-1} are the diffusivity and the lifetime of a mobile cluster within V. From Eq. (4.1), $R_i = \tilde{s} + \sum_i \tilde{k}_{ij} N_i$. In other words, we ensure that the characteristic diffusion length of any defect species is contained within the simulation volume at any given time.

4.1.2 Method parameterization

The input parameters for the SCD method are defect insertion rates and distributions (0^{th}-order), dissociation energies (1^{st}-order), and diffusion coefficients (1^{st}- and 2^{nd}-order). Below we will discuss the parameterizations based on previous DFT calculation work and our previous study of kinetic and Metropolis Monte Carlo (MC) simulations [HGZ17, HM16].

4.1.2.1 Irradiation damage

There are two types of irradiation damage: neutron damage and W to Re transmutation. For the neutron damage, neutrons first hit on the material, resulting in primary knock-on atoms (PKA) with various PKA energies. The PKA then create defects with equal numbers of vacancies and interstitials. When a neutron damage event is performed, a primary PKA energy E_{PKA} is randomly generated according to the recoil energy distribution of DEMO, HFIR, or JOYO reactors, which are the cumulative probability distribution functions (CPDF) C(E_{PKA}). The distributions are shown in Fig. (4.1). The defects are then inserted into the system according to the relations of defect distribution to PKA energy.

The distribution of defects generated by a PKA has been studied by experiments and molecular dynamics (MD) simulations [SNR15b]. Recently, Setyawan and his colleagues performed MD simulations to study defect distributions with different PKA energies E_{PKA} [SNR15b]. The results on number of Frenkel pairs as well as fractions of clustered SIAs vacancies as functions of PKA energy were extracted and used in this study. The number of

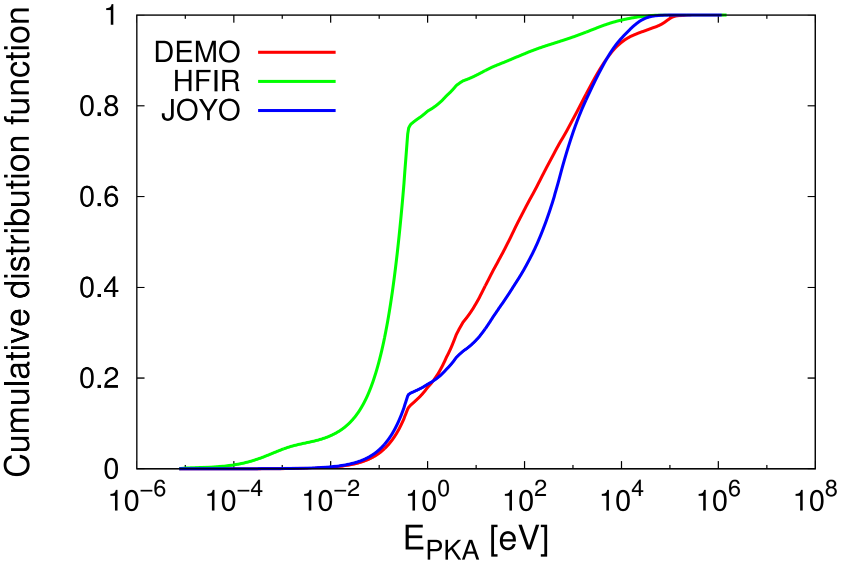

Figure 4.1: Recoil cumulative distribution function (CPDF) in W for DEMO, HFIR, and JOYO reactors.

Frenkel pairs N_F as a function of PKA energy exhibited two regimes and was fitted to linear regressions in a logarithmic graph:

$$\Delta E_{ij} = \begin{cases} N_F = & 0.4172\left(\frac{E_{PKA}}{E_d}\right)^{0.74}, \quad \text{if } \frac{E_{PKA}}{E_D} < 341.42 \\ N_F = & 0.0126\left(\frac{E_{PKA}}{E_d}\right)^{1.34}, \quad \text{otherwise} \end{cases} \tag{4.2}$$

where $E_d = 128\ eV$ is the calculated average displacement threshold energy. The temperature dependency is much smaller and omitted in this study. The fractions of clustered SIAs and vacancies f_c^{SIA}, f_c^V, on the other hand, depend on E_{PKA} and temperature, respectively. The fitting results for SIAs and vacancies are given as:

$$f_c^{SIA} = 0.09021\left(\frac{E_{PKA}}{E_d}\right)^{0.326} \tag{4.3}$$

$$f_c^V = 0.625 - 1.750 \times 10^{-4}T \tag{4.4}$$

where T is temperature. With the input parameters, defect distributions can be generated using binomial sampling.

The Re transmutation rates were calculated from data from the reactors, which are listed in Table (4.1). It can be seen that the transmutation rate for HFIR is extremely high with a value much larger than the other two reactors.

Table 4.1: Re transmutation rates for DEMO, HFIR, and JOYO.

Reactor	Transmutation rate [at%/s]
DEMO	1.173×10^{-8}
HFIR	7.374×10^{-7}
JOYO	6.879×10^{-8}

4.1.2.2 Diffusion coefficients

The mobile species in the SCD simulations are: single and pure SIA clusters, single and pure vacancy clusters, as well as single Re atoms and single mixed-dumbbells (SIA_1Re_1). Tracer diffusion coefficients (i.e., in the absence of a concentration gradient) for an object in 3-D movement is assumed to follow an Arrhenius temperature dependence:

$$D(T) = \nu f \delta^2 \exp\left(-\frac{E_a}{kT}\right) \tag{4.5}$$

where ν is attempt frequency, f is the correlation factor, δ^2 is the jump distance, E_a is the activation energy, and $D_0 = \nu f \delta^2$ is the diffusion pre-factor. Defect diffusivities can be obtained directly from this equation, with $E_a \equiv E_m$. For solute diffusion via the vacancy mechanism, the above expression must be multiplied times the probability of finding a vacancy in one of the $1^{st} - nn$ positions, such that $D_0 = z_i \nu f \delta^2$ and $E_a = E_m + E_f^V$.

In our previous work, we have performed kinetic MC simulations of W-Re alloy with only one vacancy at various temperatures and solute concentrations [HGZ17]. The diffusion coefficient of Re atom in the simulations were obtained by Einstein's equation:

$$D = \frac{\langle \Delta r^2 \rangle}{6\Delta t} \tag{4.6}$$

where $\langle \Delta r^2 \rangle$ is the mean squared displacement (msd) and Δt is the time interval. It should be noted that since a solute atom migrates by exchanging position with a vacancy, the diffusion coefficient of a solute atom depends on the concentration of vacancy. Therefore, the time interval Δt must be corrected by $\Delta t = \Delta t_{kMC} \frac{C^{kMC}}{C^{eq}}$, where $C^{kMC} = 1/Volume$ is the vacancy concentration of the kMC simulation and $C^{eq} = \exp(-E_f/k_B T)$ is the equilibrium vacancy concentration. The resulting diffusion coefficients of vacancy and solute atom were consistent with ones calculated from (4.5), and are used in this work.

The diffusion coefficient of SIA and mixed-dumbbell were directly calculated by (4.5) [HGZ17]. The diffusion coefficients used in this work are listed in Table (4.2).

Table 4.2: Diffusion coefficients.

Species	Pre-factor $[cm^2 \cdot s^{-1}]$	Activation energy [eV]
Pure SIA/cluster	$2.752 \times 10^{-3} \times (\sqrt{N_{SIA}})^{-1}$	0.003
Single mixed-dumbbell	1.498×10^{-3}	0.12
Pure vacancy/cluster	$3.387 \times 10^{-3} \times 0.001^{(N_V - 1)}$	1.623
Single Re atom	2.709×10^{-2}	4.79

4.1.2.3 Dissociation energy

The dissociation energy is defined as the energy difference between the system of a cluster to the one when a monomer is emitted and separated apart from the cluster. The dissociation energy of pure SIA and vacancy clusters has been set up and discussed in previous studies [MB11, MH12], which is used in this work.

The dissociation energy of a Re atom from a pure Re cluster is calculated as the system energy after moving a Re atom out from the cluster to infinity, subtracting the system energy before the dissociation. In previous kMC work, we have obtained several large clusters with the solute concentration roughly equal to 50at%. To compute the dissociation energy, Re atoms were moved one by one from the surface of a big cluster to a place where no bond connection with other Re atoms. The Re atoms in the cluster were extracted in the order of the distance to the center of mass of the cluster. The dissociation energy were fitted to a linear relation and the results are shown in Fig. (4.2). The fitted dissociation energy E_{diss}^{Re} as a function of number of Re atoms in the cluster N_{Re} is given as:

$$E_{diss}^{Re} = -0.0258 + 4.736 \times 10^{-6} N_{Re} \tag{4.7}$$

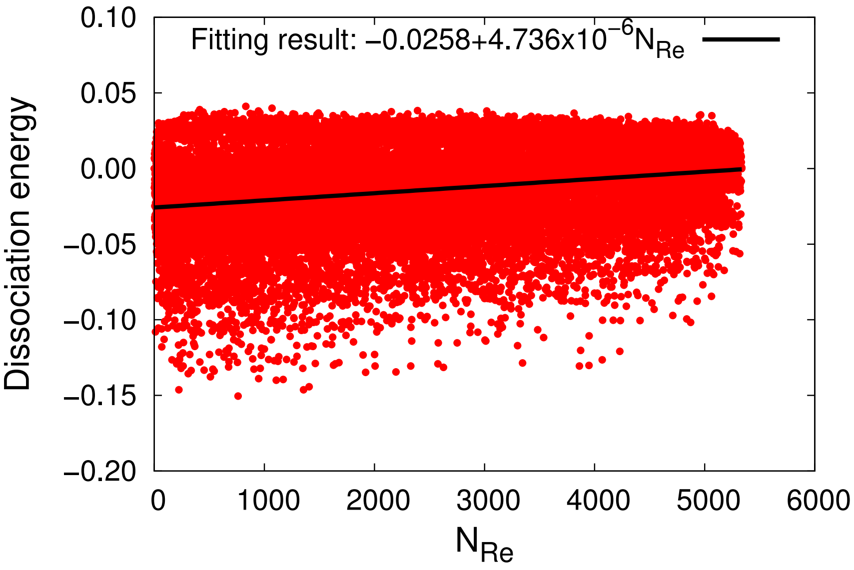

Figure 4.2: The dissociation energy of a Re atom from a pure Re cluster as a function of N_{Re} in the cluster.

It can be noted that E_{diss}^{Re} is negative, which means a pure Re cluster is not preferred and would dissociate with time.

To obtain the dissociation energy of vacancy-Re clusters, we performed Metropolis Monte Carlo simulations for V_mRe_n clusters with m= 1, 2, 3, ..., 8. For each amount of number of vacancies m, several simulations were run with different values of n (until the maximum possible number of n that a complete cluster can form), and dissociation energies of a vacancy and a Re atom were computed. The dissociation energy of a Re atom is dependent only on the ratio of the numbers of Re atoms to vacancies, whereas the dissociation energy of a vacancy is a function of both the numbers of Re atoms and vacancies in the cluster. Fig. (4.3) show the results of dissociation energies of a Re atom and a vacancy. The fitted functions are given as:

$$E_{diss}^{V_m Re_n}(Re) = 0.079 + 0.154\frac{m}{n} \tag{4.8}$$

$$E_{diss}^{V_m Re_n}(V) = 0.494 - 0.157m + 0.077n - 0.003mn + 0.015m^2 - 0.001n^2 \tag{4.9}$$

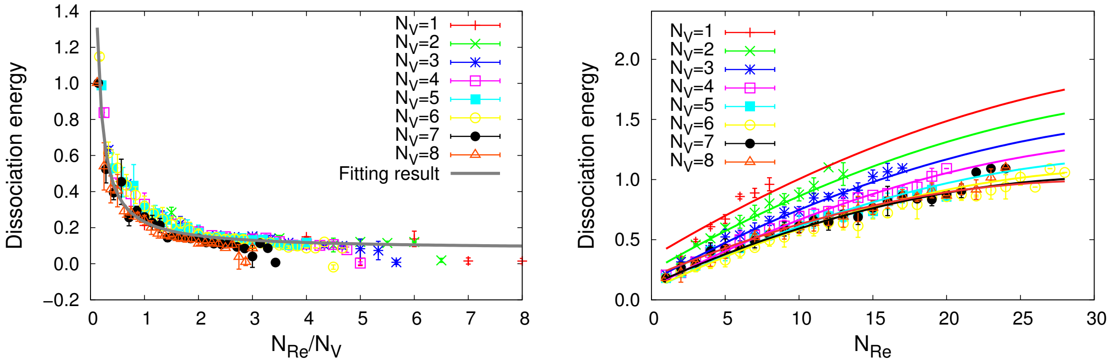

(a) (b)

Figure 4.3: The dissociation energy of (a) Re atom and (b) vacancy from a V-Re cluster as a function of ratio of N_{Re}/N_V and N_V, respectively.

4.2 Results

We perform 15 simulations for DEMO, HFIR, and JOYO reactors, each with five temperatures: 673, 773, 873, 973, and 1073 K. The system volume is set to be $10^{-20}m^3$. The dpa rate is set to be 2.4×10^{-07}, which is the same as experimental value in Ref. [XBA15,XAB17] for the purpose of comparison. The simulations are run for 2.4 dpa. The time evolution of clusters containing different amounts of SIAs, vacancies, and Re atoms are recorded during simulations for later analysis.

4.2.1 Cluster size distribution and density

We first calculate the cluster size distribution. A cluster is classified as a SIA loop if the cluster contains more SIAs than solute atoms; it belongs to a void if it contains more vacancies than solute atoms; in all other cases, it is considered as a solute precipitate. The diameter of the cluster is calculated by assuming a sphere for voids and precipitates, and a circle disk with thickness of one burger's vector for SIA loops. The size distributions of SIA loops, voids, and precipitates at 0.5, 1.0, and 2.0 dpa for DEMO, HFIR, and JOYO reactors are shown in Fig. (4.4), (4.5), and (4.6), respectively. It can be seen that at elevated temperatures vacancies/voids dissapear in the systems due to the higher mobility of vacancies, which have higher chance to be ended at sinks or recombinations. SIA loops, on the other hand, remain in the systems due to the strong binding energy to Re atoms.

The number density of clusters (with monomer excluded) at 673 K as a function of dpa is shown in Fig. (4.7). Experimentally, there is a limit resolution of 1nm when observing clusters. In Fig. (4.8), (4.9), and (4.10), we show the number density evolution for the three reactors with clusters diameter larger than 1nm. It can be clearly seen that for HFIR there are only visible clusters at 673 K and therefore in the following hardening calculation we only present results of HFIR at 673 K.

4.2.2 Irradiation hardening due to formation of clusters

The estimation of the hardening effects due to clusters have been studied and a dispersed barrier hardening model has been developed by Friedel-Kroupa-Hirsh [KH64, ZM04]. In this work, we perform a comparison of our simulation results with a recent experimental study done by Hu and his co-workers [HKF16]. In their study, the change in yield strength σ_y is

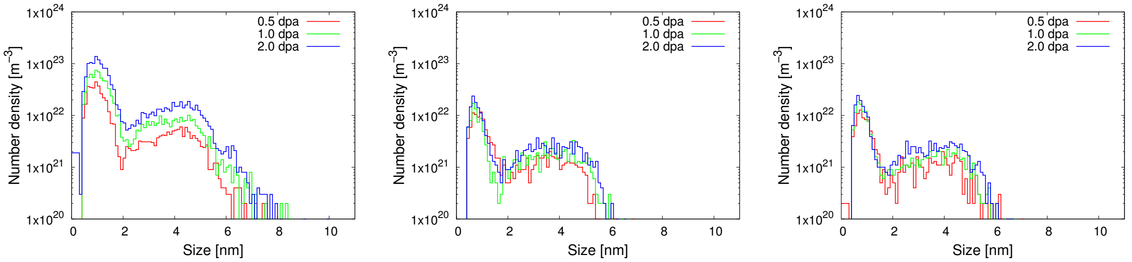

(a) SIA loops at 673 K. (b) SIA loops at 873 K. (c) SIA loops at 1073 K.

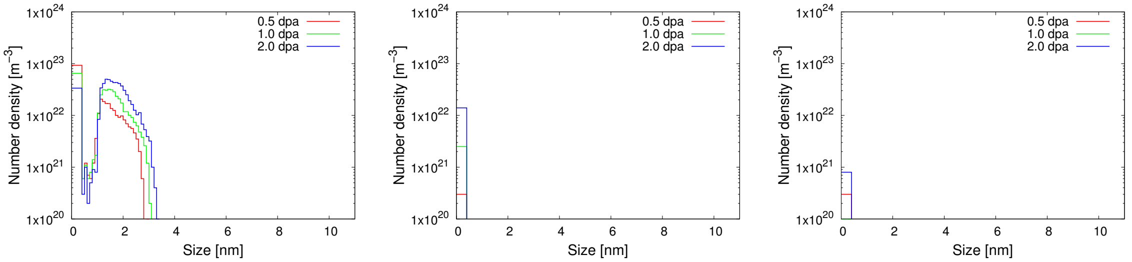

(d) Voids at 673 K. (e) Voids at 873 K. (f) Voids at 1073 K.

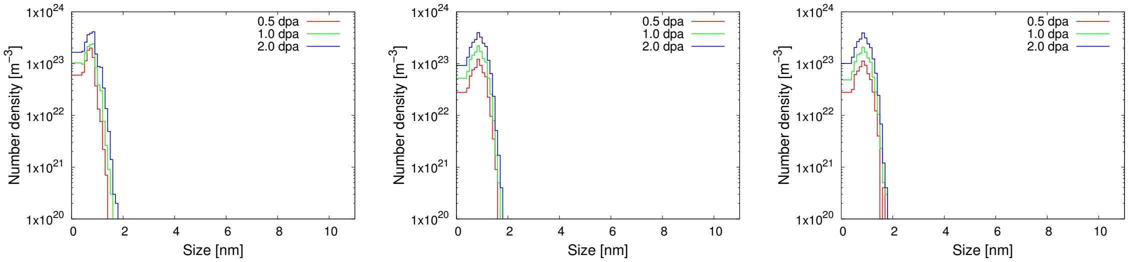

(g) Re precipitates at 673 K. (h) Re precipitates at 873 K. (i) Re precipitates at 1073 K.

Figure 4.4: The cluster size distributions of SIA loops, voids, and Re precipitates for DEMO irradiations.

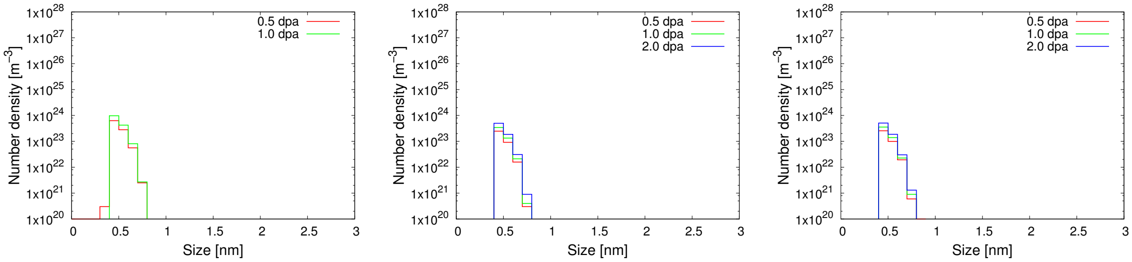

(a) SIA loops at 673 K. (b) SIA loops at 873 K. (c) SIA loops at 1073 K.

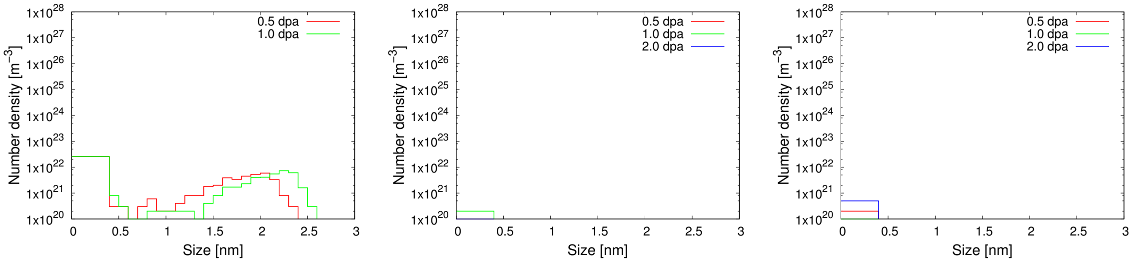

(d) Voids at 673 K. (e) Voids at 873 K. (f) Voids at 1073 K.

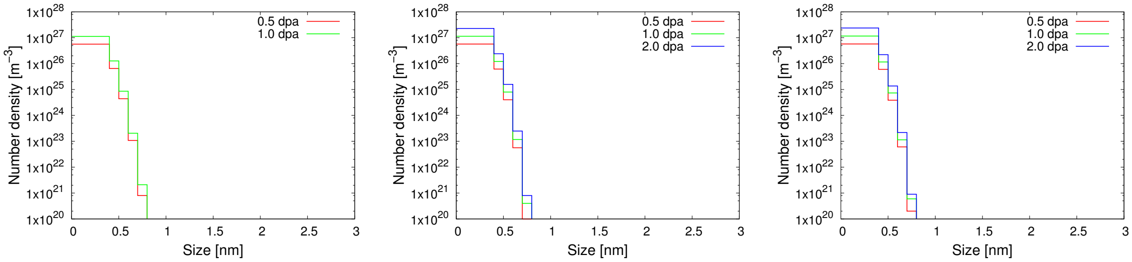

(g) Re precipitates at 673 K. (h) Re precipitates at 873 K. (i) Re precipitates at 1073 K.

Figure 4.5: The cluster size distributions of SIA loops, voids, and Re precipitates for HFIR irradiations.

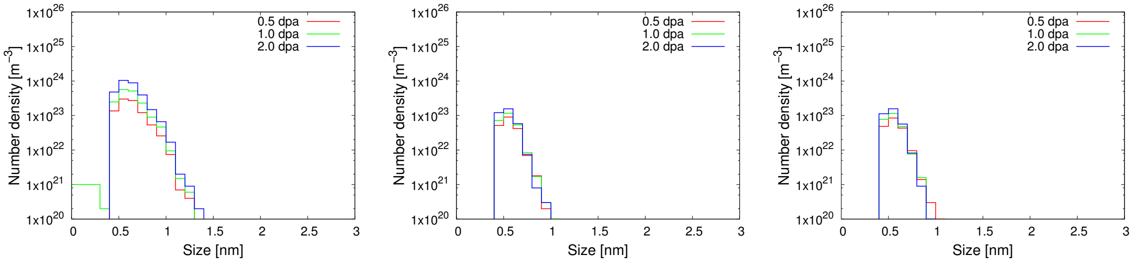

(a) SIA loops at 673 K. (b) SIA loops at 873 K. (c) SIA loops at 1073 K.

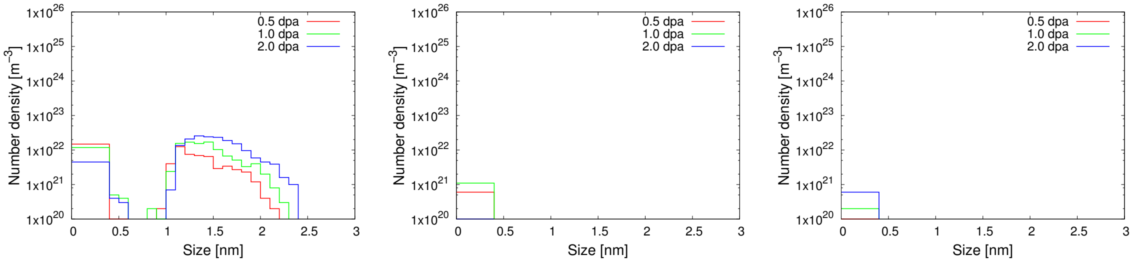

(d) Voids at 673 K. (e) Voids at 873 K. (f) Voids at 1073 K.

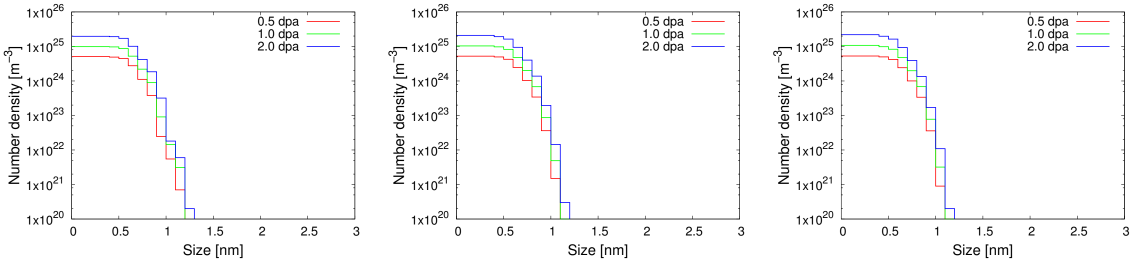

(g) Re precipitates at 673 K. (h) Re precipitates at 873 K. (i) Re precipitates at 1073 K.

Figure 4.6: The cluster size distributions of SIA loops, voids, and Re precipitates for JOYO irradiations.

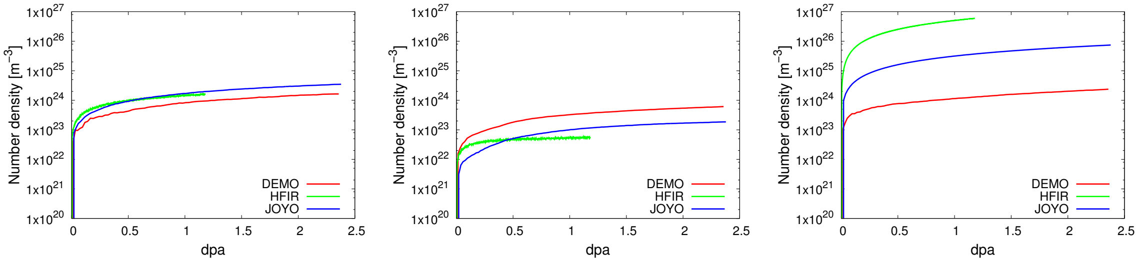

(a) SIA loops. (b) Voids. (c) Re precipitates.

Figure 4.7: Accumulation of all SIA loops, voids, and Re precipitates clusters as a function of dose at different temperatures for DEMO, HFIR, and JOYO irradiations.

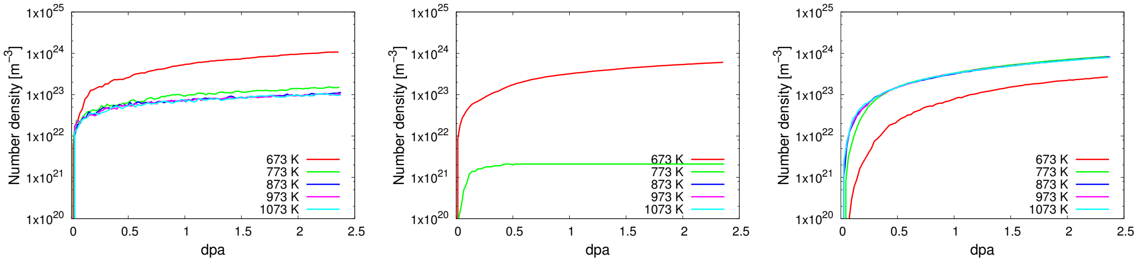

(a) SIA loops.

(b) Voids.

(c) Re precipitates.

Figure 4.8: Accumulation of visible SIA loops, voids, and Re precipitates as a function of dose at different temperatures for DEMO irradiations.

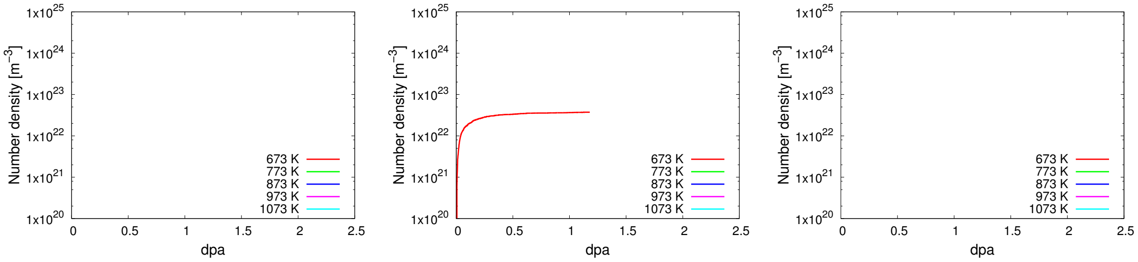

(a) SIA loops.

(b) Voids.

(c) Re precipitates.

Figure 4.9: Accumulation of visible SIA loops, voids, and Re precipitates as a function of dose at different temperatures for HFIR irradiations.

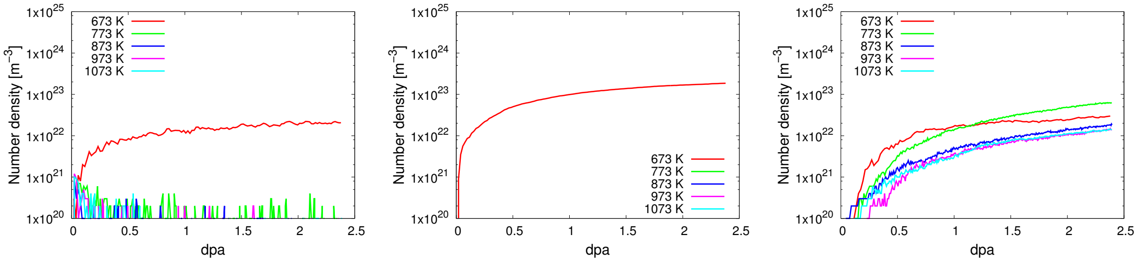

(a) SIA loops.

(b) Voids.

(c) Re precipitates.

Figure 4.10: Accumulation of visible (>1.0 nm) SIA loops, voids, and Re precipitates as a function of dose at different temperatures for JOYO irradiations.

formulated as:

$$\sigma_y = 3.2M\alpha\mu b(Nd)^{\frac{1}{2}} \tag{4.10}$$

where M is the Taylor factor, α is the defect cluster barrier strength, μ is the shear modulus of the tungsten matrix, b is the magnitude of the dislocation Burgers vector, N is the number density. Followed by the work of Hu et al. [HKF16], the values of Taylor factor M, shear modulus μ were set to be 3.06, 161 Gpa, respectively, and Burgers vector is given as $\bar{b} = \frac{a}{2} < 111 >$. The defect cluster barrier strength α is different for different defect clusters: voids and precipitates are considered as strong obstacles and therefore have relatively high values of α. The values of α are listed in Table (4.3). In this calculation, only the contribution of visible clusters (with diameter larger than 1.0 nm) is taken into account.

Table 4.3: The defect cluster barrier strength α for different types and diameter of clusters. The values were obtained from the work of Hu et al. [HKF16].

Defects	size	barrier strength factor (α)
Dislocation loops	>1.0 nm	0.15
Voids	1-2 nm	0.25
Voids	2-3 nm	0.30
Voids	3-4 nm	0.35
Voids	>4 nm	0.40
Precipitates	>1.0 nm	0.60

Fig. (4.11) shows the simulation results of irradiation hardening contribution from different clusters calculated using Eq. (4.10). As the dose increases, the hardness increases as more damages are inserted into the systems. Hardening is dependent on temperature. At low temperature, vacancy mobility is very small, making vacancies/voids hard to reach at sinks. In this case, voids are the major obstacles to contribute to hardening. At high temperature, voids are dissipated and Re precipitates become the main contributor of hardening. The hardness increases obtained in this simulation work are partially consistent with the experimental data such as JOYO at low temperatures. However, some inconsistencies are also observed. In the experimental work, The major contributor changes from SIA loops and voids to Re precipitates as dose increase, which cannot observe in our simulation results. Also, the contribution from Re precipitates for HFIR does not appear in the results, despite the high transmutation rates.

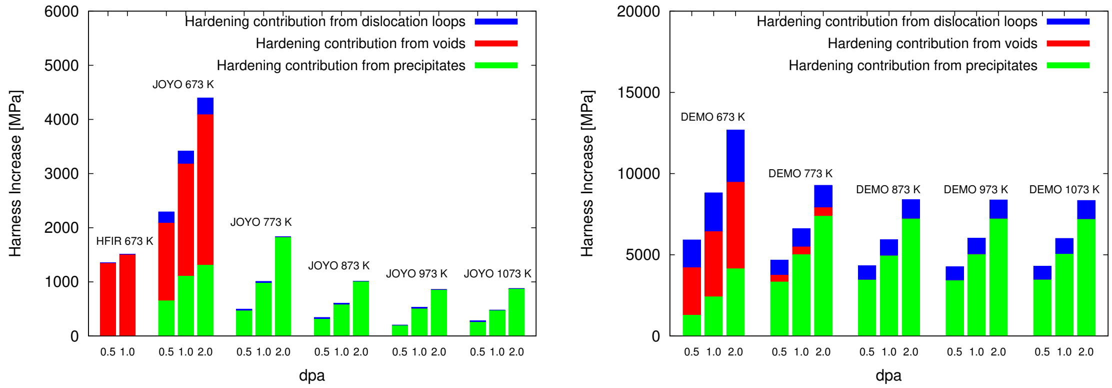

(a) HFIR and JOYO.

(b) DEMO.

Figure 4.11: Radiation-induced hardening contributions from different clusters calculated using Eq. (4.10) for (a) HFIR, JOYO and (b) DEMO reactors. For HFIR reactor, there are visible clusters only at temperature of 673 K and hardening at other temperatures is omitted.

APPENDIX A

A.1 Details in diffusion coefficient calculations

During the diffusion simulations, we tracked the positions of the vacancy and solute atoms, and calculated the mean square displacements by $\langle \Delta r^2 \rangle = n^{-1} \sum_{a=1}^{n} r_a^2$, where $n = 1, n_B$ for the vacancy and solute atoms, respectively. Fig. (A.1) shows an example of $\langle \Delta r^2 \rangle$ as a function of time for solute atom diffusions at 900 K at different solute concentrations. A linear relation between $\langle \Delta r^2 \rangle$ and time can be observed. 100 data points are then selected with equal time period and diffusion coefficients are obtained by fitting the data points to the *Einstein*'s equation:

$$D = \frac{\langle \Delta r^2 \rangle}{6\Delta t} \tag{A.1}$$

Transport coefficients are calculated with the same method, with the dot product $\langle \Delta r_i \Delta r_j \rangle$ computed as $\left(\sum_{a=1}^{n} r_a\right)\left(\sum_{b=1}^{n} r_b\right)$.

A.2 Size dependence of physical time in kMC simulations

As explained in Section 3.3, the mechanism of formation of Re clusters requires the concerted action of both interstitials and vacancies. In order to be able to capture their formation during reasonable computational times, the temperature regime considered must be one

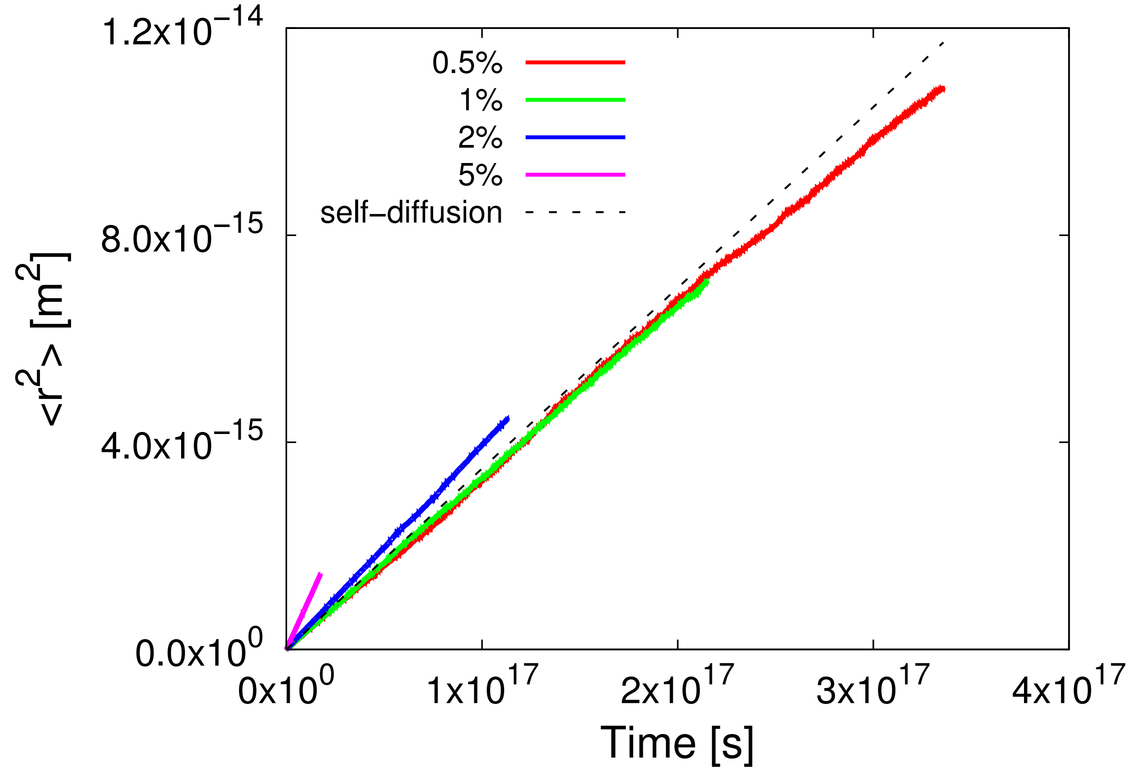

Figure A.1: Mean square displacements of solute atoms $\langle r^2 \rangle$ as a function of time at 900 K for different solute concentrations.

where the mobility of both species is comparable (1700 $\sim$ 2000 K in our case). Then, the rate of arrival of solute atoms to a previously-nucleated Re cluster can be approximated by:

$$r_s = \frac{1}{t_{\mathrm{FP}} + t_{diff}} \tag{A.2}$$

where t_{FP} and t_{diff} are the average time in between successive Frenkel-pair insertions and a characteristic diffusion time required by a vacancy and an interstitial to recombine with one another. r_s is measured in units of atoms per unit time. At the temperatures and dose rates considered here, $t_{\mathrm{FP}} \gg t_{diff}$, such that $r_s \approx {t_{\mathrm{FP}}}^{-1}$. Assuming then that for each Frenkel pair inserted a minimum of one solute atom is transported:

$$r_s = \frac{dN_B}{dt} = r_{\mathrm{dpa}} N \tag{A.3}$$

where N_B is the total number of solute atoms in the precipitate. r_{dpa} in the above equation is the damage rate, expressed in units of [dpa$\cdot$s^{-1}]. The precipitate volume growth rate is directly equal to the atomic volume times r_s:

$$\dot{V}_{\text{ppt}} = \Omega_a r_s = \Omega_a \frac{dN_B}{dt} = \Omega_a r_{\text{dpa}} N \tag{A.4}$$

Assuming that the precipitate is close to spherical:

$$\dot{V}_{\text{ppt}} = 4\pi {R_{\text{ppt}}}^2 \dot{R}_{\text{ppt}} = \Omega_a r_{\text{dpa}} N$$

And, operating, we arrive at the equation for the evolution of the precipitate radius with time:

$$R_{\text{ppt}} = \left(\frac{\Omega_a r_{\text{dpa}} N t}{4\pi} \right)^{\frac{1}{3}} \tag{A.5}$$

which is the equation used for fitting in Fig. 3.11.

Then, from eq. (A.3), for a given constant dpa rate, it is clear that the ratio $r_s(V_1)N_1^{-1} = r_s(V_2)N_2^{-1} =$ constant, where V_1 and V_2 are two different box sizes. For as long as the approximation in eq. (A.2) is valid, then:

$$t_{\text{FP}}^{(1)} N_1 = t_{\text{FP}}^{(2)} N_2 = \text{ constant}$$

which allows us to compare simulations done on box sizes of 64^3 and 80^3 directly. We emphasize that at lower temperatures, and/or high dose rate, where $t_{\text{FP}} \approx t_{diff}$, this comparison is no longer valid.

A.3 Cluster size distribution

The cluster distribution evolution in a KMC simulation with no sink is shown in Fig. (A.2). It demonstrates the transition of the cluster distribution while the big precipitate sucks solute atoms from the small clusters.

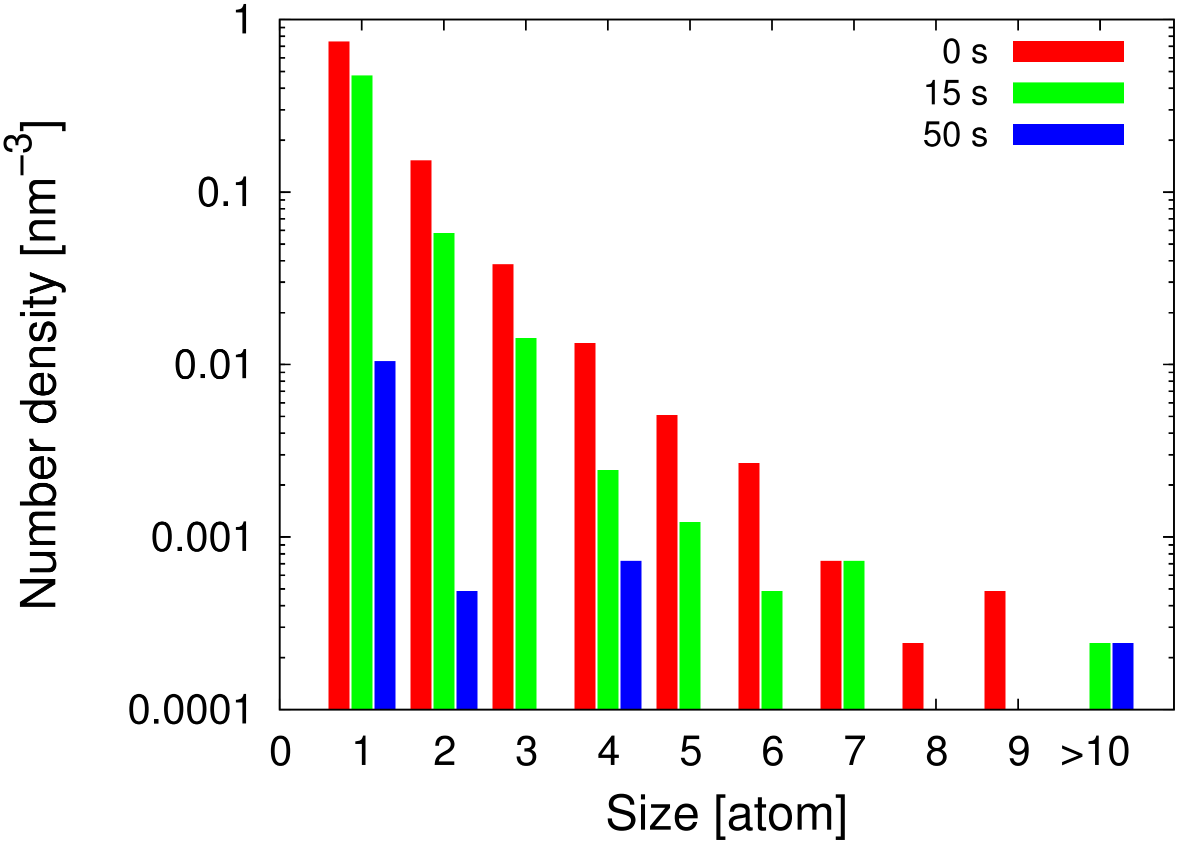

Figure A.2: The histogram plot of solute cluster distribution at 0s (beginning), 15s (growing), and 50s (end). The KMC simulations are performed at 2.0% solute concentration at 2000 K.

A.4 Confirmation of SRO preference of vacancies

As discussed in the main text, a vacancy acts as a mediator for solute atoms to form small cluster (dimer, trimer, etc.) when the W-Re alloy is in random-solution state, but changes its roll to dissolve precipitates when the precipitate grows larger. We performed KMC simulations with only 1 vacancy to confirm the hypothesis. The vacancy was initially added to the system and no other defect was generated during simulations. Two initial configurations were used: random solution and complete precipitation with all solute atoms in a big cubic. The SRO is then computed and compared. The simulations were performed at 2.0% solute concentration at 1800 K, with box size of 64^3. The results of SRO evolution can be seen in Fig. (A.3). It can be seen that SRO with initial configurations of full precipitation and random solid solution converges from a value of roughly 1.0, 0.0, respectively, to a value close to 10^{-3}.

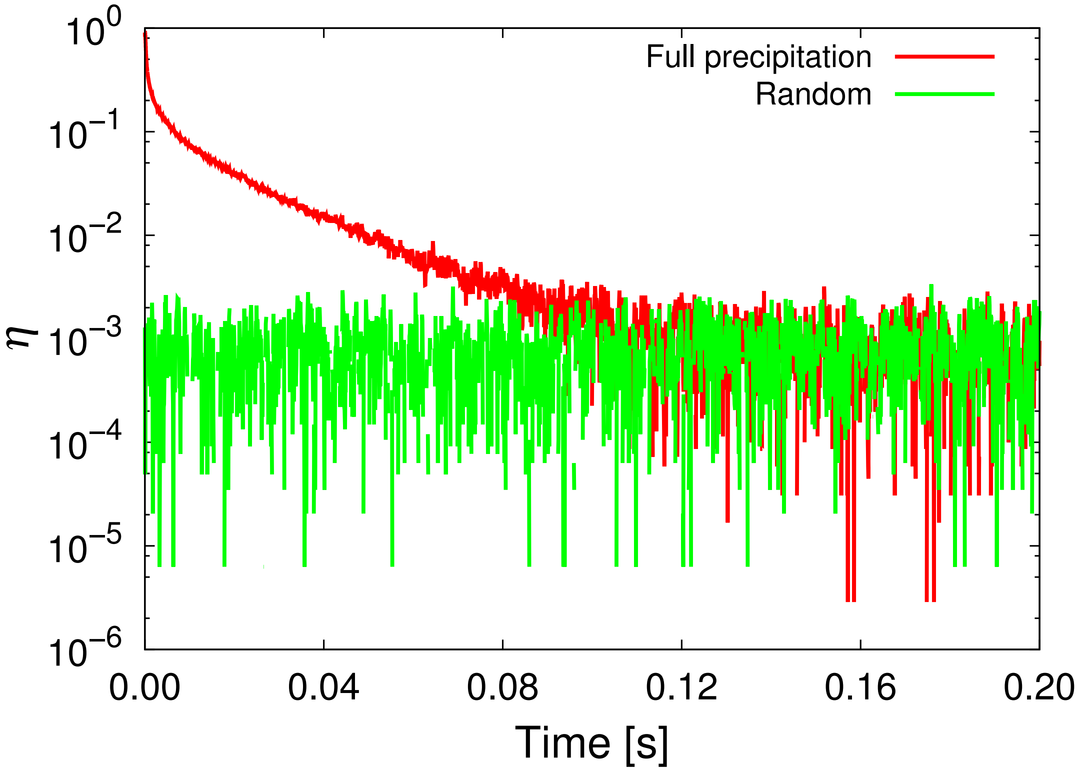

Figure A.3: SRO evolution with initial configurations of full precipitation and random solid solution. The KMC simulations are performed at 2.0% solute concentration at 1800 K.

A.5 KMC simulations with sinks

As discussed in the theory and methods section, there are two sink conditions used in this work: plane sink and surface sink. We performed KMC simulations on an 64^3 W-2.0% at. Re alloy at 1800 K. The concentration profiles for the two sink conditions along x-dimension are shown in Fig. (A.4). The enrichment of solute atoms can be clearly seen at the middle and two sides of the system for plane sink and surface sink conditions, respectively. As discussed in the main text, mixed-interstitial is the major solute atom carrier to the sinks. Vacancy, on the other hand, may disperse solute atoms to surrounding regions nearby sinks.

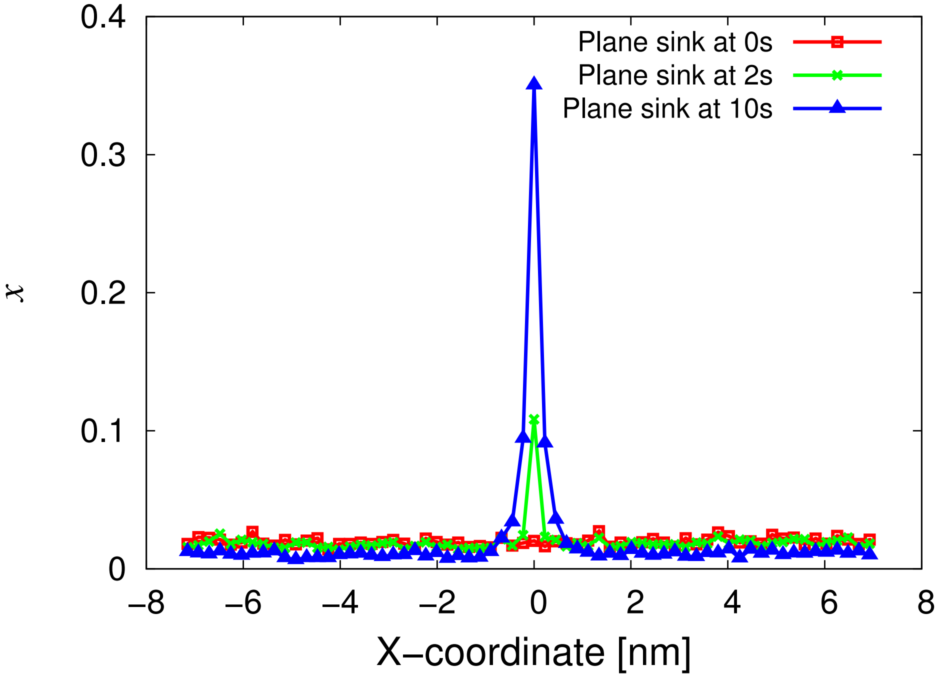

(a)

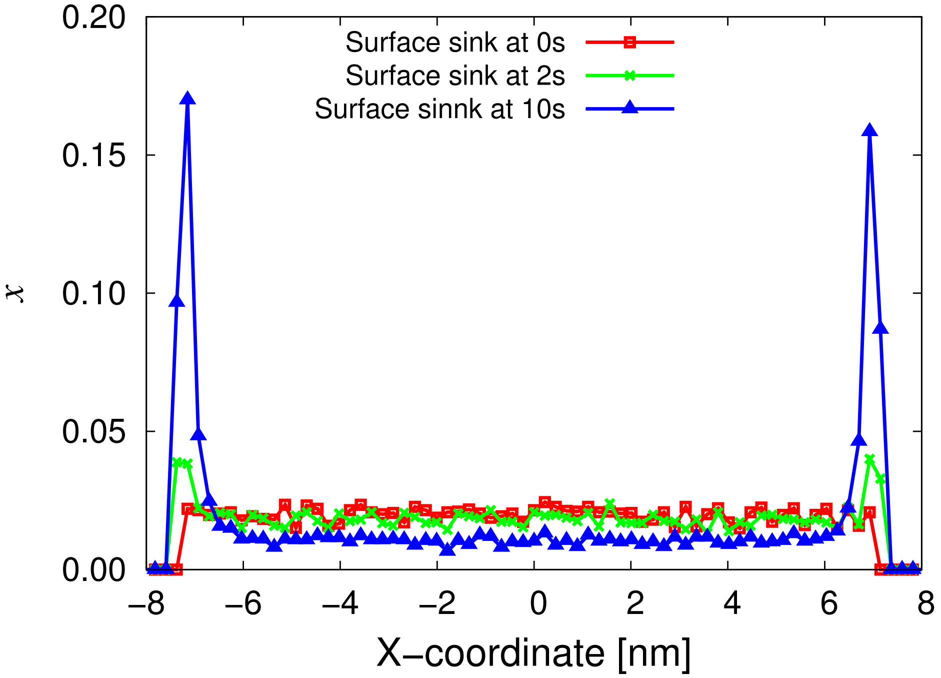

(b)

Figure A.4: Solute concentration profile along x-dimension for simulations in (a) plane sink and (a) surface sink conditions. The KMC simulations were performed at 2.0% solute concentration at 1500 K.

References

[AL03] A.R. Allnatt and A.B. Lidiard. *Atomic Transport in Solids*. Cambridge University Press, 2003.

[BD07] C.S. Becquart and C. Domain. “Ab initio calculations about intrinsic point defects and He in W.” *Nuclear Instruments and Methods in Physics Research Section B: Beam Interactions with Materials and Atoms*, **255**(1):23 – 26, 2007. Computer Simulation of Radiation Effects in SolidsProceedings of the Eighth International Conference on Computer Simulation of Radiation Effects in Solids (COSIRES 2006)Computer Simulation of Radiation Effects in Solids.

[BD09] C. S. Becquart and C. Domain. “An object Kinetic Monte Carlo Simulation of the dynamics of helium and point defects in tungsten.” *J. Nucl. Mater.*, **385**(2):223–227, March 2009.

[BDS10] C.S. Becquart, C. Domain, U. Sarkar, A. DeBacker, and M. Hou. “Microstructural evolution of irradiated tungsten: Ab initio parameterisation of an {OKMC} model.” *Journal of Nuclear Materials*, **403**(1–3):75 – 88, 2010.

[Bl94] P. E. Blöchl. “Projector augmented-wave method.” *Phys. Rev. B*, **50**(24):17953 –17979, 1994.

[BLP81] Kurt Binder, Joel L. Lebowitz, Mohan K. Phani, and Malvin H. Kalos. “Monte carlo study of the phase diagrams of binary alloys with face centered cubic lattice structure.” *Acta Metallurgica*, **29**(9):1655, 1981.

[BS02] Y. L. Bouar and F. Soisson. “Kinetic pathways from embedded-atom-method potentials: Influence of the activation barriers.” *Physical Review B*, **65**:094103, 2002.

[BW34] W. L. Bragg and E. J. Williams. “The Effect of Thermal Agitation on Atomic Arrangement in Alloys.” *Proceedings of the Royal Society of London A: Mathematical, Physical and Engineering Sciences*, **145**(855):699–730, 1934.

[BW35] W. L. Bragg and E. J. Williams. “The Effect of Thermal Agitation on Atomic Arrangement in Alloys. II.” *Proceedings of the Royal Society of London A: Mathematical, Physical and Engineering Sciences*, **151**(874):540–566, 1935.

[BZ04] V. Blum and A. Zunger. “Mixed-basis cluster expansion for thermodynamics of bcc alloys.” *Physical Review B*, **70**:155108, 2004.

[BZK10] A. Biborski, L. Zosiak, R. Kozubski, R. Sot, and V. Pierron-Bohnes. “Semi-grand canonical Monte Carlo simulation of ternary bcc lattice-gas decomposition: Vacancy formation correlated with {B2} atomic ordering in A–B intermetallics.” *Intermetallics*, **18**(12):2343 – 2352, 2010.

[Car08] Emily A Carter. "Challenges in modeling materials properties without experimental input." *Science*, **321**(5890):800–803, 2008.

[CL05] Luigi Cannavacciuolo and D. P. Landau. "Critical behavior of the three-dimensional compressible Ising antiferromagnet at constant volume: A Monte Carlo study." *Physical Review B*, **71**:134104, 2005.

[CM79] Richard Cauvin and Georges Martin. "Radiation induced homogeneous precipitation in undersaturated solid-solutions." *Journal of Nuclear Materials*, **83**(1):67 – 78, 1979.

[Cot04] GA Cottrell. "Sigma phase formation in irradiated tungsten, tantalum and molybdenum in a fusion power plant." *Journal of nuclear materials*, **334**(2):166–168, 2004.

[Cow50] J. M. Cowley. "An Approximate Theory of Order in Alloys." *Phys. Rev.*, **77**:669–675, Mar 1950.

[CPL13] Aleksandr Chernatynskiy, Simon R Phillpot, and Richard LeSar. "Uncertainty quantification in multiscale simulation of materials: A prospective." *Annual Review of Materials Research*, **43**:157–182, 2013.

[CS63] D. A. Chesnut and Z. W. Salsburg. "Monte Carlo Procedure for Statistical Mechanical Calculations in a Grand Canonical Ensemble of Lattice Systems." *The Journal of Chemical Physics*, **38**(12):2861–2875, 1963.

[DD58] George Julian Dienes and AC Damask. "Radiation enhanced diffusion in solids." *Journal of Applied Physics*, **29**(12):1713–1721, 1958.

[DDJ95] H. A. H. Duparc, R. C. Doole, M. L. Jenkins, and A. Barbu. "A high-resolution electron microscopy study of copper precipitation in Fe-1.5 wt% Cu under electron irradiation." *Philosophical Magazine Letters*, **71**(6):325–333, 1995.

[DE15] S. Dubey and A. El-Azab. "A defect-based model of radiation-induced segregation to free surfaces in binary alloys." *Computational Materials Science*, **106**:111–122, 2015.

[DL93] B. Dunweg and D. P. Landau. "Phase diagram and critical behavior of the Si-Ge unmixing transition: A Monte Carlo study of a model with elastic degrees of freedom." *Physical Review B*, **48**:14182, 1993.

[DMD07] F. G. Djurabekova, L. Malerba, C. Domain, and C. S. Becquart. "Stability and mobility of small vacancy and copper-vacancy clusters in bcc-Fe: An atomistic kinetic Monte Carlo study." *Nuclear Instruments and Methods in Physics Research Section B: Beam Interactions with Materials and Atoms*, **255**(1):47–51, 2007.

[EB01] R. A. Enrique and P. Bellon. "Compositional patterning in immiscible alloys driven by irradiation." *Physical Review B*, **63**(13), 2001.

[EMS13] Paul Erhart, Jaime Marian, and Babak Sadigh. “Thermodynamic and mechanical properties of copper precipitates in alpha-iron from atomistic simulations.” *Phys. Rev. B*, **88**(2):024116, July 2013.

[ENA03] R. A. Enrique, K. Nordlund, R. S. Averback, and P. Bellon. “Simulations of dynamical stabilization of Ag-Cu nanocomposites by ion-beam processing.” *Journal of Applied Physics*, **93**(5):2917, 2003.

[EPG00] M. Ekman, K. Persson, and G. Grimvall. “Phase diagram and lattice instability in tungsten-rhenium alloys.” *Journal of Nuclear Materials*, **278**(2-3):273–276, 2000.

[EXH15] Philip D Edmondson, Alan Xu, Luke R Hanna, Michal Dagan, Steve G Roberts, and Lance L Snead. “Atomic Scale, 3-Dimensional Characterization of Radiation Effects in Tungsten for Fusion Applications.” *Microscopy and Microanalysis*, **21**(S3):579–580, 2015.

[FN08] S. P. Fitzgerald and D. Nguyen-Manh. “Peierls Potential for Crowdions in the bcc Transition Metals.” *Phys. Rev. Lett.*, **101**:115504, 2008.

[FPW00] P. Fratzl, O. Penrose, R. Weinkamer, and I. Žižak. “Coarsening in the Ising model with vacancy dynamics.” *Physica A: Statistical Mechanics and its Applications*, **279**(1-4):100–109, 2000.

[FVP93] C. Frontera, E. Vives, and A. Planes. “Monte Carlo study of the relation between vacancy diffusion and domain growth in two-dimensional binary alloys.” *Physical Review B*, **48**(13):9321–9326, 1993.

[Gas08] D. R. Gaskell. *Introduction to the Thermodynamics of Materials, Fifth Edition*. CRC Press, 2008.

[GDD08] M R Gilbert, S L Dudarev, P M Derlet, and D G Pettifor. “Structure and metastability of mesoscopic vacancy and interstitial loop defects in iron and tungsten.” *Journal of Physics: Condensed Matter*, **20**(34):345214, 2008.

[GDZ12] M. R. Gilbert, S. L. Dudarev, S. Zheng, L. W. Packer, and J.-Ch Sublet. “An integrated model for materials in a fusion power plant: transmutation, gas production, and helium embrittlement under neutron irradiation.” *Nuclear Fusion*, **52**(8):083019, 2012.

[GE15] L. Gharaee and P. Erhart. “A first-principles investigation of interstitial defects in dilute tungsten alloys.” *Journal of Nuclear Materials*, **467, Part 1**:448–456, 2015.

[GME16] Leili Gharaee, Jaime Marian, and Paul Erhart. “The role of interstitial binding in radiation induced segregation in W-Re alloys.” *Journal of Applied Physics*, **120**(2), 2016.

[GMM01] D. Gendt, P. Maugis, G. Martin, M. Nastar, and F. Soisson. "Monte Carlo Simulation of NbC Precipitation Kinetics in α-Fe." In *Diffusion in Materials DIMAT2000*, volume 194 of *Defect and Diffusion Forum*, pp. 1779–1786. Trans Tech Publications, 2001.

[GS11] M. R. Gilbert and J.-Ch Sublet. "Neutron-induced transmutation effects in W and W-alloys in a fusion environment." *Nuclear Fusion*, **51**(4):043005, 2011.

[Han11] Felix Hanke. "Sensitivity analysis and uncertainty calculation for dispersion corrected density functional theory." *Journal of computational chemistry*, **32**(7):1424–1430, 2011.

[HDC10] Céline Hin, Mildred Dresselhaus, and Gang Chen. "Vacancy clustering and diffusion in heavily P doped Si." *Applied Physics Letters*, **97**(25), 2010.

[HGZ17] Chen-Hsi Huang, Leili Gharaee, Yue Zhao, Paul Erhart, and Jaime Marian. "Mechanism of Re precipitation in irradiated W-Re alloys from kinetic Monte Carlo simulations." *arXiv*, **1702**:03019, 2017.

[Hin09] C. Hin. "Kinetics of heterogeneous grain boundary precipitation of Ni 3 Al in nickel alloy." *Journal of Physics D: Applied Physics*, **42**(22):225309, 2009.

[HIS95] T. Hashimoto, Y. Isobe, and N. Shigenaka. "A model for radiation-induced segregation in fcc binary alloys." *Journal of Nuclear Materials*, **225**:108–116, 1995.

[HKF16] Xunxiang Hu, Takaaki Koyanagi, Makoto Fukuda, N.A.P. Kiran Kumar, Lance L. Snead, Brian D. Wirth, and Yutai Katoh. "Irradiation hardening of pure tungsten exposed to neutron irradiation." *Journal of Nuclear Materials*, **480**:235 – 243, 2016.

[HKK15] X Hu, T Koyanagi, Y Katoh, M Fukuda, B D Wirth, and L L Snead. "Defect Evolution in Neutron-Irradiated Single Crystalline Tungsten.", 2015. DOE/ER-0313/58-Semiannual Progress Report, June 30, 2015.

[HM16] Chen-Hsi Huang and Jaime Marian. "A generalized Ising model for studying alloy evolution under irradiation and its use in kinetic Monte Carlo simulations." *Journal of Physics: Condensed Matter*, **28**(42):425201, 2016.

[HS84] R Herschitz and DN Seidman. "An atomic resolution study of radiation-induced precipitation and solute segregation effects in a neutron-irradiated W-25 at.% Re alloy." *Acta Metallurgica*, **32**(8):1155–1171, 1984.

[HS85] Roman Herschitz and David N Seidman. "Radiation-induced precipitation in fast-neutron irradiated tungsten-rhenium alloys: An atom-probe field-ion microscope study." *Nuclear Instruments and Methods in Physics Research Section B: Beam Interactions with Materials and Atoms*, **7**:137–142, 1985.

[HTH06] JC He, GY Tang, A Hasegawa, and K Abe. "Microstructural development and irradiation hardening of W and W–(3–26) wt% Re alloys after high-temperature neutron irradiation to 0.15 dpa." *Nuclear fusion*, **46**(11):877, 2006.

[HTN11] Akira Hasegawa, Takashi Tanno, Shuhei Nogami, and Manabu Satou. “Property change mechanism in tungsten under neutron irradiation in various reactors.” *J. Nucl. Mater.*, **417**(1–3):491–494, October 2011.

[HUJ00] Graeme Henkelman, Blas P. Uberuaga, and Hannes Jónsson. “A climbing image nudged elastic band method for finding saddle points and minimum energy paths.” *J. Chem. Phys.*, **113**(22):9901–9904, 2000.

[HWN09] C. Hin, B. D. Wirth, and J. B. Neaton. “Formation of Y_2O_3 nanoclusters in nanostructured ferritic alloys during isothermal and anisothermal heat treatment: A kinetic Monte Carlo study.” *Phys. Rev. B*, **80**:134118, 2009.

[KAB07] P. Krasnochtchekov, R. S. Averback, and P. Bellon. “Homogeneous phase separation in binary alloys under ion irradiation conditions: Role of interstitial atoms.” *Physical Review B*, **75**(14), 2007.

[KF96a] G. Kresse and J. Furthmüller. “Efficiency of ab-initio total energy calculations for metals and semiconductors using a plane-wave basis set.” *Comput. Mater. Sci.*, **6**(1):15–50, 1996.

[KF96b] G. Kresse and J. Furthmüller. “Efficient iterative schemes for ab initio total-energy calculations using a plane-wave basis set.” *Phys. Rev. B*, **54**:11169, 1996.

[KH64] F. Kroupa and P.B. Hirsch. “Elastic interaction between prismatic dislocation loops and straight dislocations.” *Discussions of the Faraday Society*, **38**:49 – 55, 1964.

[KH93] G. Kresse and J. Hafner. “Ab initio molecular dynamics for liquid metals.” *Phys. Rev. B*, **47**(1):558–561, 1993.

[KH94] G. Kresse and J. Hafner. “Ab initio molecular-dynamics simulation of the liquid-metal–amorphous-semiconductor transition in germanium.” *Phys. Rev. B*, **49**(20):14251, 1994.

[KIM11] Daiji Kato, Hirotomo Iwakiri, and Kazunori Morishita. “Formation of vacancy clusters in tungsten crystals under hydrogen-rich condition.” *Journal of Nuclear Materials*, **417**(1):1115–1118, 2011.

[KJ99] G. Kresse and D. Joubert. “From ultrasoft pseudopotentials to the projector augmented-wave method.” *Phys. Rev. B*, **59**(3):1758 – 1775, 1999.

[KJR16] M. Klimenkov, U. Jntsch, M. Rieth, H.C. Schneider, D.E.J. Armstrong, J. Gibson, and S.G. Roberts. “Effect of neutron irradiation on the microstructure of tungsten.” *Nuclear Materials and Energy*, pp. –, 2016.

[LFF92] D. B. Laks, L. G. Ferreira, S. Froyen, and A. Zunger. “Efficient cluster expansion for substitutional systems.” *Physical Review B*, **46**:12587–12605, 1992.

[MB11] Jaime Marian and Vasily V. Bulatov. "Stochastic cluster dynamics method for simulations of multispecies irradiation damage accumulation." *Journal of Nuclear Materials*, **415**(1):84 – 95, 2011.

[MGL01] P. Maugis, D. Gendt, S. Lanteri, and P. Barges. "Modeling of Niobium Carbide Precipitation in Steel." In *Diffusion in Materials DIMAT2000*, volume 194 of *Defect and Diffusion Forum*, pp. 1767–1772. Trans Tech Publications, 2001.

[MH12] Jaime Marian and Tuan L. Hoang. "Modeling fast neutron irradiation damage accumulation in tungsten." *Journal of Nuclear Materials*, **429**(1–3):293 – 297, 2012.

[MNK11] M. Muzyk, D. Nguyen-Manh, K. J. Kurzydłowski, N. L. Baluc, and S. L. Dudarev. "Phase stability, point defects, and elastic properties of W-V and W-Ta alloys." *Phys. Rev. B*, **84**:104115, Sep 2011.

[MNM74] J. Matolich, H. Nahm, and J. Moteff. "Swelling in neutron irradiated tungsten and tungsten-25 percent rhenium." *Scripta Metallurgica*, **8**(7):837 – 841, 1974.

[MSF12] E. Martínez, O. Senninger, C. Fu, and F. Soisson. "Decomposition kinetics of Fe-Cr solid solutions during thermal aging." *Physical Review B*, **86**:224109, 2012.

[MSH15] JD McDonnell, N Schunck, D Higdon, J Sarich, SM Wild, and W Nazarewicz. "Uncertainty quantification for nuclear density functional theory and information content of new measurements." *Physical review letters*, **114**(12):122501, 2015.

[NBD12] R. Ngayam-Happy, C. S. Becquart, C. Domain, and L. Malerba. "Formation and evolution of MnNi clusters in neutron irradiated dilute Fe alloys modelled by a first principle-based AKMC method." *Journal of Nuclear Materials*, **426**(1-3):198–207, 2012.

[NS12] M. Nastar and F. Soisson. "Atomistic modeling of phase transformations: Point-defect concentrations and the time-scale problem." *Physical Review B*, **86**:220102, 2012.

[OIT14] Y. Oda, A. M. Ito, A. Takayama, and H. Nakamura. "First-Principles Study on Migration of Vacancy in Tungsten." *Plasma and Fusion Research*, **9**:3401117, Mar 2014.

[OR79] P. R. Okamoto and L. E. Rehn. "Radiation-induced segregation in binary and ternary alloys." *Journal of Nuclear Materials*, **83**(1):2–23, 1979.

[PBE96] John P. Perdew, Kieron Burke, and Matthias Ernzerhof. "Generalized Gradient Approximation Made Simple." *Phys. Rev. Lett.*, **77**(18):3865–3868, 1996. erratum, *ibid.* **78**, 1396(E) (1997).

[PSM99] C. Pareige, F. Soisson, G. Martin, and D. Blavette. "Ordering and phase separation in Ni–Cr–Al: Monte Carlo simulations vs three-dimensional atom probe." *Acta Materialia*, **47**(6):1889 – 1899, 1999.

[RDV13] M. Rieth, S. L. Dudarev, S. M. Gonzalez de Vicente, J. Aktaa, T. Ahlgren, S. Antusch, D. E. J. Armstrong, M. Balden, N. Baluc, M. F. Barthe, W. W. Basuki, M. Battabyal, C. S. Becquart, D. Blagoeva, H. Boldyryeva, J. Brinkmann, M. Celino, L. Ciupinski, J. B. Correia, A. De Backer, C. Domain, E. Gaganidze, C. García-Rosales, J. Gibson, M. R. Gilbert, S. Giusepponi, B. Gludovatz, H. Greuner, K. Heinola, T. Höschen, A. Hoffmann, N. Holstein, F. Koch, W. Krauss, H. Li, S. Lindig, J. Linke, Ch. Linsmeier, P. López-Ruiz, H. Maier, J. Matejicek, T. P. Mishra, M. Muhammed, A. Muñoz, M. Muzyk, K. Nordlund, D. Nguyen-Manh, J. Opschoor, N. Ordás, T. Palacios, G. Pintsuk, R. Pippan, J. Reiser, J. Riesch, S. G. Roberts, L. Romaner, M. Rosiñski, M. Sanchez, W. Schulmeyer, H. Traxler, A. Ureña, J. G. van der Laan, L. Veleva, S. Wahlberg, M. Walter, T. Weber, T. Weitkamp, S. Wurster, M. A. Yar, J. H. You, and A. Zivelonghi. "Recent progress in research on tungsten materials for nuclear fusion applications in Europe." *J. Nucl. Mater.*, **432**(1-3):482–500, January 2013.

[RMO11] C. Reina, J. Marian, and M. Ortiz. "Nanovoid nucleation by vacancy aggregation and vacancy-cluster coarsening in high-purity metallic single crystals." *Physical Review B*, **84**(10), 2011.

[San93] J. M. Sanchez. "Cluster expansions and the configurational energy of alloys." *Physical Review B*, **48**:14013–14015, Nov 1993.

[SB02] S. Schmauder and P. Binkele. "Atomistic computer simulation of the formation of Cu-precipitates in steels." *Computational Materials Science*, **24**(1-2):42–53, 2002.

[SBA13] S. Shu, P. Bellon, and R. S. Averback. "Complex nanoprecipitate structures induced by irradiation in immiscible alloy systems." *Physical Review B*, **87**(14), 2013.

[SBC10] F. Soisson, C. S. Becquart, N. Castin, C. Domain, L. Malerba, and E. Vincent. "Atomistic Kinetic Monte Carlo studies of microchemical evolutions driven by diffusion processes under irradiation." *Journal of Nuclear Materials*, **406**(1):55–67, 2010.

[SBM96] F. Soisson, A. Barbu, and G. Martin. "Monte Carlo simulations of copper precipitation in dilute iron-copper alloys during thermal ageing and under electron irradiation." *Acta Materialia*, **44**(9):3789–3800, 1996.

[SDN13] A. E. Sand, S. L. Dudarev, and K. Nordlund. "High-energy collision cascades in tungsten: Dislocation loops structure and clustering scaling laws." *EPL (Europhysics Letters)*, **103**(4):46003, 2013.

[SF07] F. Soisson and C. Fu. "Cu-precipitation kinetics in α-Fe from atomistic simulations: Vacancy-trapping effects and Cu-cluster mobility." *Physical Review B*, **76**:214102, 2007.

[SG64] A. Savitzky and M. J. E. Golay. "Smoothing and Differentiation of Data by Simplified Least Squares Procedures." *Analytical Chemistry*, **36**(8):1627–1639, 1964.

[sgm] The semi-grand canonical (SG) ensemble employed in the present work is characterized for a two-component system by the following parameters: (i) the *total* number of sites (or particles N, (ii) the chemical potential difference between the components μ, (iii) the temperature T, and (iv) the volume V. By contrast, the equivalent grand canonical (GC) ensemble depends on the number of sites (particles) of type A, N_{A}, and B, N_{B}, as well as T and V. Accordingly, in the GC ensemble the total number of sites (particles) is *not* constant. While Monte Carlo (MC) simulations of the present kind based on lattice Hamiltonians are occasionally described as GCMC simulations, the fact that the total number of atoms is fixed implies that they should be instead referred to as SGMC simulations.

[SM74] VK Sikka and J Moteff. "Identification of α-Mn crystal structure in neutron irradiated W-Re alloy." *Metallurgical and Materials Transactions B*, **5**(6):1514–1517, 1974.

[SNK16] W. Setyawan, G. Nandipati, and R. J. Kurtz. "Interaction of interstitial clusters with rhenium, osmium, and tantalum in tungsten." Technical Report DOE/ER-0313/60, June 2016.

[SNR15a] W. Setyawan, G. Nandipati, K. J. Roche, R. J. Kurtz, and B. D. Wirth. "Quantum Calculations of Energetics of Rhenium Clusters in Tungsten." *Semiannual Progress Report*, **58**(8.4):266–271, 2015.

[SNR15b] Wahyu Setyawan, Giridhar Nandipati, Kenneth J. Roche, Howard L. Heinisch, Brian D. Wirth, and Richard J. Kurtz. "Displacement cascades and defects annealing in tungsten, Part I: Defect database from molecular dynamics simulations." *Journal of Nuclear Materials*, **462**:329 – 337, 2015.

[Soi05] F. Soisson. "Monte Carlo simulations of segregation and precipitation in alloys under irradiation." *Philosophical Magazine*, **85**(4-7):489–495, 2005.

[Soi06] F. Soisson. "Kinetic Monte Carlo simulations of radiation induced segregation and precipitation." *Journal of Nuclear Materials*, **349**(3):235–250, 2006.

[SSM16] O. Senninger, F. Soisson, E. Martínez, M. Nastar, C. Fu, and Y. Brechet. "Modeling radiation induced segregation in iron-chromium alloys." *Acta Materialia*, **103**:1 – 11, 2016.

[SYH14] T Suzudo, M Yamaguchi, and A Hasegawa. "Stability and mobility of rhenium and osmium in tungsten: first principles study." *Modelling and Simulation in Materials Science and Engineering*, **22**(7):075006, 2014.

[SYH15] T. Suzudo, M. Yamaguchi, and A. Hasegawa. "Migration of rhenium and osmium interstitials in tungsten." *Journal of Nuclear Materials*, **467, Part 1**:418–423, 2015.

[THF08] Takashi Tanno, Akira Hasegawa, Mitsuhiro Fujiwara, Jian-Chao He, Shuhei Nogami, Manabu Satou, Toetsu Shishido, and Katsunori Abe. “Precipitation of Solid Transmutation Elements in Irradiated Tungsten Alloys.” *Mater. Trans.*, **49**(10):2259–2264, 2008.

[THH07] Takashi Tanno, Akira Hasegawa, Jian-Chao He, Mitsuhiro Fujiwara, Shuhei Nogami, Manabu Satou, Toetsu Shishido, and Katsunori Abe. “Effects of Transmutation Elements on Neutron Irradiation Hardening of Tungsten.” *Mater. Trans.*, **48**(9):2399–2402, 2007.

[THH09] T. Tanno, A. Hasegawa, J. C. He, M. Fujiwara, M. Satou, S. Nogami, K. Abe, and T. Shishido. “Effects of transmutation elements on the microstructural evolution and electrical resistivity of neutron-irradiated tungsten.” *J. Nucl. Mater.*, **386–388**:218–221, April 2009.

[TLA04] F. Tavazza, D. P. Landau, and J. Adler. “Phase diagram and structural properties for a compressible Ising ferromagnet at constant volume.” *Physical Review B*, **70**:184103, 2004.

[TMB05] Dmitry Terentyev, Lorenzo Malerba, and AV Barashev. “On the correlation between self-interstitial cluster diffusivity and irradiation-induced swelling in Fe–Cr alloys.” *Philosophical magazine letters*, **85**(11):587–594, 2005.

[TPK15] Anastasios Tsourtis, Yannis Pantazis, Markos A Katsoulakis, and Vagelis Harmandaris. “Parametric sensitivity analysis for stochastic molecular systems using information theoretic metrics.” *The Journal of chemical physics*, **143**(1):014116, 2015.

[VBD08] E. Vincent, C. S. Becquart, and C. Domain. “Microstructural evolution under high flux irradiation of dilute Fe-CuNiMnSi alloys studied by an atomic kinetic Monte Carlo model accounting for both vacancies and self interstitials.” *Journal of Nuclear Materials*, **382**(2-3):154–159, 2008.

[VBP08] E. Vincent, C. S. Becquart, C. Pareige, P. Pareige, and C. Domain. “Precipitation of the FeCu system: A critical review of atomic kinetic Monte Carlo simulations.” *Journal of Nuclear Materials*, **373**(1-3):387–401, 2008.

[VWF12] Lisa Ventelon, F Willaime, Chu-Chun Fu, M Heran, and I Ginoux. “Ab initio investigation of radiation defects in tungsten: Structure of self-interstitials and specificity of di-vacancies compared to other bcc transition metals.” *Journal of Nuclear Materials*, **425**(1):16–21, 2012.

[Was07] Gary S Was. *Fundamentals of radiation materials science: metals and alloys.* Springer Science & Business Media, 2007.

[WF03] R. Weinkamer and P. Fratzl. “By which mechanism does coarsening in phase-separating alloys proceed?” *EPL (Europhysics Letters)*, **61**(2):261, 2003.

[WFG04] R. Weinkamer, P. Fratzl, H. S. Gupta, O. Penrose, and J. L. Lebowitz. “Using Kinetic Monte Carlo simulations to study phase separation in Alloys.” *Phase Transitions*, **77**(5-7):433–456, 2004.

[WFM05] F. Willaime, C. C. Fu, M. C. Marinica, and J. D. Torre. “Stability and mobility of self-interstitials and small interstitial clusters in -iron: ab initio and empirical potential calculations.” *Nuclear Instruments and Methods in Physics Research Section B: Beam Interactions with Materials and Atoms*, **228**(1-4):92–99, 2005. Proceedings of the Seventh International Conference on Computer Simulation of Radiation Effects in Solids.

[Wil35] E. J. Williams. “The Effect of Thermal Agitation on Atomic Arrangement in Alloys. III.” *Proceedings of the Royal Society of London. Series A, Mathematical and Physical Sciences*, **152**(875):231–252, 1935.

[WNK16] J. S. Wrobel, D. Nguyen-Manh, K. J. Kurzydlowski, and S. L. Dudarev. “Radiation-induced segregation in dilute Re-W solid solutions.” *ArXiv e-prints*, April 2016.

[WNK17] J S Wróbel, D Nguyen-Manh, K J Kurzydłowski, and S L Dudarev. “A first-principles model for anomalous segregation in dilute ternary tungsten-rhenium-vacancy alloys.” *Journal of Physics: Condensed Matter*, **29**(14):145403, 2017.

[Wol12] W. G. Wolfer. “Fundamental Properties of Defects in Metals.” In Rudy J.M. Konings, editor, *Comprehensive Nuclear Materials*, volume 1, pp. 1–45. Elsevier, Oxford, 2012.

[WWB83] R. K. Williams, F. W. Wiffen, J. Bentley, and J. O. Stiegler. “Irradiation induced precipitation in tungsten based, W-Re alloys.” *Metall. Trans. A*, **14**(3):655–666, March 1983.

[WZK12] P. Warczok, J. Ženíšek, and E. Kozeschnik. “Atomistic and continuums modeling of cluster migration and coagulation in precipitation reactions.” *Computational Materials Science*, **60**:59–65, 2012.

[XAB17] Alan Xu, David E.J. Armstrong, Christian Beck, Michael P. Moody, George D.W. Smith, Paul A.J. Bagot, and Steve G. Roberts. “Ion-irradiation induced clustering in W-Re-Ta, W-Re and W-Ta alloys: An atom probe tomography and nanoindentation study.” *Acta Materialia*, **124**:71 – 78, 2017.

[XBA15] Alan Xu, Christian Beck, David E.J. Armstrong, Krishna Rajan, George D.W. Smith, Paul A.J. Bagot, and Steve G. Roberts. “Ion-irradiation-induced clustering in W-Re and W-Re-Os alloys: A comparative study using atom probe tomography and nanoindentation measurements.” *Acta Materialia*, **87**:121 – 127, 2015.

[YE66] W. M. Young and E. W. Elcock. “Monte Carlo studies of vacancy migration in binary ordered alloys: I.” *Proceedings of the Physical Society*, **89**(3):735, 1966.

[YSM15] X. Yi, A. E. Sand, D. R. Mason, M. A. Kirk, S. G. Roberts, K. Nordlund, and S. L. Dudarev. "Direct observation of size scaling and elastic interaction between nano-scale defects in collision cascades." *EPL (Europhysics Letters)*, **110**(3):36001, 2015.

[ZG00] S. J. Zinkle and N. M. Ghoniem. "Operating temperature windows for fusion reactor structural materials." *Fusion Engineering and Design*, **51–52**:55–71, November 2000.

[ZLH13] W.H. Zhou, Y.G. Li, L.F. Huang, Z. Zeng, and X. Ju. "Dynamical behaviors of self-interstitial atoms in tungsten." *Journal of Nuclear Materials*, **437**(1-3):438 – 444, 2013.

[ZM04] S.J Zinkle and Y Matsukawa. "Observation and analysis of defect cluster production and interactions with dislocations." *Journal of Nuclear Materials*, **329–333, Part A**:88 – 96, 2004. Proceedings of the 11th International Conference on Fusion Reactor Materials (ICFRM-11).